Experimental and Numerical Evaluations of Viscoplastic Material Behaviour and Multiaxial Ratchetting for Austenitic and Ferritic Materials

Von der Fakultät Energie-, Verfahrens- und Biotechnik der Universität Stuttgart zur Erlangung

der Würde eines Doktor-Ingenieurs (Dr.-Ing.) genehmigte Abhandlung

Vorgelegt von

MSc. Yu Wang

Geboren in Henan, VR. China

Hauptberichter: Prof. Dr.-Ing. habil. Eberhard Roos

Mitberichter: Prof. Dr.-Ing. habil. Karl Maile

Tag der mündlichen Prüfung: 06.05.2014

Institut für Materialprüfung, Werkstoffkunde und Festigkeitslehre

(IMWF) Universität Stuttgart und

Materialprüfungsanstalt (MPA) Universität Stuttgart

2014

Vorwort

Die vorliegende Arbeit entstand während meiner Tätigkeit als wissenschaftlicher Mitarbeiter an der Materialprüfungsanstalt (MPA) Universität Stuttgart sowie am Institut für Materialprüfung, Werkstoffkunde und Festigkeitslehre (IMWF) Universität Stuttgart.

Mein besonderer Dank gilt Herrn Prof. Dr.-Ing. habil. E. Roos für die Möglichkeit der Anfertigung dieser Arbeit, die Betreuung und das stete Interesse am Fortgang dieser Arbeit, die wertvollen Diskussionen und zahlreichen Anregungen.

Herrn Prof. Dr.-Ing. habil. K. Maile danke ich sehr herzlich für sein Interesse an dieser Arbeit und die Übernahme der zweiten Berichterstattung.

Des weiteren bedanke ich mich bei allen Mitarbeiterinnen und Mitarbeitern des Instituts für Materialprüfung, Werkstoffkunde und Festigkeitslehre und der Material-prüfungsanstalt für die gute Zusammenarbeit und Unterstützung.

Ganz besonders aber möchte ich meinen Kollegen Herrn Dr. Ludwig Stumpfrock und Herrn Dr. Siegfried Krolop danken, deren ständige Bereitschaft zur fachlichen Diskussion eine wertvolle Hilfe war. Weiterhin gilt mein Dank allen Kolleginnen und Kollegen der Abteilung Berechnung, für das mir entgegengebrachte Vertrauen und die angenehme Arbeitsatmosphäre.

Meiner Frau Dr. Yawei Zhang und meinen Eltern gilt mein besonderer Dank für ihr Verständnis und ihre Unterstützung während des Entstehens dieser Arbeit.

Table of contents

Deutsche Zusammenfassung

Bauteile in Kraftwerken sind im Betrieb zyklischen Beanspruchungen, die zur in-elastischen Verformung im Werkstoff führen können, ausgesetzt. Wenn die Werkstoffe, insbesondere unter einachsiger zyklischer Beanspruchung mit Mittelspannung oder unter mehrachsiger kombinierter konstanter (primärer) und zyklischer Beanspruchung belastet sind, kann sich eine fortschreitende plastische Deformation akkumulieren. Diese fortschreitende plastische Deformation, genannt Ratchetting, ist im Bereich der niederzyklischen Ermüdung (Low-Cycle-Fatigue), in dem hohe Beanspruchungsamplituden vorliegen, relevant und spielt daher für die Sicherheit im Betrieb einer Anlage eine wichtige Rolle.

Zur genaueren Ermittlung der Lebensdauer von hochbeanspruchten Komponenten im Rahmen der Festigkeits- und Ermüdungsfestigkeitsanalysen, werden Werkstoff-modelle, die die komplexen inelastischen Verformungsvorgänge unter zyklischer Beanspruchung beschreiben können, angewandt. Ein Werkstoffmodell, auch Konstitutivmodell genannt, stellt den mathematischen Zusammenhang zwischen Spannungstensor und Dehnungstensor dar, und beschreibt damit das nichtlineare, zeitabhängige zyklische Materialverhalten im allgemeinen dreiachsigen Spannungs-zustand. Das Ziel dieser Arbeit ist es, ein Werkstoffmodell zu entwickeln und zu verifizieren, um das zyklische inelastische Materialverhalten des austenitischen Stahls X6CrNiNb18-10 und des ferritischen Stahls 20MnMoNi5-5 numerisch zu simulieren und insbesondere den Ratchetting Effekt zu quantifizieren.

Um das dehnratenabhängige, viskoplastische Materialverhalten unter zyklischer Beanspruchung zu beschreiben, wird, aufbauend auf einem zeitunabhängigen Chaboche-Modell, ein viskoplastisches Chaboche-Modell verwendet. Die Effekte der Dehnraten- bzw. Zeitabhängigkeit wurde durch eine Viskospannung im Modell implementiert. Die Beschreibung des zyklischen Materialverhaltens wird durch die Einführung von weiteren inneren Variablen realisiert.

Die tensorielle kinematische Verfestigungsvariable, in der Literatur häufig Backstress oder Rückspannung genannt, wird verwendet, um die richtungsabhängige Ver-festigung (Dehnungsverfestigung) zu beschreiben. In der vorliegenden Arbeit werden

unterschiedliche nicht-lineare kinematische Verfestigungsmodelle untersucht, darunter das Armstrong-Frederick-Modell als grundlegendes nichtlineares kinematisches Verfestigungsmodell, das Ohno-Wang-Modell, das besonders zur Simulation der Ratchettingverformung geeignet ist, und das Krämer-Krolop-Modell zur Beschreibung der nichtproportionalen Effekte bei einer mehrachsigen nichtproportionalen zyklischen Beanspruchung. Durch Verwendung von vier Rückspannungsvariablen im Werkstoffmodell kann die zyklische Dehnungsverfestigung in einem größeren Schwingbreitenbereich präziser beschrieben werden.

Die richtungsunabhängige Verfestigung und Entfestigung - zyklische Verfestigung und Entfestigung genannt - wird durch skalare isotrope Verfestigungsvariable im Werkstoffmodell berücksichtigt. Im Rahmen dieser Arbeit werden verschiedene Verfestigungsmodelle mit isotropem Charakter entwickelt und untersucht. Mit diesen Modellen können unterschiedliche Mechanismen wie zyklische Verfestigung mit und ohne Sättigung, zyklische Entfestigung oder kombinierte zyklische Verfestigung und Entfestigung abgebildet werden.

Weiter wird die Entwicklungsgleichung für den Dehnungs-Gedächtnis-Effekt in das viskoplastische Chaboche-Modell implementiert, um im Experiment beobachtete Gedächtniseffekte zu berücksichtigen.

Das so erweiterte viskoplastische Chaboche-Modell wird in verschiedenen Fassungen als Unterprogramm UMAT des kommerziellen Finite Elemente Programmes ABAQUS implementiert und kann zur numerischen Simulation von Bauteilen angewendet werden. Die unterschiedlichen Fassungen werden im weiteren als Armstrong-Frederick-Modell, Ohno-Wang-Modell und Krämer-Krolop-Modell bezeichnet.

Zur Bestimmung der Materialparameter des Werkstoffmodells mit dem numerischen Optimierungsprogramm MINUIT werden zunächst einachsige Versuche im üblichen Labormaßstab durchgeführt. Parallel wird das Werkstoffmodell in einachsiger Formulierung in das Optimierungsprogramm integriert. Durch Vergleich von gemessenen und berechneten Ergebnissen an den ausgewählten Werkstoffen werden die Parameter so optimiert, bis minimale Abweichungen zwischen Messung und Rechnung erreicht sind.

Zur Verifikation des Werkstoffmodells an unterschiedlichen wechselnden Beanspruch-ungen wird ein umfangreiches Versuchsprogramm mit den ausgewählten Werkstoffen realisiert. Dies umfasst axiale Zugversuche, axiale dehnungsgesteuerte zyklische Zugdruckversuche und spannungsgesteuerte Treppenstufenzugdruckversuche mit Mittelspannung bei unterschiedlicher Prüftemperatur. Mit den zuvor ermittelten Parametern werden sehr gute, teilweise sogar vollständige Übereinstimmungen zwischen den durchgeführten einachsigen zyklischen Versuchen und den numerischen Berechnungen erzielt.

Zur weiteren Verifikation der Werkstoffmodelle werden experimentelle Unter-suchungen an Geradrohrabschnitten, also realen Bauteilen, bei Raumtemperatur und T = 300 °C durchgeführt. Das Versuchsprogramm umfasst mehrachsige zyklische Torsionsversuche ohne und mit axialer Ratchettingverformung sowie Versuche bei denen sich die Torsionsbelastungen und somit die axialen Zugdruckbelastungen in Phase und gegen Phase zyklisch verändern.

Die folgenden Erkenntnisse können aus den Bauteilversuchen und den zugehörigen numerischen Simulationen mit den Erweiterungen des Chaboche-Modells abgeleitet werden:

Sowohl das Armstrong-Frederick-Modell als auch das Ohno-Wang-Modell zur Simulation kinematischen Verfestigungsverhaltens zeigen gute Übereinstimmungen zwischen Berechnung und Messung hinsichtlich Dehnungsverfestigung. Durch Kombination mit isotropen Verfestigungsmodellen können die Werkstoffmodelle die von der Dehnungsschwingbreite abhängigen zyklischen Verfestigungen und Entfestigungen sehr gut nachbilden.

Bei Vorliegen von mehrachsigem Ratchetting überschätzt das Armstrong-Frederick-Modell die Ratchettingdehnung für alle untersuchten Fälle hinsichtlich Temperatur und Schwingbreite, während das Ohno-Wang-Modell akzeptable Ergebnisse liefert: Das mehrachsige Ratchetting mit einer hohen primären Spannung wird durch das Ohno-Wang-Modell gut nachgebildet. Bei niedriger oder stark wechselnder primärer Spannung wird die Ratchettingdehnung in der Anfangsphase, also in den ersten

Zyklen, jedoch überschätzt. Diese Abweichung zwischen Berechnung und experimenteller Beobachtung ist auf den Unterschied zwischen einachsigem und mehrachsigem Ratchetting zurückzuführen. Die mittels einachsigen Ratchettingversuchen bestimmten Werkstoffparameter können das mehrachsige Ratchetting nicht unbedingt beschreiben.

Effekte aus nichtproportionaler Belastung mit zusätzlicher Verfestigung bei zyklischer nichtproportionaler mehrachsiger Beanspruchung können grundsätzlich durch das Krämer-Krolop-Modell simuliert werden. Die Größe der zusätzlichen Verfestigung hängt auch von der Nichtproportionalität der zyklischen Beanspruchung ab, also von der Form des Lastpfads.

Aus den bisherigen Ergebnissen lassen sich folgende weiter führende Arbeiten ableiten: Die Simulation der Ratchettingdehnung bei niedriger oder stark wechselnder primärer Spannung mit dem Ohno-Wang-Modell bedarf noch weiterer Verbesserung, um die bis dato berechneten Abweichungen zu verringern. Die Abweichungen liegen zwar auf der sicheren Seite, hinsichtlich eines optimalen Betriebs ist es jedoch wünschenswert diese Abweichung zu reduzieren.

Die Abhängigkeit der zusätzlichen Verfestigungseffekte bei nichtproportionaler Belastung könnte durch Ermittlung der Parameter quantitativ bestimmt werden und somit eine weitere Verbesserung der Übereinstimmung zwischen Experiment und numerischer Simulation bringen.

Abstract

Components in power plants are subjected under cyclic loading, which can yield inelastic deformation. When the materials are loaded under uniaxial cyclic loading with mean-stress or under multiaxial combined constant (primary) and cyclic loading (secondary), a progressive plastic deformation can gradually accumulate. This progressive plastic deformation, so-called ratchetting, is related to low cycle fatigue, in which high loading amplitudes are existent, therefore plays an important role in service safety of power plant facilities.

For the accurate determination on life-time of highly loaded components in the frame of strength and fatigue analyses, material models, which are able to describe complex inelastic deformation processes under cyclic loading, should be applied. A material model, also called constitutive model, represents the mathematical relationship between stress and strain tensors, and thereby describes the nonlinear time dependent cyclic material behaviour in multiaxial stress-state. The objective of this work is to develop and verify a material model, in order to numerically simulate the cyclic inelastic material behaviour of the austenitic steel X6CrNiNb18-10 and the ferritic steel 20MnMoNi5-5, especially the ratchetting effect.

The tensorial kinematic hardening variable, so-called back-stress, is used to describe the direction dependent hardening (strain-hardening). In this work, different nonlinear kinematic hardening models are investigated, that include the Armstrong-Frederick-model as fundamental nonlinear kinematic hardening model, the Ohno-Wang-model, which is particular suitable to simulate the ratchetting deformation, and the Krämer-Krolop-model for taking into account the nonproportional effect under multiaxial nonproportional cyclic loading. By applying four back-stress variables in the material model, the cyclic strain hardening in a large strain-range can be accurately described.

The direction independent hardening and softening, so-called cyclic hardening and softening, is included in the material model by means of scalar isotropic hardening variable. In the frame of this work, different isotropic hardening models are developed and investigated. By using these models, various mechanisms, such as cyclic hardening

with and without saturation, cyclic softening, or combined cyclic hardening and soften-ing, can be represented.

In addition, the evolution equation for so-called strain-memory-effect is implemented in the viscoplastic Chaboche model, in order to take into account the memory-effect ob-served in experiment.

The extended viscoplastic Chaboche model is implemented in different versions as subroutine UMAT of commercial finite element program ABAQUS and can be used for the simulation of real components. Regarding formulation of the kinematic hardening variable, the different versions are denoted as Armstrong-Frederick-model, Ohno-Wang-model and Krämer-Krolop-model subsequently.

To determine the parameters of the material models with the numerical optimization program MINUIT, uniaxial tests in conventional bench-scale are performed at first. In parallel, the material model in uniaxial formulation is integrated in the optimization pro-gram. By comparing measured and calculated results of the selected materials, the parameters are optimized, until the minimal deviations between measurement and cal-culation are reached.

For the verification of the material model under different alternating loading conditions, a comprehensive test program with the selected materials is implemented. This in-cludes axial tensile tests, axial strain-controlled cyclic tension-compression tests and axial stress-controlled stepwise tension-compression tests with mean-stress at differ-ent test temperatures. With the determined parameters, very good and partially even complete agreements between the performed uniaxial cyclic tests and numerical simu-lations are achieved.

For the further verification of the material models, component tests with straight pipe section are performed at room temperature and 300 °C. The test program incorporates multiaxial cyclic torsion tests with and without axial ratchetting deformation as well as tests, in which the torsional loading and the axial tension-compression loading are re-spectively in-phase and out-of-phase cyclic applied.

The following conclusions can be drawn based on the component tests and corresponding numerical simulations with the extended Chaboche models:

For the simulation of strain hardening, both the Armstrong-Frederick-model and the Ohno-Wang-model show good agreements between calculation and measurement. Via the combination with isotropic hardening models, the material models can very well simulate the strain-range dependent cyclic hardening and softening.

With the existence of multiaxial ratchetting, the Armstrong-Frederick-model overestimates the ratchetting strain in all researched cases with respect to temperature and loading range, while the Ohno-Wang-model provides acceptable results: The multiaxial ratchetting with a high primary stress is accurately simulated by using the Ohno-Wang-model. However, under low or pronounced alternating primary stress, the ratchetting strain is overestimated in the beginning phase, the first several cycles. This deviation between simulation and experimental observation results from the difference between uniaxial and multiaxial ratchetting behaviour. The material parameters identified by using uniaxial ratchetting tests cannot absolutely describe the multiaxial ratchetting behaviour.

Effects of nonproportional loading with additional hardening under cyclic nonproportional multiaxial loading can be in principle simulated by using the Krämer-Krolop-model. The magnitude of the additional hardening is dependent upon the nonproportionality of the cyclic loading, for instance the form of load path.

Based on current results, following further works are anticipated: The simulation of ratchetting strain under low or pronounced alternating primary stress with the Ohno-Wang-model can be further improved, in order to reduce the current deviation. Although the deviations are on the safe side, concerning an optimal operation, it is preferable to reduce this deviation.

The dependence of the additional hardening under nonproportional loading can be quantitatively determined by means of parameter identification, and thus provide a further improvement on the agreement between experiment and numerical simulation.

Abbreviation and notations:

Abbreviation:

AFC	Armstrong-Frederick-Chaboche
FEA	Finite element analysis
FEM	Finite element method
KTA	Kerntechnischer Ausschuss (nuclear technologie committee)
LCF	Low cycle fatigue
LK	Linear kinematic hardening approach
NLK	Nonlinear kinematic hardening approach
RT	Room temperature

General notations:

A	Scale value
$\underline{A}$	Vector
$\underline{\underline{A}}$	Tensor
$\dot{A}$	Time derivative

Notations:

e	-	Mathematical constant
$\underline{\underline{\varepsilon}}$	-	Total strain tensor
$\underline{\underline{\varepsilon}}_e$	-	Elastic strain tensor
$\varepsilon_{eng.}$	-	Engineering strain
$\Delta \varepsilon_{eq}$	-	Equivalent strain range
$\dot{\varepsilon}_{eq}$	1/s	Equivalent strain rate
$\underline{\underline{\varepsilon}}_{in}$,	-	Inelastic strain tensor
ε_{true}	-	True strain
$\underline{\underline{\varepsilon}}_p$	-	Viscoplastic strain tensor

$\underline{\dot{\underline{\varepsilon}}}_p$	1/s	Tensor of viscoplastic strain-rate
$\underline{\underline{E}}$	MPa	Elasticity tensor
f	-	Viscoplastic flow rule
Φ_1	J/m³/s	Intrinsic dissipation
Φ_2	J/m²/s	Thermal dissipation
$J_2(\underline{\underline{\sigma}})$	MPa	Second invariant of stress tensor
$J_3(\underline{\underline{\sigma}})$	MPa	Third invariant of stress tensor
$H(F)$	-	Heaviside step function
$\underline{\underline{I}}$	-	Unit tensor
k	MPa	Initial size of elastic domain
p	-	Accumulated viscoplastic plastic strain
$\dot{p}$	1/s	Accumulated viscoplastic plastic strain-rate
$\underline{q}$	J/m²/s	Heat flux
r	MPa	Isotropic hardening variable (microscopic)
R	MPa	Isotropic hardening variable (macroscopic)
s	J/K	Entropy
$\underline{\underline{\sigma}}$	MPa	Stress tensor
$\underline{\underline{\sigma}}'$	MPa	Deviatoric stress
$\sigma_{eng.}$	MPa	Engineering stress
$\sigma_{m.}$	MPa	Mean stress
$\sigma_{true.}$	MPa	True stress
σ_{vis}	MPa	Viscous stress or over stress
T	°C	Temperature
ρ	t/mm³	Mass density
$\underline{\underline{X}}$	MPa	Kinematic hardening variable (macroscopic) or back-stress
$\underline{\underline{X}}'$	MPa	Deviatoric back-stress
Ω_p	J	Dissipation potential
Ω_r	J	Recovery potential
Ψ	J	Free energy potential

Z	-	Material parameter in dissipation potential and viscous stress
n	-	Material parameter in dissipation potential and viscous stress
c , c_i	-	Material parameter in kinematic hardening approach
γ_i γ_{31} γ_{32}	-	Material parameters in kinematic hardening approach
β_3	-	Material parameter in kinematic hardening approach
X_L	MPa	Material parameter in kinematic hardening approach
h_i	-	Material parameter in Ohno-Wang approach
m_i	-	Material parameter in Ohno-Wang approach
M	-	Number of back-stress used in kinematic hardening approach
$\underline{\underline{k}}_i$	MPa	Unified kinematic hardening variable $\underline{\underline{X}}_i$
p^*	-	Function used in Krämer-Krolop approach
c'' c'''	-	Material parameters in Krämer-Krolop approach
φ	-	Function in Krämer-Krolop approach
κ	-	Function in Krämer-Krolop approach
$\underline{\underline{n}}$	-	Normal of equipotential surface
a , b , c	-	Material parameter in isotropic hardening approach
Q	MPa	Material parameter in isotropic hardening approach
q_s	-	Internal variable for strain-memory-effect
q_1 , q_2	-	Material parameters in isotropic hardening approach
$\underline{\underline{\xi}}$	-	Internal variable for strain memory effect
η	-	Material parameter for strain memory effect
$\underline{\underline{n}}^*$	-	Normal of strain memory surface
μ	-	Material parameter for strain memory effect
Q_0 , Q_{max}	MPa	Material parameter for strain memory effect

1 Introduction and objectives

1.1 General introduction

Many equipments and components in power plants are exposed to coupled mechanical and thermal loading in service, which lead to inelastic deformations in material at highly stressed regions. Besides the change of plastification under single load, the superposition of cyclic load components can also lead to a progressive deformation. This progress of deformation due to the change of plastification under cyclic loading, which is so-called ratchetting, cannot be excluded in service. Such kind of stressing and associated material damage can influence the low-cycle-fatigue (LCF) behaviour of corresponding components. The interest of this work especially focuses on the material behaviour of pipe components, which is mainly subjected to torsion and axial load.

For the service safety design of the components in nuclear engineering equipments, the safety standards from the nuclear technology committee (KTA) [1] are applied in Germany. Besides the service safety, additional concept of basic safety was developed [2][3], so that catastrophic failure of nuclear equipments can be excluded. The cyclic loading is limited based on the $3S_m$- criterion in KTA 3201.2 for steels, in which a different way of calculation is specified depending on the type and magnitude of loading. If the amplitude of equivalent stress exceeds the material dependent value $3S_m$, the inelastic fatigue analysis with the actual material behaviour should be implemented. Nevertheless the progressive deformation (ratchetting) cannot be described by this criterion.

To predict the service life of high-stressed components more precisely, such kind of material model, which can describe the complex inelastic deformation process under cyclic loading, must be applied in the frame of structural and fatigue analyses. Such model builds up a mathematical interrelation between stress and strain (constitutive equations) and describes the nonlinear, rate-dependent and temperature-dependent material behaviour in multiaxial stress-state.

To describe inelastic material behaviour, many material laws have been developed, which are available in literatures [4]-[8]. The material laws are called phenomenological material models, if the state of material can be determined by observable values

such as stress, strain, temperature and a set of internal variables. In classic plasticity theory the scalar and tensorial internal variables are introduced to describe the isotropic and kinematic hardening, which allow the modelling of inelastic material behaviour under cyclic loading. Based on the flow surfaces, the material models can be distinguished into one-surface-model, two-surface-model and multi-surface-model.

The approach of a phenomenological material model is especially efficient with the cooperation of the finite-element-method (FEM). With the help of FEM, the stress-state of a component with a complex geometry can be computed. Nevertheless the advanced inelastic material models are not sophisticated in present commercial FEM programs. Therefore the demanded phenomenological material models should be programmed by user himself. With equilibrium and compatibility conditions the material laws build up a coupled initial value problem and boundary value problem, which must be related to time-integration. Based on the coupled nonlinear differential equation system, the stability problems of the numerical integration cannot be excluded, so that only the effective and robust integration algorithms are considered [9]. The material laws, which are implemented by using effective and robust integration algorithms, together with the FEM function as a software package, by which the stress-state of a component can be evaluated.

1.2 Objectives

As described above, the numerical method should be applied to study the service safety of components subjected to cyclic plastification in nuclear power plants. Therefore a material model must be employed, so that the cyclic behaviour of involved materials can be correctly described.

In the frame of this work, two metallic materials, which are widely applied in German boiling-water-reactors and pressurized-water-reactors, were studied. A material model was selected and improved for performing FE analysis. Since this type of power plants is designed for a temperature range, which is less than $400^{o}C$, the viscous effect at high temperature must be considered. Thus a time-dependent material model was considered.

In summary, the material model should fulfil the following requirements:

- Describing time-dependent viscoplastic material behaviour.
- Describing kinematic hardening behaviour.
- Describing cyclic hardening and cyclic softening behaviour.
- Describing uniaxial and multiaxial ratchetting deformation.
- Describing effect under multiaxial nonproportional cyclic loading.

The Armstrong-Frederick-Chaboche model (AFC model) was developed by ONERA [10], which provides the possibility to fulfil above-mentioned requirements. The AFC model was derived and improved by Chaboche, Armstrong and Frederick, and served as a basic principle for material characterization. In addition, to take into account the time-dependent effects, a viscoplastic material model was developed by Chaboche [11] [12] based on the AFC model, which is so-called viscoplastic Chaboche model. In the frame of this work, the viscoplastic Chaboche model is extended by applying different evolution equations for kinematic hardening and isotropic hardening/softening, so that the cyclic inelastic behaviour of involved materials can be correctly described. Since currently this material model is not available in commercial FE program ABAQUS, an ABAQUS user subroutine UMAT should be applied, in which the material laws can be implemented.

The viscoplastic material model contains a series of material parameters. Before the application of the material model for complex multiaxial stress-state, these parameters must be determined, so that the material model can be identified. The material parameters characterize the corresponding material behaviour and can be determined by means of implementing adequate uniaxial tensile tests, cyclic uniaxial tension-compression tests and multiple-step-tests. Since most of these parameters don't relate to the classical material characteristic values, the parameter fitting process is very complicated and time-consuming. Thus a proper optimization program should be applied, so that the parameters can be reliably and efficiently determined.

After the identification of the parameters for the material model, numerical analyses can be carried out for inelastic fatigue tests of components in multiaxial stress-state. By comparing the experimental results of the component tests and calculation results

of numerical analyses, it can be verified whether the material model describes cyclic material behaviour correctly.

2   Introduction of viscoplasticity and ratchetting

The theory of viscoplasticity describes the inelastic deformation depending on time. For metals and alloys, viscoplasticity can be presented by mechanisms regarding the movement of dislocations in grain with superposed effects of intercrystalline gliding [13]. Experiments show that most metals exhibit viscoplastic behaviour at high temperatures, and some alloys show this behaviour even at room temperature.

The methods for formulating the constitutive laws of viscoplasticity can be classified into physical and phenomenological approaches [14]. The physical approach models mechanisms in microscopic point of view. It describes the plastification by means of the movement of dislocations in the crystal lattice [15]. The phenomenological approach considers the material as a continuum. Thereby the microscopic physical phenomena can be represented by means of macroscopic internal variables. In the frame of this work, the phenomenological approach was applied to set up the constitutive model.

Based on the classic theories of plasticity [16][17], the hydrostatic stress-state does not influence the inelastic deformation, and the inelastic strain only depends on the deviatoric stress. This statement should also be accepted for the modelling of viscoplasticity. Additionally, the theory of plasticity introduces yield surface, by which the elastic and plastic domains are distinguished. The size and position of yield surface can be changed with the variation of load history to describe the proper stress-state. For viscoplasticity, yield surface is replaced by using equipotential surfaces, which allow an overstress beyond yield surface.

The inelastic strain-rate is described by using viscoplastic flow rule. To study the hardening behaviour, several internal variables should be introduced. The model should comprise a tensorial internal variable to describe the kinematic hardening and a scalar internal variable, by which the isotropic hardening can be modelled. The evolution equations of these internal variables define the completely hardening behaviour of the materials.

2.1 Preconditions of the viscoplastic material models

For the mathematical description of viscoplastic material behaviour, following conventions and assumptions should be satisfied.

1. The real material is considered as a continuum despite it may contain some inclusions, dislocations, flaws and pores.

2. In initial situation, the material is isotropic and should not undertake any preload, e.g. residual stress. The originally isotropic state can only be changed by inelastic deformation.

3. Damage processes, for instance the formation of cracks, are not considered in this work.

2.2 Basic Principles

Based on the small strain hypothesis, the total strain can be divided into an elastic part and an inelastic part. That is:

$$\underline{\underline{\varepsilon}} = \underline{\underline{\varepsilon}}_e + \underline{\underline{\varepsilon}}_{in}, \tag{2.1}$$

in which $\underline{\underline{\varepsilon}}$ is total strain, $\underline{\underline{\varepsilon}}_e$ is elastic strain, and $\underline{\underline{\varepsilon}}_{in}$ is inelastic strain. In the frame of this work, only viscoplastic strain is considered as irreversible strain. Hence the hypothesis of strain partitioning can be rewritten to:

$$\underline{\underline{\varepsilon}} = \underline{\underline{\varepsilon}}_e + \underline{\underline{\varepsilon}}_p, \tag{2.2}$$

in which $\underline{\underline{\varepsilon}}_p$ is viscoplastic strain.

For a field with stress distribution $\sigma = \{\sigma_{ij}(x)\}$ and external volume forces f_i, the following equilibrium condition is hold in Cartesian coordinates:

$$\frac{\partial \sigma_{ij}}{\partial x_j} + f_i = 0, \quad i, j \in \{1,2,3\}. \tag{2.3}$$

By using the moment of momentum equation, the stress tensor can be proved to be symmetric. In case of infinitesimal deformation, the strain tensor $\underline{\underline{\varepsilon}}$ can be obtained from the components of the gradient of displacement $\underline{u}$ in Cartesian coordinate system:

$$\varepsilon_{ij} = \frac{1}{2}\left[\frac{\partial u_j}{\partial x_i} + \frac{\partial u_i}{\partial x_j}\right].$$

(2.4)

For elastic part, the relation between the stress and strain tensor can be obtained according to Hooke's law:

$$\underline{\underline{\sigma}} = \underline{\underline{E}} \cdot \underline{\underline{\varepsilon}}_e ,$$

(2.5)

where $\underline{\underline{\varepsilon}}_e$ and $\underline{\underline{\sigma}}$ are second-order tensors, and $\underline{\underline{E}}$ presents the fourth-order elasticity tensor.

2.3 Definition of thermodynamic variables

Viscoplasticity can be schematically described by using a series of equipotential surfaces, as shown in figure 2.1.
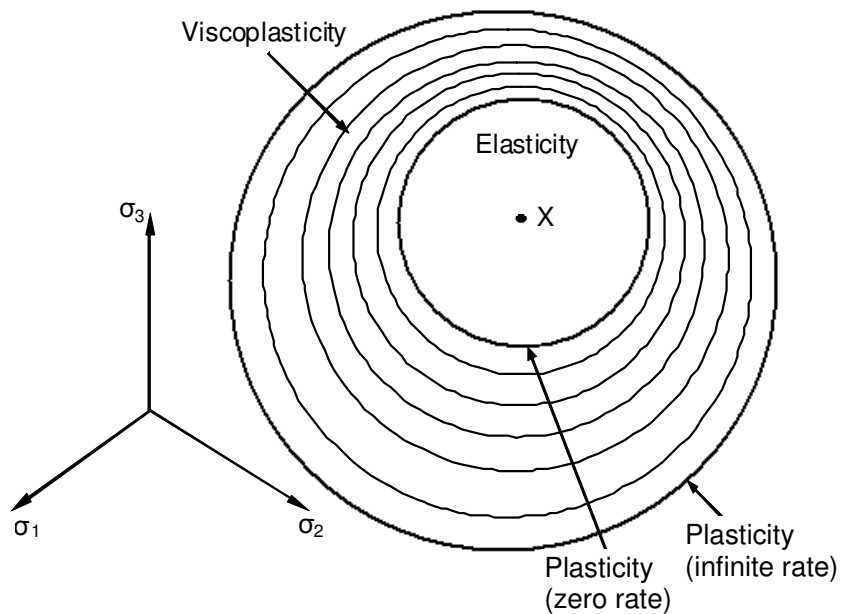

Figure 2.1: Illustration of equipotential flow surfaces.

The position of the centre and the radius of the equipotential surfaces together determine the stress-state of material. For the surface closest to the centre, $\Omega = 0$, flow rate is zero, whereas on the surface farthest from the centre, $\Omega = \infty$, flow rate is infinite. Both of these two surfaces correspond to the time-independent plasticity. The domain of viscoplasticity locates between these two surfaces. The higher is the flow rate, the larger the equipotential surface will be. For stress-state inside the inner surface, $\Omega = 0$, the material behaviour is purely elastic. The elastic domain can be expressed by $\Omega < 0$.

In thermodynamics, a free energy potential can be specified as a scalar function, which is concave with respect to temperature and convex with respect to other state variables (thermodynamic variables):

$$\Psi = \Psi(\underline{\underline{\varepsilon}}, T, \underline{\underline{\varepsilon}}_e, \underline{\underline{\varepsilon}}_p, V_k),$$ (2.6)

in which V_k denotes the internal variables, which can be scalar or tensorial variables.

In viscoplasticity, the free energy potential depends only on the elastic strain, temperature, and the internal variables V_k. Therefore it gives:

$$\Psi = \Psi(\underline{\underline{\varepsilon}}_e, T, V_k).$$ (2.7)

The thermodynamic variables, stress and entropy, are the associated variables regarding ε_e and T respectively:

$$\underline{\underline{\sigma}} = \rho \left(\frac{\partial \Psi}{\partial \underline{\underline{\varepsilon}}_e} \right),$$ (2.8)

$$s = -\frac{\partial \Psi}{\partial T},$$ (2.9)

in which s represents entropy and ρ is mass density.

The hardening in viscoplasticity can be classified into two types: kinematic hardening and isotropic hardening. Kinematic hardening describes the translation of the equipotential surface in the stress space without changes of size and shape. Isotropic hardening is based on the assumption that the centre and the shape of the equipotential

surface are fixed, while the surface can expand isotropically. Kinematic hardening can be described by using a tensorial variable $\underline{\underline{\alpha}}$, and isotropic hardening is described by a scalar variable r.

From a physical point of view, the kinematic hardening variable results from the dislocation pileups at barriers and increases as the number of dislocations in the pileup increases [18], and it gives the occurrence of Bauschinger effect. The isotropic hardening variable is associated with the number of dislocation and the stored energy. It is continuously increased or decreased unless a recovery takes place, whereas the kinematic hardening $\underline{\underline{\alpha}}$ variable does not have a continuous evolution during cyclic loading. Corresponding to the hardening variables, some thermodynamic variables can be introduced by a macroscopic way to describe the current state of microstructure.

The free energy in equation (2.7) can be decoupled to an elastic part and a viscoplastic part:

$$\Psi = \Psi_e(\underline{\underline{\varepsilon}}_e, T) + \Psi_p(\underline{\underline{\alpha}}, r, m_k, T) , \qquad (2.10)$$

and the thermodynamic forces with regard to hardening variables $\underline{\underline{\alpha}}$ and r are:

$$\underline{\underline{X}} = \rho\left(\frac{\partial \Psi}{\partial \underline{\underline{\alpha}}}\right), \text{ and } R = \rho\left(\frac{\partial \Psi}{\partial r}\right). \qquad (2.11)$$

These two thermodynamic variables, which are so-called kinematic hardening and isotropic hardening variables respectively, depict the centre of the current equipotential surface and the size of its domain, as illustrated in figure 3.1. The additional thermodynamic variables can be expressed by:

$$M_k = \rho\left(\frac{\partial \Psi}{\partial m_k}\right). \qquad (2.12)$$

By decoupling between intrinsic dissipation and thermal dissipation, the Clausius-Duhem inequality can be reduced to:

$$\Phi_1 = \underline{\underline{\sigma}} : \underline{\underline{\dot{\varepsilon}}}_p - \underline{\underline{X}} : \underline{\underline{\dot{\alpha}}} - R\dot{r} - M_k \dot{m}_k \geq 0 , \qquad (2.13)$$

$$\Phi_2 = -\left(\frac{q}{T}\right) grad T \geq 0, \tag{2.14}$$

where Φ_1 represents the intrinsic dissipation, and Φ_2 represents the thermal dissipation. In equation (2.14), q is a vector, which denotes the heat flux.

2.4 Introduction of dissipation potential

The yield surface and loading-unloading criterion in time-independent plasticity is replaced by a series of equipotential surfaces in viscoplasticity. In stress space, each of these equipotential surfaces contains the points, which have the same magnitude of strain-rate. This can also be understood that all points on an equipotential surface have the same dissipation. The surface of zero potential corresponds to the elastic domain, which can be referred to figure 2.1.

The dissipation potential must be a convex function with regard to each of the variables $\underline{\underline{\sigma}}$, $\underline{\underline{X}}$, R, M_k. It can be expressed in a dual form based on the concept of equipotential surface:

$$\Omega = \Omega\left(\underline{\underline{\sigma}}, \underline{\underline{X}}, R, M_k; T, \underline{\underline{\alpha}}, r, m_k\right), \tag{2.15}$$

In addition the dissipation potential must be positive defined. When the magnitudes of $\underline{\underline{\sigma}}$, $\underline{\underline{X}}$, R, M_k equal zero, the dissipation potential should also be zero.

Based on the normality rule, the following expression can be obtained:

$$\underline{\underline{\dot{\varepsilon}}}_p = \frac{\partial \Omega}{\partial \underline{\underline{\sigma}}}, \quad \underline{\underline{\dot{\alpha}}} = -\frac{\partial \Omega}{\partial \underline{\underline{X}}}, \quad \dot{r} = -\frac{\partial \Omega}{\partial R}, \quad \dot{m}_k = -\frac{\partial \Omega}{\partial M_k}. \tag{2.16}$$

Consequently the intrinsic dissipation can be modified to:

$$\Phi_1 = \underline{\underline{\sigma}} : \frac{\partial \Omega}{\partial \underline{\underline{\sigma}}} + \underline{\underline{X}} : \frac{\partial \Omega}{\partial \underline{\underline{X}}} + R \frac{\partial \Omega}{\partial R} + M_k \frac{\partial \Omega}{\partial M_k} \geq 0. \tag{2.17}$$

For viscoplasticity, which contains recovery effects, the dissipation potential can be decomposed to two parts:

$$\Omega = \Omega_p + \Omega_r, \tag{2.18}$$

$$\Omega_p = \Omega_p(J_2(\underline{\underline{\sigma}} - \underline{\underline{X}}) - R - k, \underline{\underline{X}}, R, M_k; T, \underline{\underline{\alpha}}, r, m_k), \tag{2.19}$$

$$\Omega_r = \Omega_r(\underline{\underline{X}}, R, M_k; T, \underline{\underline{\alpha}}, r, m_k). \tag{2.20}$$

in which Ω_p denotes the viscoplastic potential; Ω_r denotes the recovery potential. $J_2(\underline{\underline{\sigma}} - \underline{\underline{X}})$ represents a norm in stress space. Based on von Mises criterion it gives:

$$J_2(\underline{\underline{\sigma}} - \underline{\underline{X}}) = \sqrt{\frac{3}{2}(\underline{\underline{\sigma}}' - \underline{\underline{X}}') : (\underline{\underline{\sigma}}' - \underline{\underline{X}}')}, \tag{2.21}$$

in which $\underline{\underline{\sigma}}'$ and $\underline{\underline{X}}'$ are the deviators of $\underline{\underline{\sigma}}$ and $\underline{\underline{X}}$.

According to the normality rule, the viscoplastic flow rule gives:

$$\dot{\underline{\underline{\varepsilon}}}_p = \frac{\partial \Omega}{\partial J_2(\underline{\underline{\sigma}} - \underline{\underline{X}})} \frac{J_2(\underline{\underline{\sigma}} - \underline{\underline{X}})}{\partial \underline{\underline{\sigma}}} = \frac{3}{2}\dot{p}\frac{\underline{\underline{\sigma}}' - \underline{\underline{X}}'}{J_2(\underline{\underline{\sigma}} - \underline{\underline{X}})}, \tag{2.22}$$

where p is so-called accumulated strain, which gives:

$$\dot{p} = \sqrt{\frac{2}{3}\dot{\underline{\underline{\varepsilon}}}_p : \dot{\underline{\underline{\varepsilon}}}_p}. \tag{2.23}$$

Additionally, the expression of internal variable r can be obtained likewise:

$$\dot{r} = \dot{p} - \frac{\partial \Omega_r}{\partial R}. \tag{2.24}$$

When recovery effects are neglectable, $\Omega_r = 0$, the internal variable r is equal to the accumulated plastic strain p.

2.5 Perfect viscoplasticity

In the case of perfect viscoplasticity, there is no hardening effect, therefore the internal variables are absent. The dissipation potential in perfect viscoplasticity can be defined as:

$$\Omega = \Omega(\underline{\underline{\sigma}};T).\tag{2.25}$$

Based on the assumption of plastic incompressibility and the independence between the yield state and hydrostatic stress, it is sufficient to use the deviatoric stress tensor:

$$\underline{\underline{\sigma}}' = \underline{\underline{\sigma}} - \frac{1}{3}(\underline{\underline{\sigma}}:\underline{\underline{I}})\underline{\underline{I}}.\tag{2.26}$$

In addition, according to the isotropic criteria, the invariants of the deviatoric stress tensor $\underline{\underline{\sigma}}'$ can be used, so that:

$$\Omega = \Omega\big(J_2(\underline{\underline{\sigma}}), J_3(\underline{\underline{\sigma}});T\big),\tag{2.27}$$

with $J_2(\underline{\underline{\sigma}}) = \sqrt{\dfrac{3}{2}\underline{\underline{\sigma}}':\underline{\underline{\sigma}}'}$, and $J_3(\underline{\underline{\sigma}}) = \sqrt[3]{\dfrac{9}{2}Tr(\underline{\underline{\sigma}}'^3)}$.

In general, the third invariant can be neglected, so that the von Mises criterion based viscoplastic potential can be obtained:

$$\Omega = \Omega\big(J_2(\underline{\underline{\sigma}});T\big),\tag{2.28}$$

Using normality rule, the flow rule of the viscoplasticity can be defined:

$$\dot{\underline{\underline{\varepsilon}}}_p = \frac{\partial\Omega}{\partial\underline{\underline{\sigma}}} = \frac{3}{2}\frac{\partial\Omega}{\partial J_2(\underline{\underline{\sigma}})}\frac{\underline{\underline{\sigma}}'}{J_2(\underline{\underline{\sigma}})}.\tag{2.29}$$

A definition of the dissipation potential function is supplied by Odqvist's law [19] for perfect viscoplasticity, in which elastic part is not considered and the elastic domain is diminished to origin point. In this definition, the dissipation potential function is expressed by a power function:

$$\Omega = \frac{\lambda^*}{N^*+1}\left(\frac{J_2(\underline{\underline{\sigma}})}{\lambda^*}\right)^{N^*+1},\tag{2.30}$$

where λ^* and N^* are material constants. Consequently the flow rule gives:

$$\dot{\underline{\underline{\varepsilon}}}_p = \frac{3}{2}\left(\frac{J_2(\underline{\underline{\sigma}})}{\lambda^*}\right)^{N^*}\frac{\underline{\underline{\sigma}}'}{J_2(\underline{\underline{\sigma}})}.\tag{2.31}$$

Due to the absence of hardening and the elastic domain, the perfect viscoplasticity based on the Odqvist's law is simple to be modelled in numerical calculations.

The Odqvist's law can also be generalized to incorporate the elastic domain. By introducing the initial size of elastic domain k, the dissipation potential can be modified to:

$$\Omega = \frac{\lambda^*}{N^*+1} \left\langle \frac{J_2(\underline{\underline{\sigma}})-k}{\lambda^*} \right\rangle^{N^*+1} , \qquad (2.32)$$

with $\langle F \rangle := F \cdot H(F)$ and $H(F) := \begin{cases} 1 & if \quad F \geq 0 \\ 0 & if \quad F < 0 \end{cases}$,

where $H(F)$ is so-called Heaviside step function and the $\langle \rangle$ indicates the loading-unloading criterion. Finally, the viscoplastic strain-rate gives:

$$\dot{\underline{\underline{\varepsilon}}}_p = \frac{3}{2} \left\langle \frac{J_2(\underline{\underline{\sigma}})-k}{\lambda^*} \right\rangle^{N^*} \frac{\underline{\underline{\sigma}}'}{J_2(\underline{\underline{\sigma}})} . \qquad (2.33)$$

2.6 Viscoplasticity with kinematic and isotropic hardening

To improve the viscoplastic material model, internal variables of describing kinematic hardening and isotropic hardening should be introduced simultaneously. The application of kinematic hardening variable is helpful to describe the yield curve and hysteresis loop more accurately, while the employment of isotropic hardening variable provides the possibility to simulate cyclic hardening or softening effect.

Kinematic hardening and isotropic hardening are introduced in free energy by using internal variables $\underline{\underline{\alpha}}$ and r and their thermodynamic forces. In the absence of recovery processes, they give:

$$\underline{\underline{X}} = \rho \left(\frac{\partial \Psi}{\partial \underline{\underline{\alpha}}} \right) \text{ and } R = \rho \left(\frac{\partial \Psi}{\partial r} \right) = \rho \left(\frac{\partial \Psi}{\partial p} \right). \qquad (2.34)$$

Consequently the dissipation potential can be expressed by:

$$\Omega = \Omega\left(\underline{\underline{\sigma}}, \underline{\underline{X}}, R; T, \underline{\underline{\alpha}}, p\right) \quad . \tag{2.35}$$

Keeping $\underline{\underline{\alpha}}$ and p in the expression of dissipation potential, the free energy and the dissipation potential can be written in general forms:

$$\rho\Psi = \rho\Psi_e + \frac{1}{3}c\underline{\underline{\alpha}}:\underline{\underline{\alpha}} + h(p), \tag{2.36}$$

$$\Omega = \Omega\left(J_2(\underline{\underline{\sigma}} - \underline{\underline{X}}) - R - k + \frac{1}{2}\frac{\gamma}{c}J_2^2(\underline{\underline{X}}) - \frac{2}{9}c\gamma J_2^2(\underline{\underline{\alpha}}); T, p\right), \tag{2.37}$$

in which k, c, γ are parameters depending on temperature. k corresponds to the initial size of elastic domain.

Based on equation (2.34) and (2.36), the thermodynamic variables can be deduced to:

$$\underline{\underline{X}} = \frac{2}{3}c\underline{\underline{\alpha}}, \text{ and } R = h'(p) = \rho\left(\frac{\partial\Psi}{\partial p}\right). \tag{2.38}$$

By using normality rule, the following evolution equations can be obtained:

$$\dot{\underline{\underline{\varepsilon}}}_p = \frac{\partial\Omega}{\partial\underline{\underline{\sigma}}} = \frac{3}{2}\frac{\partial\Omega}{\partial J_2(\underline{\underline{\sigma}} - \underline{\underline{X}})}\frac{\underline{\underline{\sigma}}' - \underline{\underline{X}}}{J_2(\underline{\underline{\sigma}} - \underline{\underline{X}})}, \tag{2.39}$$

$$\dot{p} = -\frac{\partial\Omega}{\partial R} = \frac{\partial\Omega}{\partial J_2(\underline{\underline{\sigma}} - \underline{\underline{X}})} = \sqrt{\frac{2}{3}\dot{\underline{\underline{\varepsilon}}}_p : \dot{\underline{\underline{\varepsilon}}}_p}, \tag{2.40}$$

$$\dot{\underline{\underline{\alpha}}} = -\frac{\partial\Omega}{\partial R} = \dot{\underline{\underline{\varepsilon}}}_p - \frac{3}{2}\frac{\gamma}{c}\underline{\underline{X}}\dot{p}. \tag{2.41}$$

Inserting equation (2.41) into equation (2.38), it gives:

$$\dot{\underline{\underline{X}}} = \frac{2}{3}c\dot{\underline{\underline{\varepsilon}}}_p - \gamma\underline{\underline{X}}\dot{p}. \tag{2.42}$$

The isotropic hardening can be formulated in a simplest form:

$$\dot{R} = b(Q - R)\dot{p}, \tag{2.43}$$

in which b, Q are two material parameters, which may depend on the temperature. Based on this viscoplastic model with the superposition of kinematic hardening and isotropic hardening, a so-called unified viscoplastic model was developed by Chaboche. In the frame of this work, the unified Chaboche model was extended and optimized in order to study the multiaxial ratchetting behaviour and the effect of non-proportional loading.

2.7   Introduction of ratchetting phenomenon

Generally speaking, ratchetting phenomenon can be classified into mechanical ratchetting and thermal ratchetting. Mechanical ratchetting is evoked when components are subjected to a sustained extensional load acting over the full cross section or thickness in combination with a strain controlled cyclic load, which yields plastification. Thermal ratchetting can be detected, if a sustained extensional load is acting over the full cross section or thickness of components in combination with a temperature distribution, which is alternately applied and removed. Ratchetting causes cyclic straining, which produces a cyclic incremental growth of plastification of the structure and can ultimately lead to incremental collapse [20].

This research work was focused on mechanical ratchetting in components, which results from a superposition of constant load and strain controlled cyclic load simultaneously. The constant stress caused by sustained constant load, or mean-stress in uniaxial stress state, can be understood as primary stress, e.g. an internal pressure of a pipe or a constant longitudinal tension, while the cyclic stress induced by the cyclic load can be understood as secondary stress. The concept of primary and secondary stresses is commonly applied in literatures on ratchetting. They should be differentiated from the stress definitions in KTA. If the superposition of primary and secondary stresses is locally bounded, e.g. at notches or a locally heated position, local ratchetting can arise.

Subjected to the primary and secondary stresses, an irreversible inelastic deformation is induced and accumulated in the direction of load which yields primary stress. The corresponding inelastic strain is defined as ratchetting strain. The occurrence of ratchetting may cause unpredictable large straining and yield earlier failure of components,

therefore the ratchetting should be limited in service procedure of mechanical components.

With the increase of load cycles, the accumulation procedure of ratchetting strain can be distinguished into the following two stages:

Transient ratchetting: As shown in figure 2.2, transient ratchetting arises at the beginning of cyclic loading. During the start-up stage, the transient ratchetting increases rapidly. With the increase of load cycles, the gradient of transient ratchetting decreases gradually.
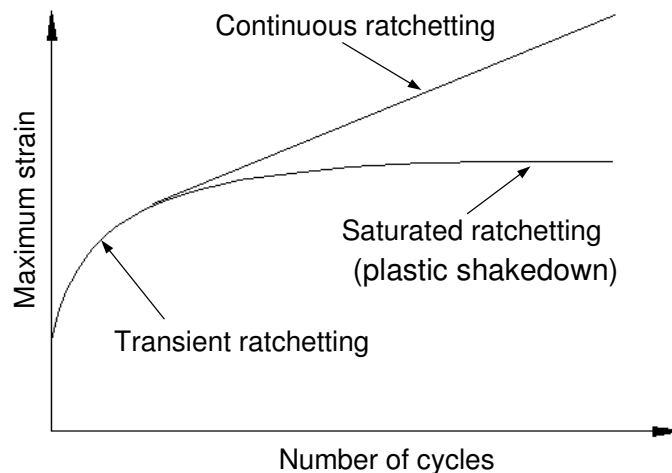
Figure 2.2: Schematic illustration of transient and asymptotic ratchetting.

Asymptotic ratchetting: A procedure corresponds to a stabilized state of ratchetting strain increase, which arises after the stage of transient ratchetting. Based on different behaviour, asymptotic ratchetting can be classified into continuous ratchetting and saturated ratchetting. The continuous ratchetting is defined as a linear increase of ratchetting strain with a certain gradient. If the ratchetting strain reaches a stable state and the increase terminates after a certain number of cycles, this phenomenon is defined as saturated ratchetting or plastic shakedown [53].

2.7.1 Uniaxial ratchetting

Mechanical ratchetting arises not only under multiaxial loading but also under cyclic uniaxial loading. For uniaxial ratchetting, a tension-compression stress-controlled test

with a mean-stress should be considered. In uniaxial stress-state, the mean-stress is considered as primary load, while the cyclic stress is considered as secondary one. If the stress-range of the secondary load is greater than twice of the yield limit, the plastification and hardening occur during both loading and unloading processes. The procedure of ratchetting can be illustrated by using figure 2.3.
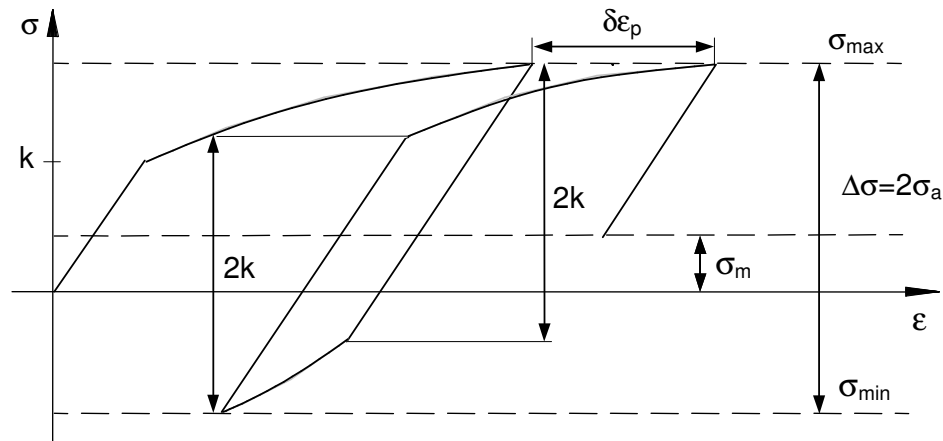

Figure 2.3: Schematic illustration of ratchetting under uniaxial, stress-controlled loading with mean-stress [54].

As shown in figure 2.3, starting from an initial undeformed state, material is elastically loaded till yield limit k. After the yield limit is exceeded, the plastification and hardening occur. The hardening proceeds by following the characteristic hardening curve until the reverse point of loading direction, which corresponds to a maximum stress σ_{max}. Subsequently, unloading procedure begins. After material passes the elastic range of 2k, it starts to yield and harden in compression. Due to the influence of the cyclic hardening behaviour of the material, the progress of the plastic flow shows a steeper gradient than that in loading procedure. After reaching the minimum stress σ_{min}, the load direction changes; while a new loading procedure starts. The material first passes the elastic range of 2k, and then it proceeds with yielding and hardening again. After reaching the maximum stress σ_{max}, an increment of inelastic strain, $\delta\varepsilon_p$, is attained. This inelastic strain is not reversible and will accumulate gradually with the increase of loading cycles. The amount of the inelastic strain depends on mean-stress, stress-amplitude, as well as kinematic hardening and isotropic hardening/softening behaviour of material.

Under uniaxial loading with nonzero mean-stress and nonzero inelastic strain-range, there exists always transient ratchetting. Saturated ratchetting takes place eventually after transient ratchetting. If mean-stress increases under a constant kept stress-range, transient ratchetting increases too. In addition, saturated ratchetting may be replaced by continuous ratchetting, and the gradient of continuous ratchetting is also influenced by mean-stress. Likewise, if mean-stress is kept as constant, the increase of stress-range leads to not only an increase of corresponding strain-range but also an increase of ratchetting. Nevertheless it is difficult to find a clear correlation between the increase of ratchetting strain and inelastic strain-range from experimental results.

2.7.2 Multiaxial ratchetting

In multiaxial stress-state, ratchetting may arise too. If component is subjected to constant loading in one direction and cyclic alternating loading in another direction, which yields plastification, ratchetting strain is evoked in the direction of constant stress. A typical example of multiaxial ratchetting can be explained by using a straight pipe component, which is loaded by a constant axial loading and strain-controlled cyclic torsion which yields cyclic plastification. In this case, the constant axial loading acts as the primary load, while the cyclic torsion acts as the secondary load.

Multiaxial ratchetting shows approximately the same characteristics as uniaxial ratchetting. Namely, ratchetting starts from transient ratchetting and transforms to continuous ratchetting or saturated ratchetting successively. Nevertheless it has been proved by many previous work and experiments that the magnitude of multiaxial ratchetting is obviously smaller than that of uniaxial ratchetting under comparable loading conditions [21].

3 Constitutive model

In classical plasticity, one of initial constitutive models can be traced back to Bingham model [22][23]. This model assumes that material starts to flow only if the applied forces exceed yield limit. Before reaching yield limit the deformations are zero. Bingham model was improved to an elastic-plastic model by Prager [24][25]. In Hohenemer-Prager model, it is assumed that, even below the yield limit, strain increases simultaneously with stress based on the Hooke's law. After stress reaches yield limit the deformation of the material is dominated by a plastic constitutive model.

Based on above mentioned material models, many progresses have been achieved in the development of constitutive equations to describe the viscoplasticity of metals under cyclic loading in the last two decades. These constitutive models can be generally classified into two approaches depending on different material states [26].

Regarding the first approach, material behaviour can be described completely by current material state, which only depends on current physically accessible variables, e.g. stress, strain, time, temperature, number of cycles, and internal variables, although the same material state can be attained by applying different loading paths. This approach was first applied for time-independent plasticity by using the concepts of yield surface, multiple layer [27], multiple yield surface [28], or two surfaces [29][30]. The time-dependent effects was introduced by separating plastic and creep strains [31], incorporating the coupling effects in hardening rules [32], or applying a unified viscoplastic model [33].

The second approach assumes that the material state depends not only on current physically accessible values but also on the previous history of these values. The application of this approach can be found in some literatures, for example [34]-[36]. An example of this approach is so-call strain-memory-effect, in which the previous reached maximum plastic strain affects the current material state.

Among developed constitutive models, Armstrong-Frederick-Chaboche model (AFC-model) was widely applied to describe the cyclic behaviour for time independent plasticity [37]-[40]. This material model has numerous ramifications, which contain different

evolution equations for the description of kinematic and isotropic hardening. By extending the elastic-plastic AFC-model, a viscoplastic model was obtained by introducing the viscoplastic flow rule [41]. This is so-called viscoplastic Chaboche model, in which plastic strain and viscous strain are combined into a unique viscoplastic strain, so that there is no separation of strain-hardening (hardening due to deformation) and time-hardening (hardening due to time) in this model. Since viscoplastic strain incorporates both items simultaneously or successively, strain-rate does not exhibit any discontinuities under any kind of loading. By using viscoplastic strain, the description of the interaction between fatigue and creep is available. Based on the description above, the viscoplastic Chaboche model can be named as unified Chaboche model. In the frame of this work, the constitutive modelling is based on the unified viscoplastic model by superposing kinematic hardening, isotropic hardening evolution equations and strain-memory-effect.

3.1 Flow condition

As discussed in previous chapter, viscous effect can be introduced by using so-called equipotential surfaces [42]. A pure elastic domain in viscoplasticity still can be assumed. The major difference from time-independent plasticity is that viscoplastic model assumes a viscous stress-state beyond the yield surface. By using the von Mises criterion and the normality rule, the flow condition is extended by introducing kinematic and isotropic hardening variables:

$$f = J_2\left(\underline{\underline{\sigma}} - \underline{\underline{X}}\right) - R - k > 0 \text{, with } J_2\left(\underline{\underline{\sigma}} - \underline{\underline{X}}\right) = \sqrt{\frac{3}{2}\left(\underline{\underline{\sigma}}' - \underline{\underline{X}}'\right):\left(\underline{\underline{\sigma}}' - \underline{\underline{X}}'\right)}, \qquad (3.1)$$

where $\underline{\underline{X}}$ and R are two internal variables. Kinematic hardening variable $\underline{\underline{X}}$, can also be named as back-stress. Isotropic hardening variable R is a scalar variable. These two internal variables together give the position and the size of equipotential surface. The constant k is a material parameter, which represents the initial size of elastic domain.

3.2 Flow rule

After reaching yield limit, the increment of viscoplastic strain at current stress-state is perpendicular to the equipotential surface. This is so-called the normality rule. Therefore the viscoplastic flow fulfils $f > 0$ and $\dfrac{\partial f}{\partial \underline{\underline{\sigma}}} : \dot{\underline{\underline{\sigma}}} > 0$.

By using the concept of equipotential surfaces, the stress-state in excess of the elastic domain leads to a dissipation potential. In an extreme case, the elastic domain corresponds to the surface of zero potential. The dissipation potential can be written as a power function [43]:

$$\Omega_p = \frac{Z}{n+1} \left\langle \frac{J_2\left(\underline{\underline{\sigma}} - \underline{\underline{X}}\right) - R - k}{Z} \right\rangle^{n+1} , \tag{3.2}$$

in which Z and n are material dependent parameters.

Based on the normality rule, the viscoplastic flow rule can be obtained:

$$\dot{\underline{\underline{\varepsilon}}}_p = \frac{\partial \Omega}{\partial \underline{\underline{\sigma}}} = \frac{3}{2} \frac{\partial \Omega}{\partial J_2(\underline{\underline{\sigma}} - \underline{\underline{X}})} \frac{\underline{\underline{\sigma}}' - \underline{\underline{X}}'}{J_2(\underline{\underline{\sigma}} - \underline{\underline{X}})} = \frac{3}{2} \dot{p} \frac{\underline{\underline{\sigma}}' - \underline{\underline{X}}'}{J_2(\underline{\underline{\sigma}} - \underline{\underline{X}})} , \tag{3.3}$$

in which:

$$\dot{p} = \frac{\partial \Omega}{\partial J_2(\underline{\underline{\sigma}} - \underline{\underline{X}})} = \left\langle \frac{J_2\left(\underline{\underline{\sigma}} - \underline{\underline{X}}\right) - R - k}{Z} \right\rangle^{n} . \tag{3.4}$$

Here $\dot{p}$ is so-called accumulated viscoplastic strain rate. It can be also expressed by the magnitude of the viscoplastic strain rate $\dot{\varepsilon}_p$:

$$\dot{p} = \left(\frac{2}{3} \dot{\underline{\underline{\varepsilon}}}_p : \dot{\underline{\underline{\varepsilon}}}_p \right)^{\frac{1}{2}} \tag{3.5}$$

Corresponding to viscoplastic potential, an over stress or viscous stress can be defined:

$$\sigma_{vis} = J_2\left(\underline{\underline{\sigma}} - \underline{\underline{X}}\right) - R - k . \tag{3.6}$$

Inserting equation (3.6) into equation (3.4), the viscous stress can be written as the power function of the accumulated viscoplastic strain rate:

$$\sigma_{vis} = Z \cdot \dot{p}^{1/n} .$$ (3.7)

3.3 Kinematic hardening

To describe direction-dependent hardening procedure, evolution equation of kinematic hardening is introduced. The first approach of kinematic hardening can be traced back to Prager [24]. Further developments were reported in [44]. Prager applied a linear approach to describe kinematic hardening. Therefore the approach is also named as the linear kinematic hardening approach (LK). The relationship between kinematic hardening variable and the viscoplastic strain-rate is expressed by:

$$\underline{\dot{X}} = \frac{2}{3} c \underline{\dot{\varepsilon}}_p ,$$ (3.8)

in which c is a material parameter.

3.3.1 Armstrong and Frederick approach

The LK approach builds up a linear relationship between kinematic hardening and viscoplastic strain. It was applied in several constitutive theories [45]-[48]. However this approach is insufficient to describe ratchetting behaviour, since the kinematic hardening variable and viscoplastic strain are always in-phase. The drawback of the LK approach can be eliminated by introducing a dynamic recovery by means of an additional nonlinear term, which is so-called recall term. This kind of nonlinear kinematic hardening (NLK) approach was initially introduced by Armstrong and Frederick [49]:

$$\underline{\dot{X}} = \frac{2}{3} c \underline{\dot{\varepsilon}}_p - \gamma \underline{X} \dot{p} ,$$ (3.9)

where c and γ are material-dependent parameters. This formulation describes not only the dependence on viscoplastic strain increment but also the current displacement of the equipotential surface. It can be schematically illustrated in figure 3.1.
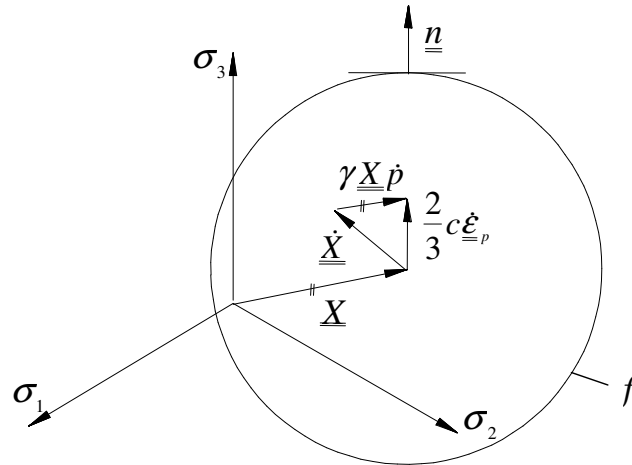
Figure 3.1: Illustration of the NLK approach in deviatoric of the principal-stress space under multiaxial loading.

It can be detected that the increment of kinematic hardening variable is composed of two parts. One is perpendicular to the equipotential surface, and the other corresponds to the recall term, which is parallel to the kinematic hardening variable $\underline{\underline{X}}$ and with respect to the accumulated viscoplastic strain-rate $\dot{p}$. Consequently, equation (3.9) is able to describe the rapid change due to the plastic flow during cyclic loading. That means, that the transient hardening effects in each stress-strain loop is taken into account. This NLK approach was widely used before, e.g. in [50][51]. The advantages of this rule are:

1. The explicit integrability under proportional loading.

2. The nonlinearity of the stress-strain evolutions, the nonuniqueness of the relation between kinematic hardening variable and inelastic strain, and the corresponding modelling of Bauschinger effects.

3. The description of ratchetting and mean-stress relaxation effects under non-symmetrical cyclic loadings.

3.3.2 Improvements of NLK approach by Chaboche

Nevertheless one of the main limitations by using Armstrong-Frederick approach is that the strain-range $\Delta\varepsilon$, for which the kinematic hardening variable is applied, is limited. Corresponding to the increase of strain, the kinematic hardening calculated by Armstrong-Frederick approach presents saturation. The speed of the saturation depends on the material parameters in equation (3.9). If the parameters are chosen to represent small strains correctly (e.g. $\Delta\varepsilon < 0.5\%$), the hardening effects of large strains (e.g. $\Delta\varepsilon > 1.0\%$) can not be properly predicted.

To improve the kinematic hardening approach for larger strain-range, more kinematic variables should be introduced, so that after the first kinematic hardening variable is saturated the hardening can be described by the other kinematic hardening variables. Therefore a generalization can be made to Armstrong-Frederick model, which decomposes the kinematic hardening variable into M components [52][53]:

$$\underline{\underline{X}} = \sum_{i=1}^{M} \underline{\underline{X}}_i \ .$$
(3.10)

The Armstrong-Frederick kinematic hardening approach is applied in each component:

$$\underline{\dot{\underline{X}}}_i = \frac{2}{3} c_i \underline{\dot{\underline{\varepsilon}}}_p - \gamma_i \underline{\underline{X}}_i \dot{p} \ .$$
(3.11)

Based on previous research from Krolop, Stegmeyer, and Scheffold [54][55][56], a further improvement of equation (3.10) and (3.11) can be obtained:

$$\underline{\dot{\underline{X}}}_1 = \frac{2}{3} c_1 \underline{\dot{\underline{\varepsilon}}}_p - \gamma_1 \underline{\underline{X}}_1 \dot{p} \ ,$$
(3.12)

$$\underline{\dot{\underline{X}}}_2 = \frac{2}{3} c_2 \underline{\dot{\underline{\varepsilon}}}_p - \gamma_2 \underline{\underline{X}}_2 \dot{p} \ ,$$
(3.13)

$$\underline{\dot{\underline{X}}}_3 = \frac{2}{3} c_3 \underline{\dot{\underline{\varepsilon}}}_p - \beta_3 \underline{\underline{X}}_3 \dot{p} \ ,$$
(3.14)

$$\text{with } \beta_3 = \begin{cases} \gamma_{31} & \text{for} \quad J_2(\underline{\underline{X}}_3) \le X_L \\ \gamma_{32}\left(1 - \dfrac{X_L}{J_2(\underline{\underline{X}}_3)}\right) & \text{for} \quad J_2(\underline{\underline{X}}_3) > X_L \end{cases} ; \quad \gamma_{31} << \gamma_{32} \ ,$$

$$\dot{\underline{\underline{X}}}_4 = \frac{2}{3} c_4 \dot{\underline{\underline{\varepsilon}}}_p - \gamma_4 \underline{\underline{X}}_4 \dot{p} \, , \tag{3.15}$$

$$\underline{\underline{X}} = \underline{\underline{X}}_1 + \underline{\underline{X}}_2 + \underline{\underline{X}}_3 + \underline{\underline{X}}_4 \, . \tag{3.16}$$

Here four kinematic hardening variables were applied by Krolop, Stegmeyer and Scheffold in their AFC model to study the cyclic plastic and ratchetting behaviour. In equation (3.14), the third kinematic hardening variable was modified based on the evolution equation from Chaboche [57], in which a parameter, so-called threshold value X_L, is introduced in the recall term. The parameter X_L plays the role of a limit for accommodation. γ_{31} and γ_{32} are two material parameters with different values. That is, γ_{32} is much larger than γ_{31}. When $J_2(\underline{\underline{X}}_3)$ is less than X_L, only linear term is activated. If $J_2(\underline{\underline{X}}_3)$ exceeds X_L, the recall term contributes to kinematic hardening gradually. Namely, with the increase of plastic strain, the magnitude of the recovery contributed by the third kinematic hardening variable increases. Consequently, a more conservative and steady strain increase for ratchetting can be obtained by this modification.

In summary, the application of the threshold value in the recall term can decrease the hardening modulus for tensile curves, provide better shapes for the stress-strain hysteresis loops and predict modest ratchetting deformation for low mean-stress. In addition, it also presents better nonlinearity of ratchetting strain as a function of the mean-stress.

3.3.3 Ohno and Wang approaches

It is known that the simulation of ratchetting behaviour is dominated by the modelling of kinematic hardening. As described in previous chapters, the Armstrong and Frederick approach is initially widely used and improved by Chaboche etc.[21],[57]-[59]. Nevertheless concerning the quantitative calculation of ratchetting deformation, these kinematic hardening approaches are still far from accurate, since they lead to very large overestimates of ratchetting under both uniaxial and multiaxial stress-states [21][57][60]-[61]

To decrease the overestimate of the ratchetting deformation, Ohno and Wang developed two different kinematic hardening approaches [62]:

$$\text{Approach I:} \quad \underline{\dot{X}}_i = \frac{2}{3} c_i \underline{\dot{\varepsilon}}_p - \gamma_i H(f_i) \sqrt{\frac{3}{2}} \left\langle \underline{n} : \underline{k}_i \right\rangle \underline{X}_i \dot{p} , \quad (3.17)$$

$$\text{Approach II:} \quad \underline{\dot{X}}_i = \frac{2}{3} c_i \underline{\dot{\varepsilon}}_p - \gamma_i \left(\frac{J_2(\underline{X}_i)}{h_i} \right)^{m_i} \sqrt{\frac{3}{2}} \left\langle \underline{n} : \underline{k}_i \right\rangle \underline{X}_i \dot{p} , \quad (3.18)$$

in which $h_i = \dfrac{c_i}{\gamma_i}$ and m_i are material parameters. Ohno and Wang's kinematic hardening approaches are formulated in a hardening-dynamic recovery format, which is similar to Armstrong-Frederick approach.

In micromechanical scale, the dynamic recovery of kinematic hardening concerns the cross slip of dislocation piled-up to obstacles [63]. In approach I, it is assumed that the dynamic recovery of kinematic hardening variable $\underline{X}_i$ is fully activated only when the magnitude $J_2(\underline{X}_i)$ reaches a critical value resulting from the energy required for cross slip. The critical state of dynamic recovery is represented by a surface:

$$f_i = J_2(\underline{X}_i)^2 - h_i^2 = 0 . \quad (3.19)$$

Using the Heaviside function H(f) in the dynamic recovery term, the NLK approach $\underline{X}_i$ can be general written as:

$$\underline{\dot{X}}_i = \frac{2}{3} c_i \underline{\dot{\varepsilon}}_p - H(f_i) \dot{\lambda}_i \underline{X}_i , \quad (3.20)$$

in which the dynamic recovery activates only if $J_2(\underline{X}_i) = h_i$. The unknown parameter $\dot{\lambda}_i$ is determined by using the condition $\dot{f}_i = 0$, which is actualized only if $f_i = 0$ and $\underline{\dot{\varepsilon}}_p : \underline{k}_i \geq 0$:

$$\dot{\lambda}_i = \gamma_i \left\langle \underline{\dot{\varepsilon}}_p : \underline{k}_i \right\rangle = \sqrt{\frac{3}{2}} \gamma_i \left\langle \underline{n} : \underline{k}_i \right\rangle \dot{p} , \quad (3.21)$$

in which $\underline{k}_i$ denotes the direction of $\underline{X}_i$:

$$\underset{=i}{k} = \frac{\underset{=i}{X}}{J_2\left(\underset{=i}{X}\right)} .$$

(3.22)

Inserting equation (3.21) into (3.20), the approach I, equation (3.17), is achieved.

In approach I, the dynamic recovery is restrained inside the surface $f_i = 0$. Nevertheless it is partly allowed inside the surface $f_i = 0$ in the approach II. When the magnitude $J_2\left(\underset{=i}{X}\right)$ approaches the critical value h_i, the dynamic recovery takes place gradually. When the kinematic hardening variable $\underset{=i}{X}$ reaches the surface $f_i = 0$, complete dynamic recovery is activated. Based on above description, the approach II can be modified from the approach I by introducing the coefficient $\left(\dfrac{J_2\left(\underset{=i}{X}\right)}{h_i}\right)^{m_i}$ instead of the critical value in the dynamic recovery term.
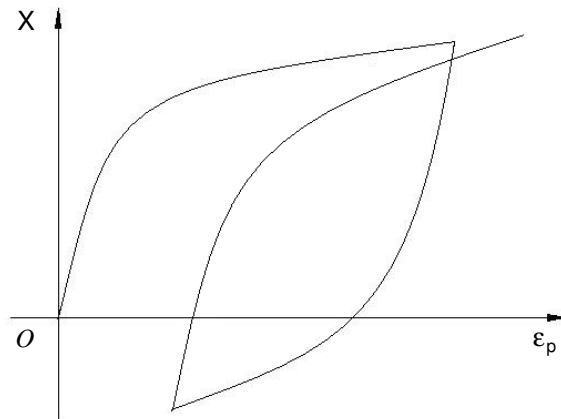
Compared to the Armstrong-Frederick approach, equation (3.9), Krolop-Stegmeyer-Scheffold model, equations (3.12)-(3.15), and some other NLK approaches [67][68], Ohno and Wang's approach I and approach II are able to predict less accumulation of ratchetting strain under both uniaxial and multiaxial loading. For instance, under uniaxial cyclic loading with any mean-stress, approach I gives closed stress-strain hysteresis loop, as shown in figure 3.2a. Namely, Approach I predicts no ratchetting strain under uniaxial loading, although ratchetting still can be induced by the viscosity of materials by means of viscous stress [21]. Approach II predicts ratchetting strain, which depends on the material parameter m_i. In general, approach II predicts less ratchetting than Armstrong-Frederick approach, as shown in figure 3.2b [62] and figure 3.2c. In extreme cases, if m_i is equal to zero, approach II is reduced to Armstrong-Frederick approach; If m_i is infinite, approach II is reduced to approach I.
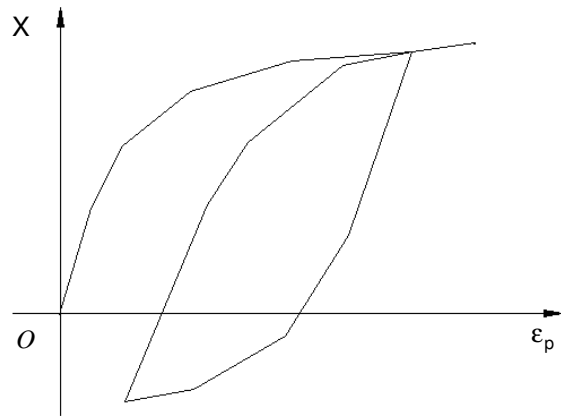
(a) Ohno-Wang approach I
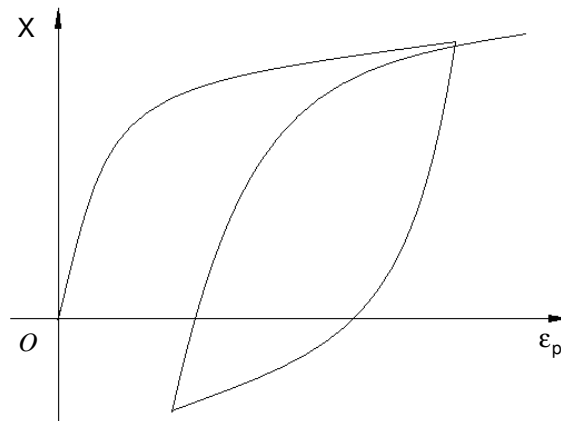
(b) Ohno–Wang approach II

(c) Armstrong-Frederick approach

Figure 3.2: Change of $\underline{\underline{X}}_i$ under cyclic loading,

Ohno-Wang approaches are also beneficial to take into account the multiaxial effect. In approach I and approach II, $\sqrt{\frac{3}{2}}\left\langle \underline{\underline{n}} : \underline{\underline{k}}_i \right\rangle$, is applied to build up the dynamic recovery term. Under multiaxial loading $\sqrt{\frac{3}{2}}\left\langle \underline{\underline{n}} : \underline{\underline{k}}_i \right\rangle \leq 1$, therefore $\sqrt{\frac{3}{2}}\left\langle \underline{\underline{n}} : \underline{\underline{k}}_i \right\rangle$ can be applied to diminish the dynamic recovery of the kinematic hardening variables and simulate less accumulation of multiaxial ratchetting strain [69].

Additionally, the same as Chaboche model and Krolop-Stegmeyer-Scheffold model, approach I and II from Ohno-Wang are characterized by the decomposition of the kinematic hardening into components too. Hence it is necessary to study the number of components of the kinematic hardening variable M. Ohno and Wang performed their calculation by using $M = 4$ and $M = 8$, respectively. In monotonic tensile, uniaxial cyclic loading and multiaxial cyclic loading calculations, the influence from M is very slight [62]. Since approaches I and II are insensitive to the uniaxial and multiaxial behaviour, if the number of components of kinematic hardening variable M is larger than four, it is sufficient to use four kinematic hardening variables in the constitutive model. This conclusion was also confirmed by the work of Krämer, Krolop, Scheffold and Stegmeyer [22][63][67].

3.3.4 Krämer-Krolop approach for multiaxial nonproportional cyclic loading

Nonproportional cyclic loading can be defined by a varying multiaxial cyclic loading procedure, in which the ratios between magnitudes of load components or loading directions are changing during cyclic loading. Compared to the case of proportional loading, more significant hardening behaviour can be observed under nonproportional cyclic loading. In addition, hardening under nonproportional loading also depends on loading path and the history of loading path. These features of hardening behaviour under nonproportional loading have already been presented in some literatures [29][68]. In this chapter an approach for taking into account the nonproportional hardening is discussed. It should be mentioned that the effect of nonproportional hardening is not related to the topic of ratchetting. However, since the simulation of this hardening behaviour can be also realized by using the kinematic hardening variable, it is discussed also in this work.

For taking into account the effect of nonproportional hardening, an additional internal variable p^* was introduced in the following evolution equation by Krolop et al.[52]:

$$\dot{p}^* = c'' |\sin \varphi| \dot{p} + c''' \kappa |\sin \varphi| \dot{p} , \tag{3.23}$$

$$\text{with} \quad \varphi := \arccos \left[\frac{\dot{\underline{\underline{\varepsilon}}}_p : \underline{\underline{\varepsilon}}_p}{\left\| \dot{\underline{\underline{\varepsilon}}}_p \right\| \left\| \underline{\underline{\varepsilon}}_p \right\|} \right] ,$$

$$\text{and} \, \kappa := \sqrt{\frac{2}{3}} \left| \frac{d}{dp} \left(\frac{\dot{\underline{\underline{\varepsilon}}}_p}{\left| \dot{\underline{\underline{\varepsilon}}}_p \right|} \right) \right| = \sqrt{\frac{2}{3}} \left| \frac{d\underline{\underline{n}}}{dp} \right| ,$$

where c'' and c''' are two material parameters. Variable φ describes the angel between viscoplastic strain and viscoplastic strain-rate, and variable κ denotes a relationship between the normal of equipotential surface $\underline{\underline{n}}$ and accumulated viscoplastic strain.

By using the internal variable p^*, an additional hardening due to nonproportional cyclic loading can be incorporated through the amplification of the linear term or the reduction of the dynamic recovery term in Armstrong-Frederick model:

$$\dot{\underline{\underline{X}}} = \frac{2}{3}(c + c'(1 - e^{-p^*}))\dot{\underline{\underline{\varepsilon}}}_p - \gamma \underline{\underline{X}} \dot{p} , \tag{3.24}$$

$$\dot{\underline{\underline{X}}} = \frac{2}{3} c \dot{\underline{\underline{\varepsilon}}}_p - (\gamma - \gamma'(1 - e^{-p^*}))\underline{\underline{X}} \dot{p} . \tag{3.25}$$

3.4 Isotropic hardening

Cyclic hardening and softening behaviour can be simulated by using the isotropic hardening variable in the unified viscoplastic Chaboche model. The isotropic hardening variable describes the extension and reduction of the size of elastic domain during the procedure of cyclic loading.

3.4.1 Cyclic saturated hardening

Chaboche introduced the following evolution equation for isotropic hardening:

$$\dot{R} = b(Q - R)\dot{p},$$
(3.26)

in which b and Q are material parameters. By using this first-order differential equation, the cyclic saturated hardening can be described. The parameter Q is a constant, which corresponds to the saturation of isotropic hardening. Nevertheless in real simulations, an isotropic hardening model, which is able to provide different saturation states for different loading conditions, is required. For instance, in a multiple step test, the strain-controlled cyclic loading is applied to specimen in a certain loading step. After a certain number of cycles, the isotropic hardening reaches saturation. In the following loading step, strain-amplitude is increased. The raise of the strain-amplitude invokes a new start of the isotropic hardening, which reaches saturation again after a certain number of cycles. Therefore the parameter Q should be defined as a function in regard to previous maximum reached inelastic strain in stead of a constant. The definition of the function Q can be carried out through strain-memory-effect, which will be discussed in chapter 3.4.4.

3.4.2 Cyclic neutral behaviour and cyclic non-saturated hardening

Based on the uniaxial tests of austenitic material X6 CrNiNb 18-10 with larger strain-amplitudes, the cyclic hardening with continuous increase instead of saturation was detected. Nevertheless above introduced Chaboche's evolution equation cannot describe this behaviour. Consequently equation (3.26) should be modified [68]:

$$\dot{R} = [b(Q - R)H(q_s - q_1) + aH(q_s - q_2)p]\dot{p},$$
(3.27)

with $H(F) := \begin{cases} 1 & if \quad F \geq 0 \\ 0 & if \quad F < 0 \end{cases}$,

where q_s denotes the radius of strain-memory-surface. q_1 and q_2 ($q_2 > q_1$) are two material parameters, which represent the limits of q_s. If $q_s < q_1$, equation (3.27) predicts a cyclic neutral behaviour, in which cyclic hardening or softening is absent; If

$q_s > q_2$, cyclic continuous hardening without saturation is presented; If q_s locates between q_1 and q_2, then equation (3.27) describes the same isotropic hardening behaviour as equation (3.26). The ratio between parameter a and b, a/b, defines the gradient of the asymptote of isotropic hardening variable as shown in figure 3.3.

The curves in figure 3.3 describe the change of isotropic hardening variable R, corresponding to equations (3.26) and (3.27), respectively. Under the same pre-condition $Q = R_s$ (where R_s denotes a saturation of isotropic hardening variable R) and $q_s > q_2$, two evolution equations present different isotropic hardening behaviour,: According to equation (3.26), a cyclic hardening reaches saturation with a certain accumulated viscoplastic strain. Whereas based on equation (3.27), the isotropic hardening variable R may exceed the saturation value R_s and proceeds along an asymptote with gradient a/b.
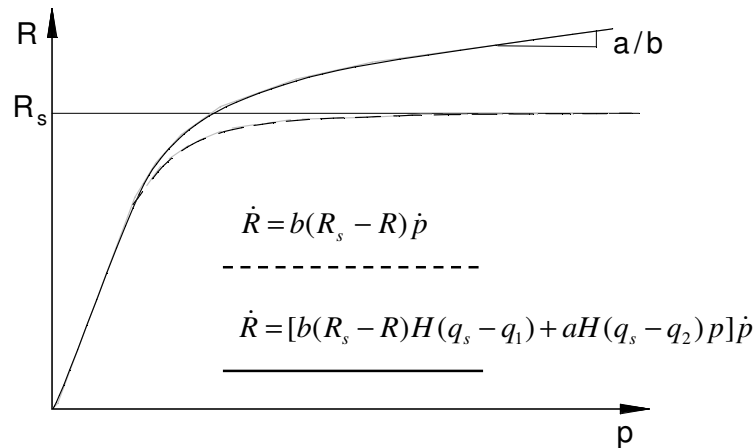
Figure 3.3: Comparison of two evolution equations for isotropic hardening.

.

3.4.3 Cyclic softening

To describe cyclic softening behaviour for metallic materials, an evolution equation was developed for isotropic hardening in this work:

$$\dot{R} = -b(Q + R)\dot{p} ,\tag{3.28}$$

which describes cyclic saturated softening behaviour, as shown in figure 3.4.

Furthermore, it was known that under certain loading conditions, the austenitic material X6 CrNiNb 18-10 and ferritic material 20 MnMoNi 5-5 present a combined hardening-softening cyclic behaviour, which presents a strong cyclic hardening at the onset of cyclic loading and successive cyclic softening after a certain number of cycles. Obviously equation (3.28) is not sufficient to describe this combined hardening-softening behaviour. Consequently, a new evolution equation was developed in this work:

$$\dot{R} = [a(cQ - R)H(q_1 - p) - b((1-c)Q + R)H(p - q_1)]\dot{p} ,\qquad\qquad (3.29)$$

$$\text{with } H(F) := \begin{cases} 1 & if \quad F \geq 0 \\ 0 & if \quad F < 0 \end{cases}$$

A characteristic of this model, which differs from above isotropic hardening models, is that the accumulated viscoplastic plastic strain p, instead of the radius of strain-memory-surface q_s, is applied to judge the state of cyclic hardening and softening. Through this modification, many numerical problems in FEM calculations can be avoided. Furthermore, in this new isotropic hardening model, only one threshold value q_1 is defined. If the accumulated viscoplastic strain p is less than the threshold value q_1, cyclic hardening arises. The magnitude of the cyclic hardening is determined by the product of c with Q. With the increase of loading cycles, the accumulated viscoplastic strain p increases simultaneously. If $p > q_1$, the hardening terminates and the cyclic softening starts, as shown in figure 3.4. The magnitude of the cyclic softening depends on the value of Q. Additionally, if q_1 is a positive infinity, the model describes a pure cyclic hardening; while if q_1 equals zero, it describes a pure cyclic softening. The parameter a, b and c define the shape of exponential cyclic hardening and softening curves. Parameters a and b determine the gradients of the exponential cyclic hardening and cyclic softening curves, respectively, while parameter c gives the ratio of the saturation values between the cyclic hardening and successive cyclic softening. Based on above description, it can be found out that the new evolution equation is able to depict cyclic behaviour flexibly: It can be used to describe cyclic hardening, cyclic softening as well as combined hardening-softening cyclic behaviour.
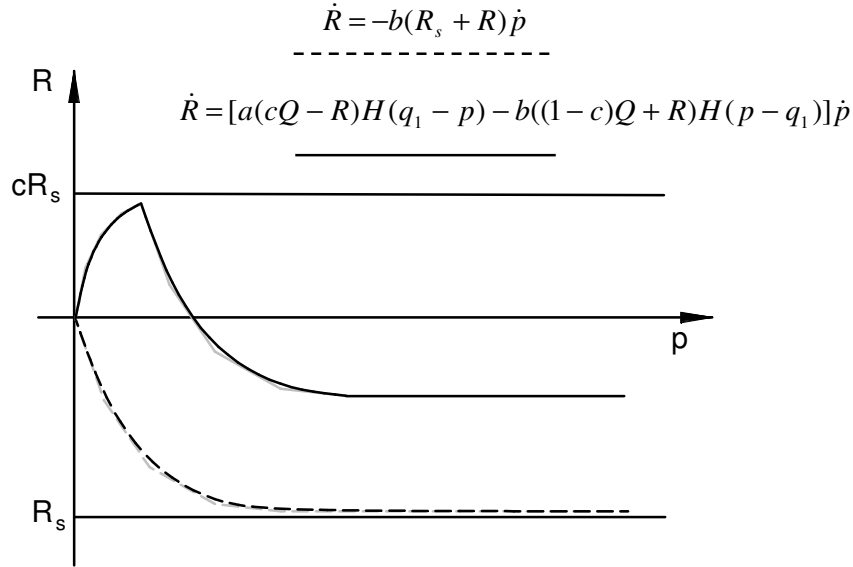
$$\dot{R} = -b(R_s + R)\dot{p}$$

$$\dot{R} = [a(cQ - R)H(q_1 - p) - b((1 - c)Q + R)H(p - q_1)]\dot{p}$$

Figure 3.4: Illustration of the isotropic softening model and the combined isotropic hardening-softening model.

3.4.4 Strain-memory-effect

It has been observed in multiple step cyclic loading tests for steels, that cyclic hardening/softening behaviour is influenced by the prior history of inelastic strain-range [43][49]. Nevertheless this history-depended behaviour cannot be simulated by above mentioned kinematic or isotropic hardening models. Therefore, to take into account the history effects of cyclic hardening behaviour, several new internal variables should be introduced, so that the prior maximum viscoplastic strain-range can be memorized. This is so-called strain-memory-effect. The concept of it is to use a strain-memory-surface in viscoplastic strain space, which is expressed by:

$$F = \frac{2}{3}J_2(\underline{\underline{\varepsilon}}_p - \underline{\underline{\xi}}) - q_s \leq 0,$$
(3.30)

with $J_2(\underline{\underline{\varepsilon}}_p - \underline{\underline{\xi}}) = \sqrt{\frac{3}{2}(\underline{\underline{\varepsilon}}_p' - \underline{\underline{\xi}}') : (\underline{\underline{\varepsilon}}_p' - \underline{\underline{\xi}}')}$,

where $\underline{\underline{\xi}}$ and q_s are two new internal variables, which define the centre and the radius of the strain-memory-surface, respectively. As shown in figure 3.5, while $\frac{2}{3}J_2(\underline{\underline{\varepsilon}}_p - \underline{\underline{\xi}})$ increases beyond the strain-memory-surface; the strain-memory-surface extends ac-

cordingly, so that the maximum inelastic strain is recorded by the variable q_s. The plastic flow inside the strain-memory-surface does not change the strain-memory-state.
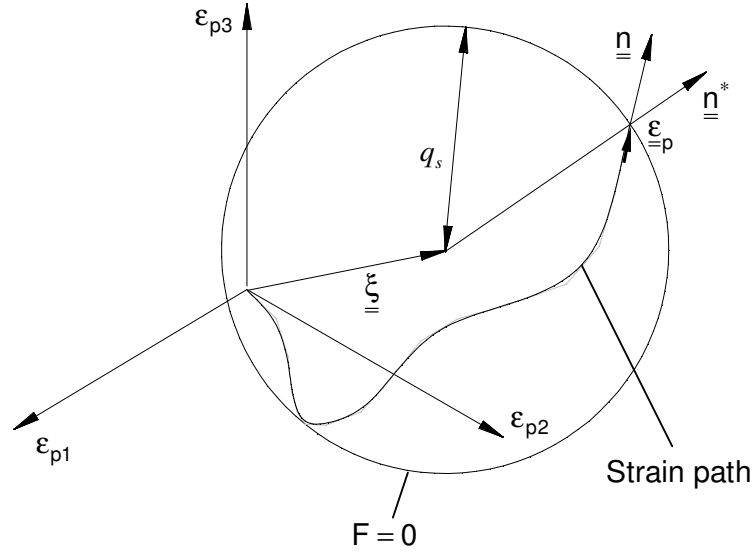

Figure 3.5: Schematic illustration of strain-memory-surface.

The following two evolution equations are applied to define internal variables $\underset{=}{\xi}$ and q_s:

$$\dot{q}_s = \eta H(F) < \underset{=}{n} : \underset{=}{n}^* > \dot{p},$$ (3.31)

$$\dot{\underset{=}{\xi}} = (1-\eta)\sqrt{\frac{3}{2}} H(F) < \underset{=}{n} : \underset{=}{n}^* > \underset{=}{n}^* \dot{p},$$ (3.32)

where coefficient η is introduced by Ohno to induce a progressive strain-memory. $\underset{=}{n}$ and $\underset{=}{n}^*$ are unit normals to the equipotential surface f and the strain-memory-surface F, respectively:

$$\underset{=}{n} = \sqrt{\frac{2}{3}} \frac{\dot{\underset{=}{\varepsilon}}_p}{\dot{q}_s} = \sqrt{\frac{3}{2}} \frac{\underset{=}{\sigma}' - \underset{=}{X}'}{J_2(\underset{=}{\sigma} - \underset{=}{X})},$$ (3.33)

$$\underset{=}{n}^* = \sqrt{\frac{2}{3}} \frac{\underset{=}{\varepsilon}_p - \underset{=}{\xi}}{q_s}.$$ (3.34)

Finally, the connection between isotropic hardening and strain-memory-effect is built up by the variable Q and the evolution equation of isotropic hardening. Since q_s corresponds to the maximum reached viscoplastic strain, Q can be empirically defined by the following equations:

$$\dot{Q} = 2\mu(Q_{max} - Q)\dot{q}_s, \tag{3.35}$$

$$\Rightarrow Q = Q_{max} + (Q_0 - Q_{max})e^{-2\mu q_s}; \quad Q_0 = Q(t=0). \tag{3.36}$$

in which μ is a material parameter, and Q_0 and Q_{max} are parameters, which denote the initial and maximum size of strain-memory-surface respectively.

3.5 Implementation of the viscoplastic Chaboche model in FEM program ABAQUS

The efficiency of numerical analysis for an inelastically loaded component depends mainly on two factors: On one hand, how far the material law can describe the macroscopic inelastic deformation behaviour of the material; on the other hand, whether this material law is available in a proper numerical method for structural analysis.

So far the viscoplastic material laws, such as the viscoplastic Chaboche model, are not yet available in commercial FEM programs. Nevertheless the commercial FEM program ABAQUS provides an interface, by which user-defined subroutines can be integrated. The user subroutine UMAT in ABAQUS [72] is such an approach, in which self-defined material laws can be integrated. In the frame of this work, the viscoplastic constitutive model was programmed and implemented in UMAT. For the integration of constitutive equations, the Explicit-Euler-Method with sub-increment associated with a time-step-controlling was applied.

Since the explicit integration method is only conditional stable, the global increment Δt specified in FE program is divided into sub-increments $\Delta\varepsilon$, and integration is executed in individual sub-increment [9]. Furthermore based on the recommendation in [73], applying elasticity instead of the tangent module (initial rigidity method) also lead to good results.
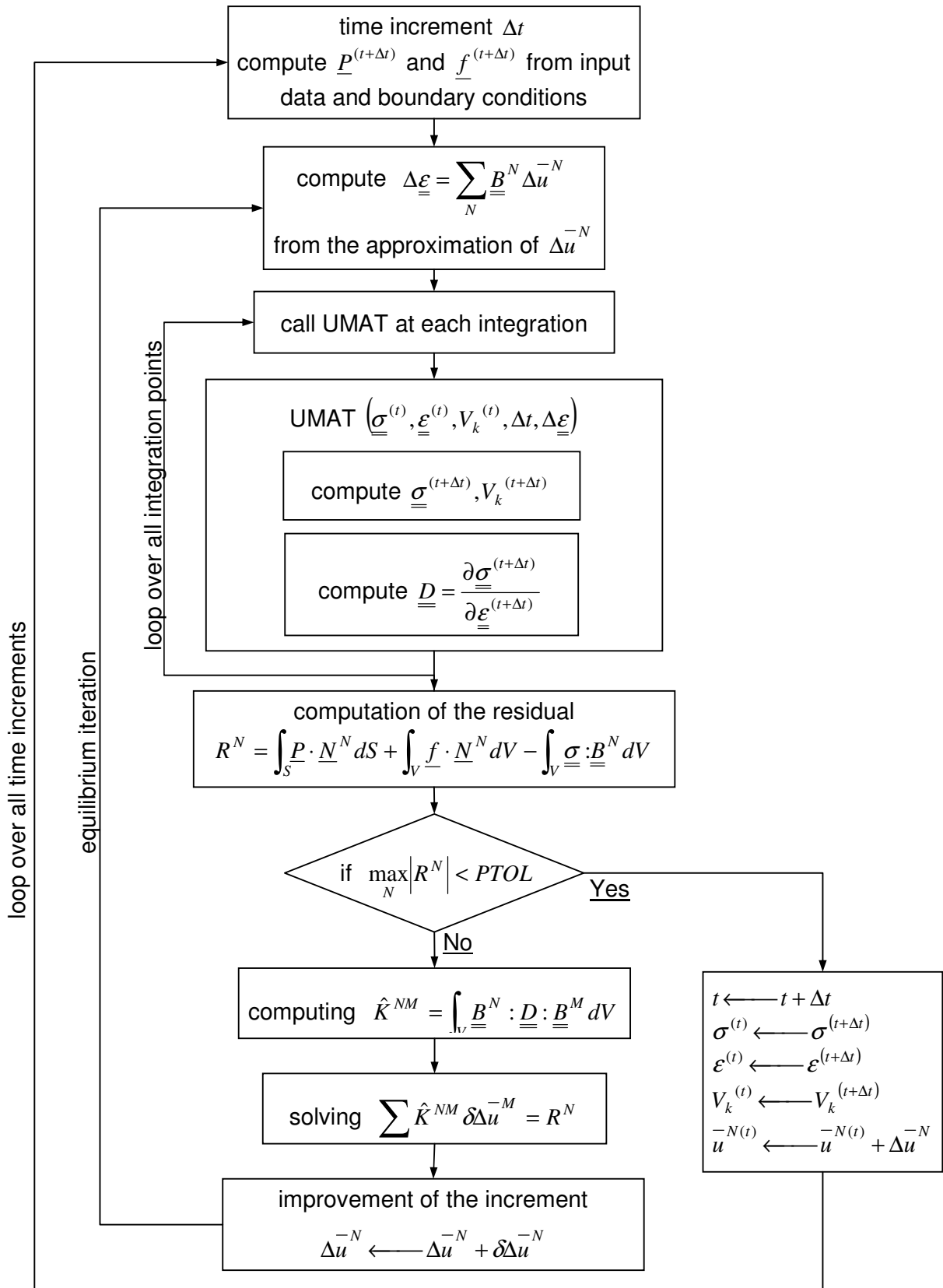
Figure 3.6: Flow chart of a nonlinear FE analysis in ABAQUS [9].

The procedure of the integration and the interaction between the user-defined subroutine UMAT and FEM program ABAQUS are illustrated in figure 3.6. It can be obviously recognized that the user-defined subroutine UMAT locates within three loops. It is accessed at each integration point of a FE model for each equilibrium iteration in each time increment. At each call the constitutive equations are integrated. Namely, based on values such as $\underline{\underline{\sigma}}^{(t)}$, $\underline{\underline{\varepsilon}}^{(t)}$, $V_k^{(t)}$ and $\Delta\underline{\underline{\varepsilon}}$ at time t, which are handed over by the main program of UMAT, the $\underline{\underline{\sigma}}^{(t+\Delta t)}$, $V_k^{(t+\Delta t)}$ and $\underline{\underline{D}}^{(t+\Delta t)}$ are calculated corresponding to time increment Δt. The total required computational time depends on the computation of the equilibrium conditions as well as the integration of the constitutive equations.

4 Experimental investigation with uniaxial tests

As test materials for the verification of the viscoplastic Chaboche model discussed in previous chapter, the austenitic material X6 CrNiNb 18-10 (material number 1.4550) and ferritic material 20 MnMoNi 5-5 (material number 1.6310) were selected, which are frequently applied as pipeline material in German boiling and pressurized water nuclear power plants. The austenitic material X6 CrNiNb 18-10, which contains 18% Cr, 10% Ni, is nonmagnetic and corrosion-resistant. The ferritic material 20 MnMoNi 5-5 is a fine grained quenched and tempered alloy steel. The microstructures of the test material are illustrated in figure 4.1 and 4.2.
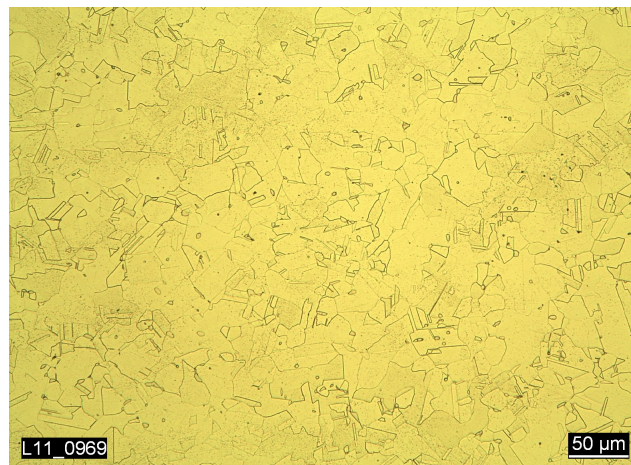
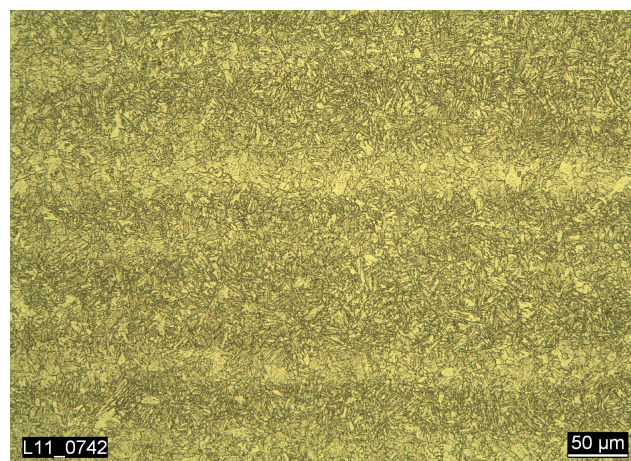Figure 4.1: Microstructure of austenitic material X6 CrNiNb 18-10 [89] .

Figure 4.2: Microstructure of ferritic material 20 MnMoNi 5-5 [89] .

The chemical compositions of both materials are shown in table 4.1 and 4.2 respectively.

C	Si	Mn	P	S	Cr	Ni	Mo	V
0.03	0.4	1.34	0.029	0.003	18.1	10.7	0.14	0.03
Al	Cu	W	Co	Nb	Sn	Ti	As	
0.03	0.07	0.02	0.06	0.32	<0.01	<0.01	<0.01	

Table 4.1: Chemical composition of austenitic material X6 CrNiNb 18-10.

C	Si	Mn	P	S	Cr	Mo	Ni	Al
0.21	0.20	1.41	0.006	0.001	0.10	0.496	0.69	0.012
Co	Cu	Ti	V	W	Pb	Sn	As	Zr
0.009	0.054	0.001	0.004	0.007	<0.001	0.005	0.006	<0.001
Ce	Sb	Te	Ta	B	Zn	N	Fe	
<0.002	<0.002	<0.001	<0.003	<0.003	<0.001	0.009	96.8	

Table 4.2: Chemical composition of ferritic material 20 MnMoNi 5-5.

The mechanical characteristic values of the austenitic material X6 CrNiNb 18-10 and the ferritic material 20 MnMoNi 5-5 are illustrated in table 4.3 and 4.4 respectively.

Temperature	$R_{p0.2}$	$R_{p1.0}$	R_m	A_3	Z	E
°C	MPa	MPa	MPa	%	%	MPa
RT	228	277	673	64.8	78.5	192500
RT	242	280	666	65.3	77.7	192500
230	185	226	471	48.9	80.0	167200
230	188	291	476	49.9	78.5	177500
300	182	209	438	45.1	80.0	180400
300	169	200	430	46.9	78.5	177100
400	141	189	422	46.6	76.2	173000
400	151	191	425	46.6	78.4	175000

Table 4.3: Mechanical characteristic values of austenitic material X6 CrNiNb 18-10.

Temperature	$R_{p0.2}$	$R_{p1.0}$	R_m	A_3	Z	E
°C	MPa	MPa	MPa	%	%	MPa
RT	500	541	746	32	63	210000
RT	466	510	702	32	63	210000
230	453	504	632	29	63	193000
230	462	509	643	30	64	193000
300	448	509	681	36	65	186400
300	463	524	706	35	64	186400
400	405	467	588	36	74.5	180000
400	396	462	588	35.5	74.1	174000

Table 4.4: Mechanical characteristic values of ferritic material 20 MnMoNi 5-5.

Experimental tests were implemented at room temperature (RT) and 300°C, respectively. The test temperature 300°C was applied corresponding to the service temperature of the German pressurized water reactor. Experiments by executing uniaxial monotonic tensile tests and uniaxial cyclic tension-compression tests, which are so-called low cycle fatigue (LCF) tests, with small specimens served for the characterization of typical material behaviour of the austenitic and ferritic materials. The small specimen is sketched in figure 4.3. For the austenitic material, the specimens were produced from forged round bars with 80mm in diameter. Whereas for the ferritic material, the specimens were manufactured from rolled plates with approximately 680mm in length, 600mm in width and 24mm in thickness.
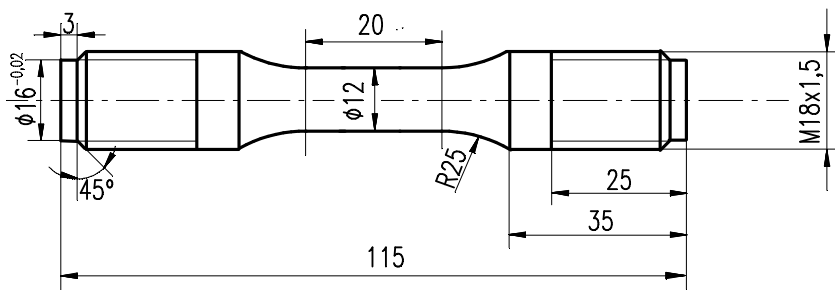

Figure 4.3: Illustration of the small specimen for uniaxial tests.

The results of the uniaxial tests are presented in following chapters 4.1 and 4.2.

As conventions, the stress and strain values shown in all figures in this chapter and chapter 5.6 are engineering stress and strain; and the strain-rate $\dot{\varepsilon} = 5 \times 10^{-4} / s$ was applied as standard strain-rate in most uniaxial tests. This convention will not be re-marked again in individual figures. If strain-rate is different from the standard strain-rate, e.g. $\dot{\varepsilon} = 5 \times 10^{-3} / s$ or $\dot{\varepsilon} = 5 \times 10^{-5} / s$ was applied, they are remarked in corresponding results figures.

4.1 Uniaxial tests for the austenitic steel X6 CrNiNb 18-10

To investigate the uniaxial tensile behaviour of the selected austenitic material, the monotonic tensile tests were performed. The engineering yield curves of the austenitic material at room temperature and 300°C are illustrated in figure 4.4. Both curves show stress values during the increase of strain from 0 to 6%. Strong nonlinear strain-hardening can be detected in both yield curves. The yield curve at RT proceeds smoothly at the yielding stage and no obvious bending point can be observed. The deflections from linear elasticity can be detected within a stress-range of 130 MPa - 170 MPa, and the characteristic value $R_{p0.2}$ around 228 MPa to 242 MPa was measured. The change of temperature influences the yield point and hardening behaviour of the austenitic material, so that the yield curve at 300°C locates beneath the one at room temperature. The characteristic value $R_{p0.2}$ locates between 169 MPa and 172 at 300°C.
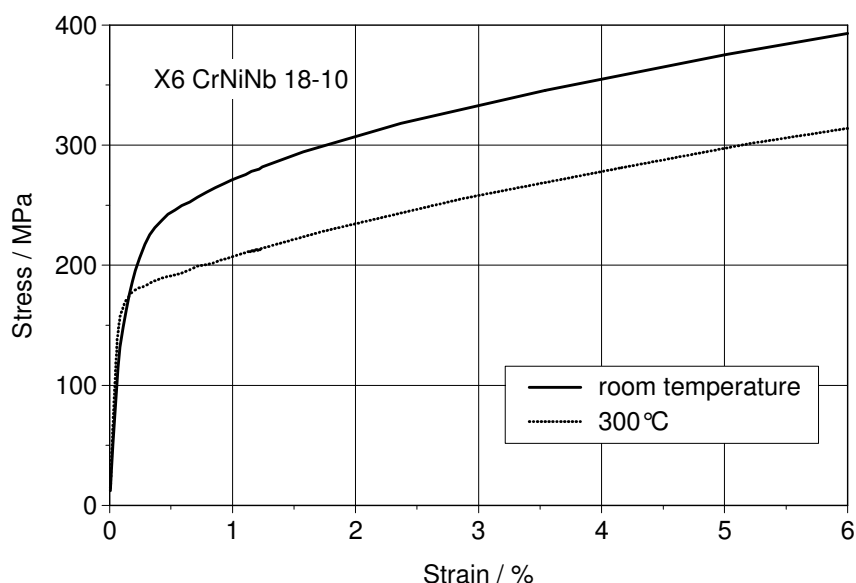

Figure 4.4: Yield curves of the austenitic material at room temperature and 300°C.

If cyclic loading yields inelastic deformation in metallic materials, there exists a phase difference between cyclic stress and cyclic strain. The characteristic curve representing the relationship between cyclic stress and strain is so-called hysteresis loop. Moreover, typical characteristic cyclic behaviour of steels shows the cyclic hardening/softening. For instance, if under strain-controlled cyclic loading, in which strain-range is constantly kept in loading cycles, the corresponding stress-range increases during the increase of loading cycles, this behaviour is so-called cyclic hardening. Likewise, the contrary behaviour is named as cyclic softening. To characterize the material behaviour under cyclic loading, uniaxial strain-controlled cyclic tension-compression tests were performed by using different strain-rates. As already mentioned in this chapter, the standard strain-rate was specified to be $\dot{\varepsilon} = 5 \times 10^{-4} / s$ in this work, which was applied in tensile tests and most of uniaxial cyclic tests. To study the time effect of the selected materials, uniaxial cyclic tests by using strain-rates $\dot{\varepsilon} = 5 \times 10^{-3} / s$ and $\dot{\varepsilon} = 5 \times 10^{-5} / s$ were implemented too.
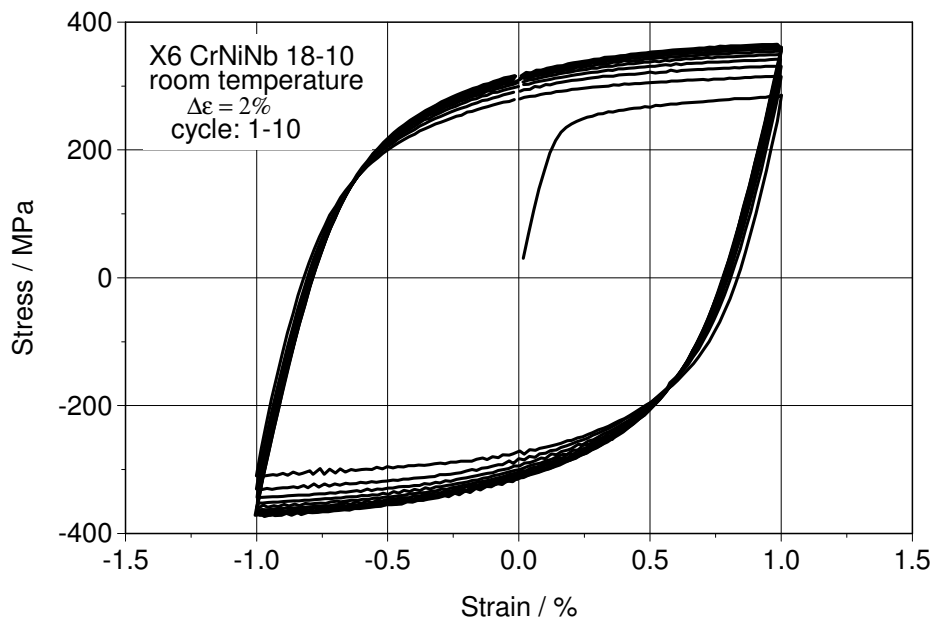

Figure 4.5: Hysteresis loops of the austenitic material at room temperature.

Figure 4.5 depicts the hysteresis loops corresponding to the first 10 cycles for the austenitic material at room temperature, in which strain-range and strain-rate were specified to be $\Delta\varepsilon = 2.0\%$ and $\dot{\varepsilon} = 5 \times 10^{-4} / s$, respectively. In successive loading cycles, the hysteresis loops show similar shapes. Nevertheless they show gradually increased

cyclic hardening. That is, during the increase of loading cycles, corresponding stress-range increases.
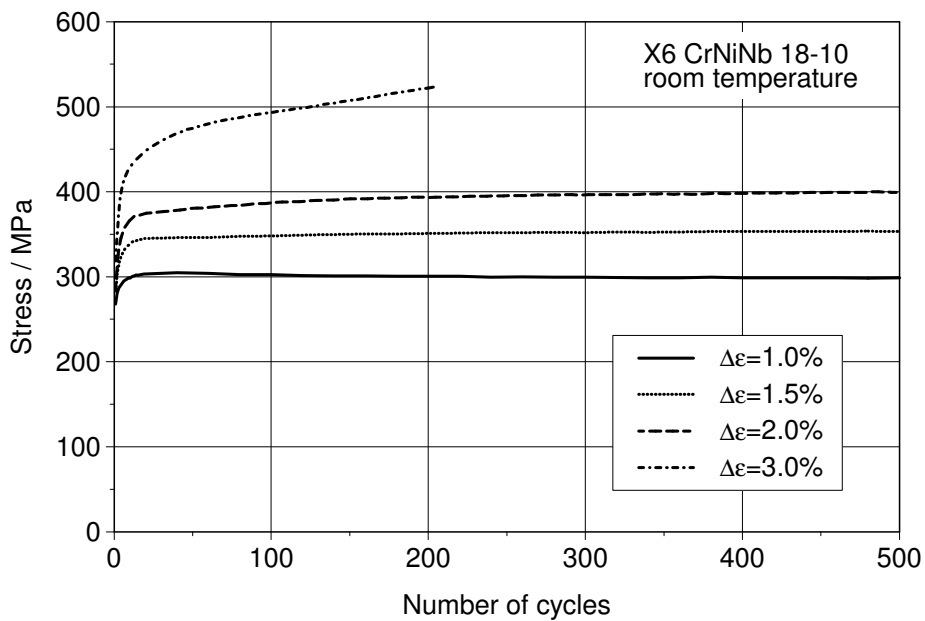

Figure 4.6: Stress-amplitude against number of cycles in different strain-ranges for the austenitic material at room temperature.

Figure 4.6 illustrates the test results based on four uniaxial strain-controlled cyclic tests, which were implemented by using the standard strain-rate 5×10^{-4} /s and different strain-ranges, 1.0%, 1.5%, 2.0% and 3.0%, respectively. The cyclic hardening/softening curves, which depict stress-amplitudes with respect to the number of loading cycles, are illustrated in the figure. The common feature of these curves is that they all show significant incipient cyclic hardening at the beginning of loading cycles. After the start-up stage, the curves with different strain-ranges show different cyclic hardening/softening behaviour: The smallest strain-range 1.0% leads to minor cyclic softening after the first 20 cycles; Strain-range 1.5% induces a neutral behaviour after incipient significant cyclic hardening. Namely, after the start-up stage, the amplitude of stress reaches a saturation and keeps constant in the following cycles; strain-range 2.0 yields a cyclic hardening until a saturation is reached after above 400 cycles; The cyclic hardening curve with strain-range of 3.0% proceeds with an continuous linear increase after the incipient cyclic hardening till a failure occurred after around 200 cycles. Furthermore, based on this test, it can be observed that the magnitude of incipi-

ent cyclic hardening is also dependent on strain-range: That is, a larger strain-range evokes larger incipient cyclic hardening.

Figure 4.7 shows the uniaxial ratchetting test for the austenitic material at room temperature. Uniaxial stress controlled cyclic tension-compression loading was applied in the test. The test was performed in three steps sequentially. Each step contains 300 load cycles. The applied stress range 500 MPa was constantly kept in all three steps, while the axial mean-stress σ_m was stepwise increased. In the first step the mean-stress was zero, so that the test was fully reversed performed; in the second step the mean-stress 20 MPa was applied; in the third step the mean-stress was increased to 40 MPa. The applied strain rate was equivalent to the standard strain rate $5 \times 10^{-4} / s$.
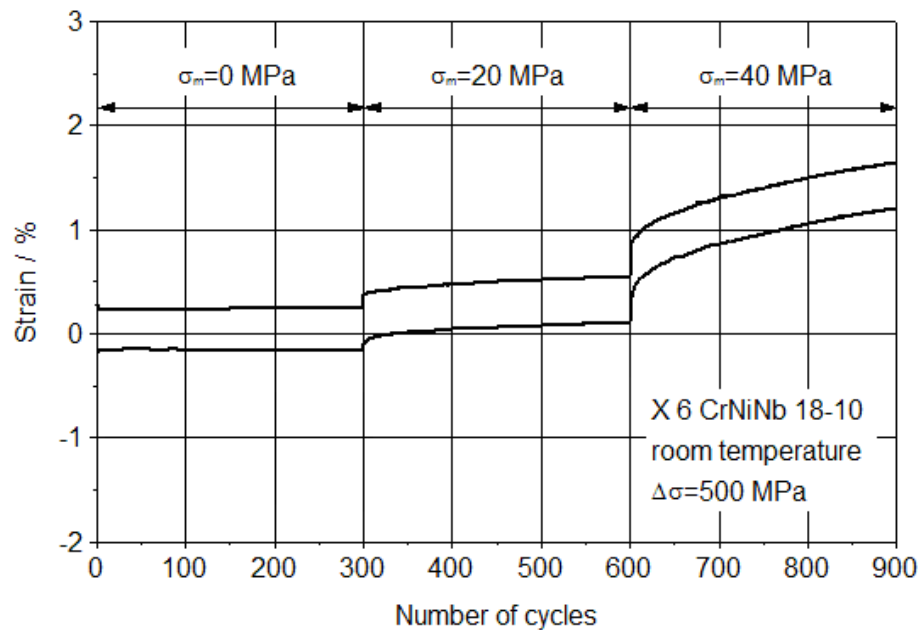
Figure 4.7: Uniaxial ratchetting test for the austenitic material at room temperature.

The curves in the figure 4.7 present the maximum and minimum strains with respect to load cycles. In the first step, since there was no mean-stress applied, the curves proceed without any deflection. After 300 cycles the second step began, due to the involvement of mean-stress, the curves started to deflect to the tension direction, in which the mean-stress was applied. The deflection of the maximal and minimal strain curves presented the accumulation of uniaxial ratchetting. Therefore they are so-called uniaxial ratchetting curves. In the third step, due to the increase of mean-stress, the deflection was much larger than that in the second step. In both steps, where uniaxial

ratchetting arises, the ratchetting strains increased very fast at the beginning. As intro-duced in chapter 2.7, this phenomenon is so-called transient ratchetting. After a cer-tain number of cycles, the speed of ratchetting slowed down. This phenomenon was so-called asymptotic ratchetting. In the second step, asymptotic ratchetting tended to reach a saturation after 300 cycles, which is so-called shake-down, whereas in the third step, due to the large mean-stress, asymptotic ratchetting kept increasing linearly after 300 cycles, which is so-called continuous ratchetting. As shown in the figure, the magnitude of transient ratchetting and the gradient of asymptotic ratchetting are both influenced by the applied mean-stress, which is so-called primary stress regarding the topic of uniaxial ratchetting.

The experimental results of uniaxial cyclic tests for the austenitic material at 300 °C are illustrated in figures 4.8 and 4.9. Figure 4.8 illustrates a uniaxial strain-controlled cyclic test, which was performed by using strain-range 2.0% and the standard strain-rate. Several hysteresis loops regarding cycle 1, 2, 10, 50 and 200 are sketched in the fig-ure. Cyclic hardening can also be detected from the increase of the stress-range dur-ing the increase of loading cycles.
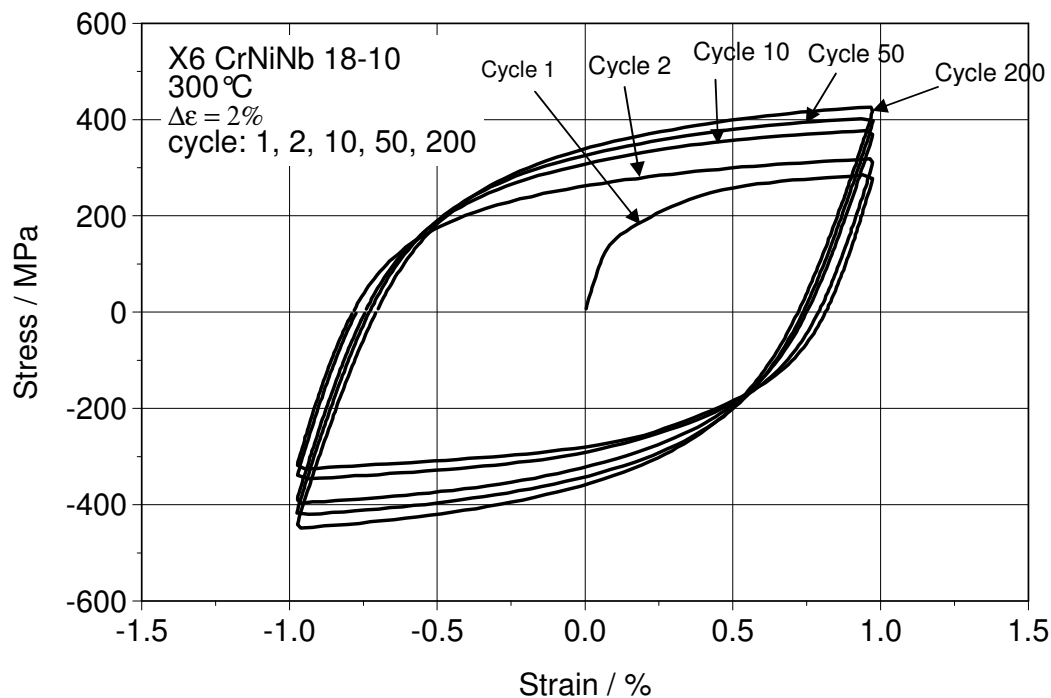

Figure 4.8: Hysteresis loops of the austenitic material at 300 °C.

Cyclic hardening/softening curves regarding different strain-ranges are illustrated in figure 4.9. Corresponding uniaxial cyclic tests were performed by using the standard strain-rate and strain-ranges 1.0%, 1.5% and 2.0%, respectively. It is found that, compared to those at room temperature, the cyclic curves at 300 °C show more significant dependence on strain-range: Strain-range 1.0% yields cyclic softening in succession of the incipient cyclic hardening; The curve corresponding strain-range 1.5% presents similar cyclic behaviour as that at room temperature, where a saturation is reached after the first 20 cycles; The cyclic hardening curve regarding strain-range 2.0% presents continuous cyclic hardening with a linear increase after incipient cyclic hardening in first 20 cycles.
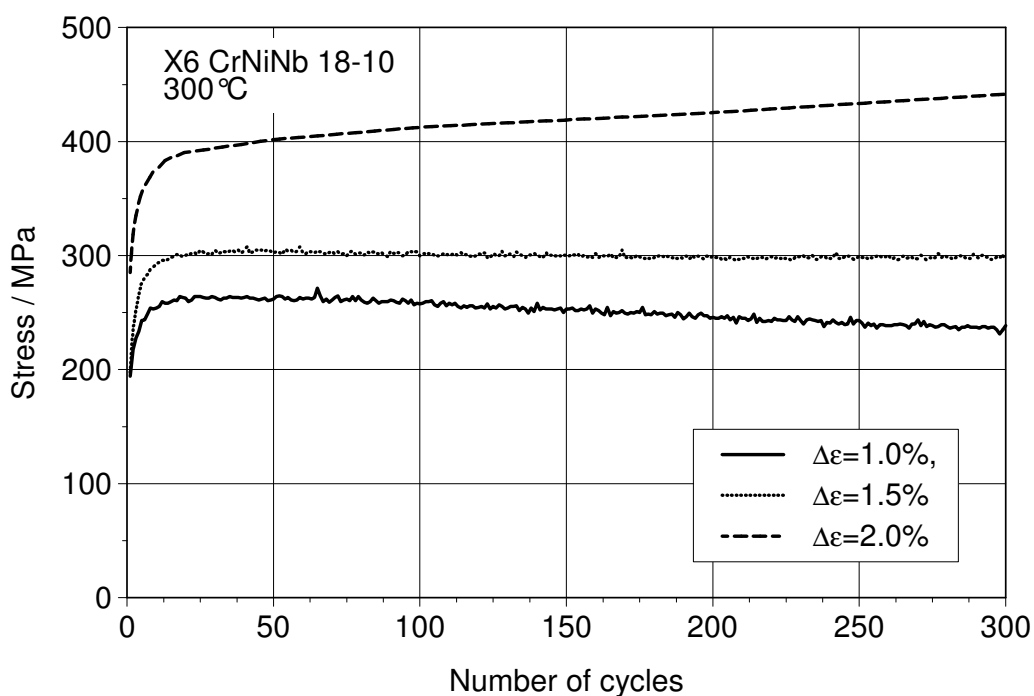

Figure 4.9: Stress-amplitude against number of cycles in different strain-ranges for the austenitic material at 300 °C.

The uniaxial ratchetting test for the austenitic material at 300 °C is shown in figure 4.10. Uniaxial stress controlled cyclic tension-compression loading was applied in the test. The test was performed also in three steps sequentially. Each step contains 500 load cycles. The applied stress range 340 MPa was constantly kept in all three steps, while the axial mean-stress σ_m was stepwise increased. In the first step the mean-stress

was zero; in the second step the mean-stress 20 MPa was applied; in the third step the mean-stress was increased to 40 MPa. The applied strain rate was equivalent to the standard strain rate 5×10^{-4} /s.
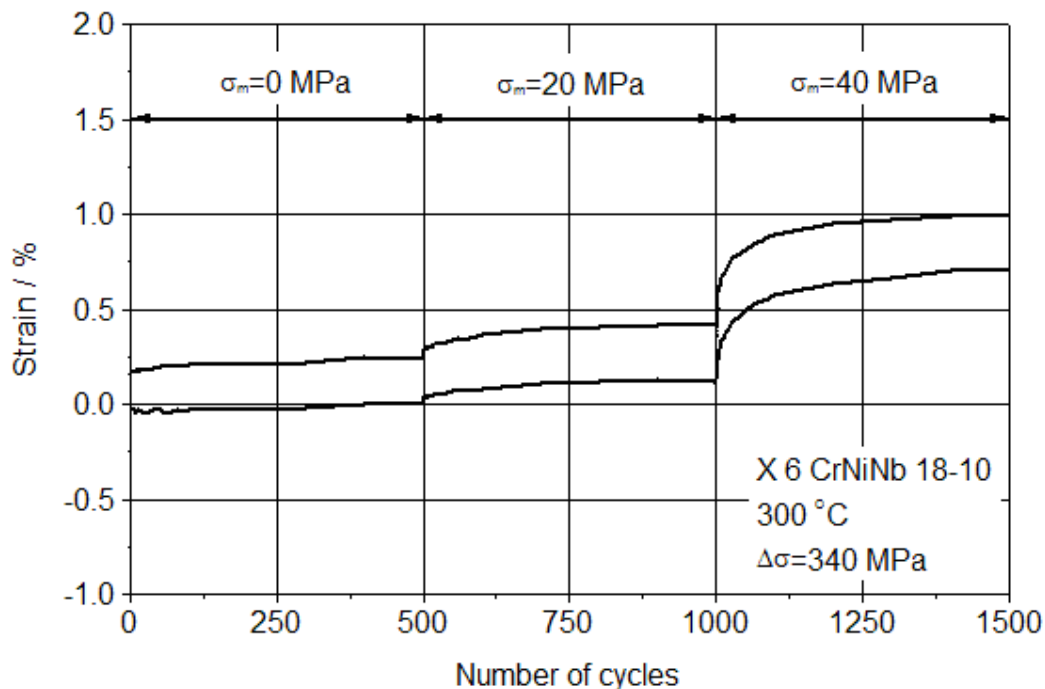

Figure 4.10: Uniaxial ratchetting test for the austenitic material at 300 °C.

The maximum and minimum strains with respect to load cycles are illustrated in figure 4.10. In the first step, the curves proceeded almost constantly. After 500 cycles, mean-stress 20 MPa was applied, so that the uniaxial ratchetting could be clearly observed. That is, transient ratchetting was followed by asymptotic ratchetting with a shake-down. In the third step, due to the increase of mean-stress, larger transient ratchetting was evoked. Furthermore due to the larger mean-stress in the third step, the gradient of asymptotic ratchetting was also larger than that in the second step.

4.2 Uniaxial tests for the ferritic steel 20 MnMoNi 5-5

The uniaxial tensile test was also performed for the ferritic material 20 MnMoNi 5-5. Engineering yield curves at room temperature and 300 °C are illustrated in figure 4.11, where the relationship between stress and strain from 0 to 6% is presented. Compared to the austenitic material X6 CrNiNb 18-10, the ferritic material 20 MnMoNi 5-5 pos-sesses larger elastic moduli at room temperature and 300 °C. Nonlinearity of strain

hardening at both temperatures can be observed. Nevertheless differing from the austenitic material, the ferritic material shows clear bends at yielding stage, especially at room temperature. Additionally, temperature difference doesn't influence the yield limits so much like in the austenitic materials, so that the deflection between both yield curves is not as large as that of the austenitic material.
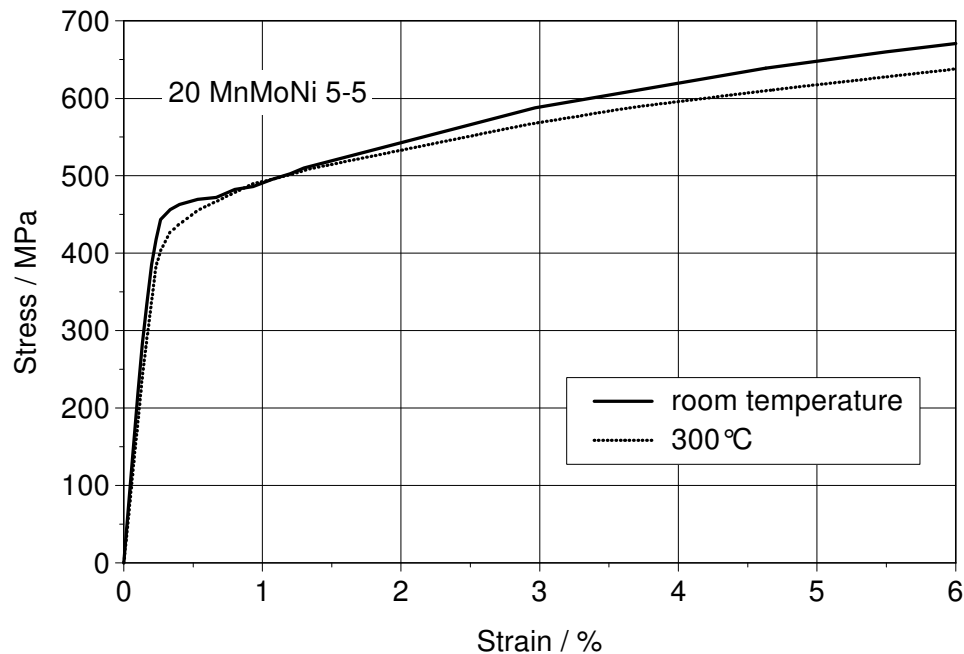

Figure 4.11: Yield curves of the ferritic material at room temperature and 300°C.

The hysteresis loops of the ferritic material at room temperature and 300°C are illustrated in figures 4.12 and 4.13, respectively. At each temperature, a uniaxial strain-controlled cyclic test was performed with strain-range 2.0% and the standard strain-rate.

As shown in figure 4.12, after initial hardening in the first cycle, hysteresis loops present similar shapes in cycle 20 and cycle 250. The cyclic behaviour shows in the beginning cyclic hardening and successively cyclic softening, which can be indicated by the expansion and diminishing of stress-range. The hysteresis loops regarding cycle 1, 20 and 300 at 300°C are sketched in figure 4.13. The strain-hardening in different hysteresis loops present similar shape. From cycle 1 to cycle 20, cyclic hardening can be observed, while from cycle 20 to cycle 300, slight cyclic softening can be detected.
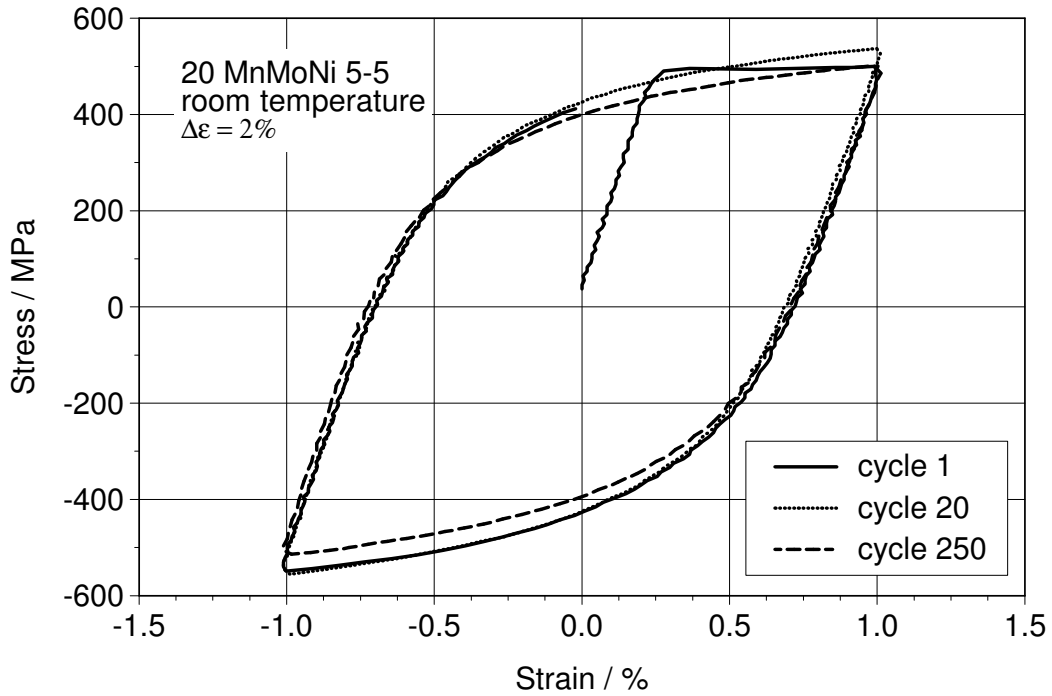
Figure 4.12: Hysteresis loops of the ferritic material at room temperature.
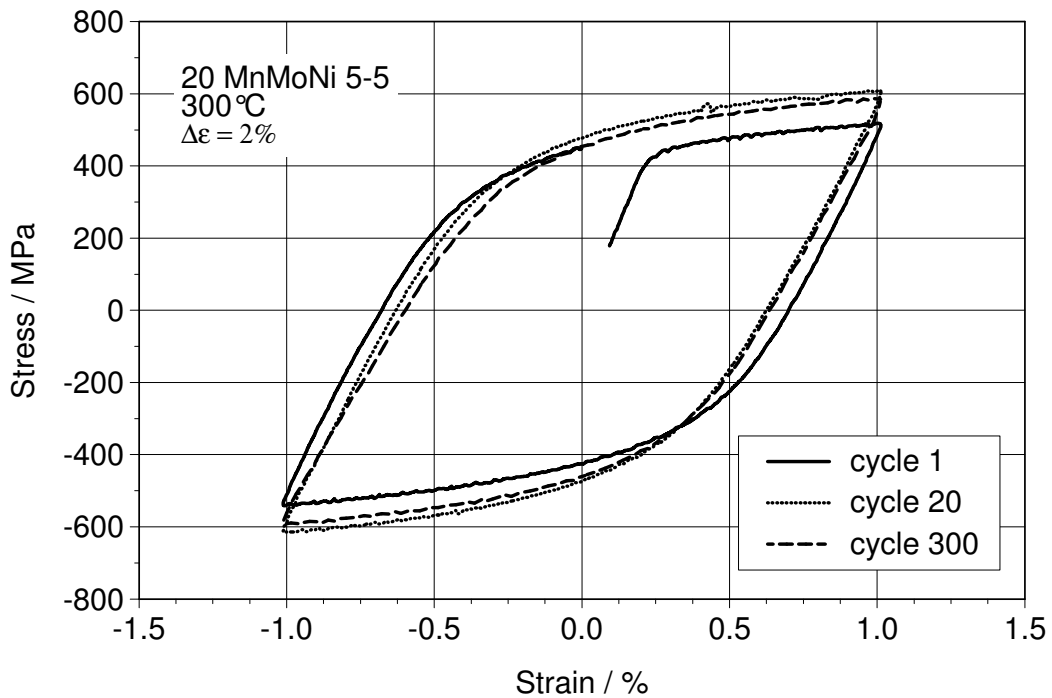

Figure 4.13: Hysteresis loops of the ferritic material at 300 °C.

To investigate the cyclic behaviour of the ferritic material, a series of uniaxial cyclic tests with different strain-ranges were carried out at room temperature and 300 °C, re-

spectively. The corresponding cyclic hardening/softening curves are shown in figures 4.14 and 4.15.

Figure 4.14 illustrates the testing results of three uniaxial strain-controlled cyclic tests, which were performed with strain-rates $\Delta\varepsilon = 1.0\%$, $\Delta\varepsilon = 2.0\%$ and $\Delta\varepsilon = 4.0\%$ and the standard strain-rate at room temperature. The stress-amplitudes are plotted with respect to the number of cycles. All three cyclic curves show combined hardening-softening behaviour: That is, incipient cyclic hardening in the beginning and cyclic softening in succession. Furthermore, the larger strain-ranges evoke larger magnitudes of cyclic hardening and cyclic softening.
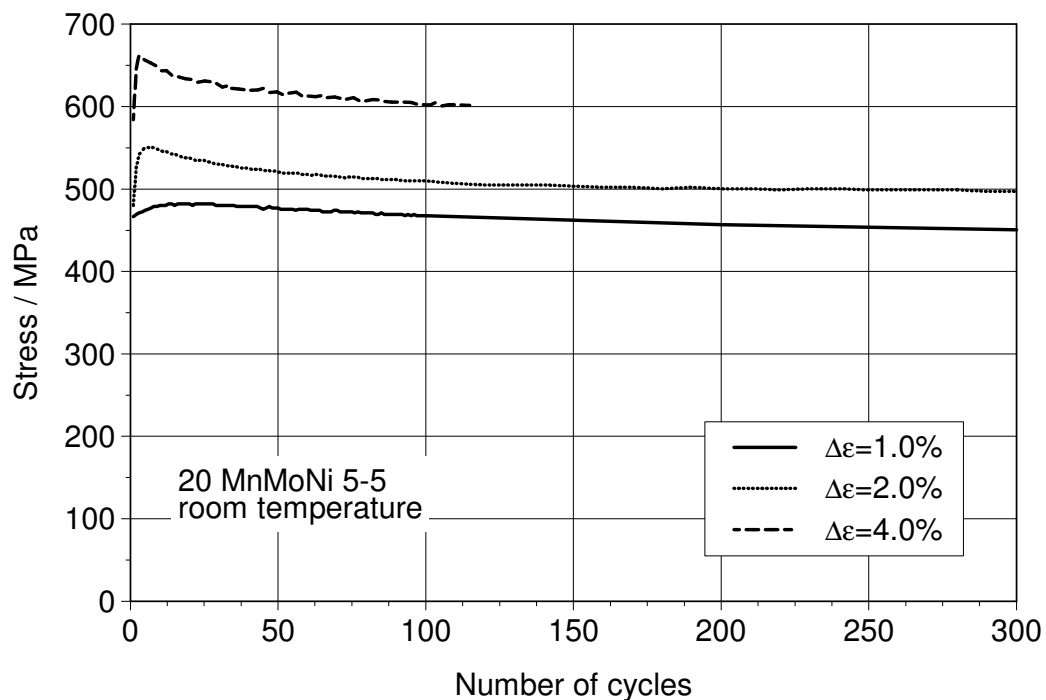

Figure 4.14: Stress-amplitude against number of cycles in different strain-ranges for the ferritic material at room temperature.

Figure 4.15 depicts experimental results of three uniaxial strain-controlled cyclic tests, which were tested at $300\,^{\circ}\mathrm{C}$. The strain-ranges were specified to $\Delta\varepsilon = 1.0\%$, $\Delta\varepsilon = 2.0\%$ and $\Delta\varepsilon = 3.0\%$, respectively, and the standard strain-rate $\dot{\varepsilon} = 5\times10^{-4}\,/\mathrm{s}$ was applied. By comparing with results in figure 4.14, it is found that the higher temperature tends to reduce the cyclic softening behaviour: In small strain-range $\Delta\varepsilon = 1.0\%$, only cyclic hardening and successive saturation are presented. In larger

strain-ranges $\Delta\varepsilon = 2.0\%$ and $\Delta\varepsilon = 3.0\%$, only slight softening appear after the incipient cyclic hardening stage.
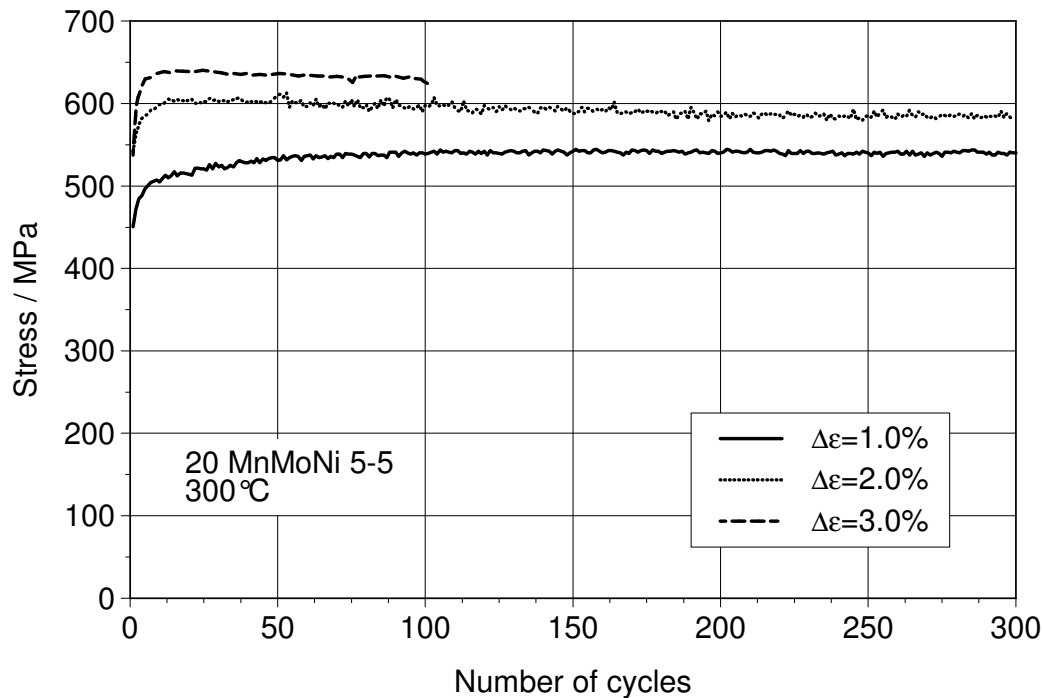

Figure 4.15: Stress-amplitude against number of cycles in different strain-ranges for the ferritic material at 300°C.

The uniaxial ratchetting test for the ferritic material at room temperature is shown in figure 4.16. Uniaxial stress controlled cyclic tension-compression loading was applied in the test. The test was performed in two steps sequentially. The first step contains 200 cycles, while in the second step, the incipient crack was detected on the specimen after 75 cycles. The applied stress range 920 MPa was constantly kept in both steps, In the first step, the specimen was fully reversed loaded, while in the second step, a mean-stress 100 MPa was applied. The applied strain rate was equivalent to the standard strain rate $5 \times 10^{-4} /s$. The maximum and minimum strains with respect to load cycles are shown in the figure. In the first step, the curves proceeded constantly due to the fully reversed loading. After 200 cycles, uniaxial ratchetting was invoked and rapidly increased. It can been seen in the figure, due to the large mean-stress, not only significant transient ratchetting can be observed in the beginning of the second step, but also the asymptotic ratchetting presents a large gradient, so that specimen cracked after only 75 cycles in the second step.
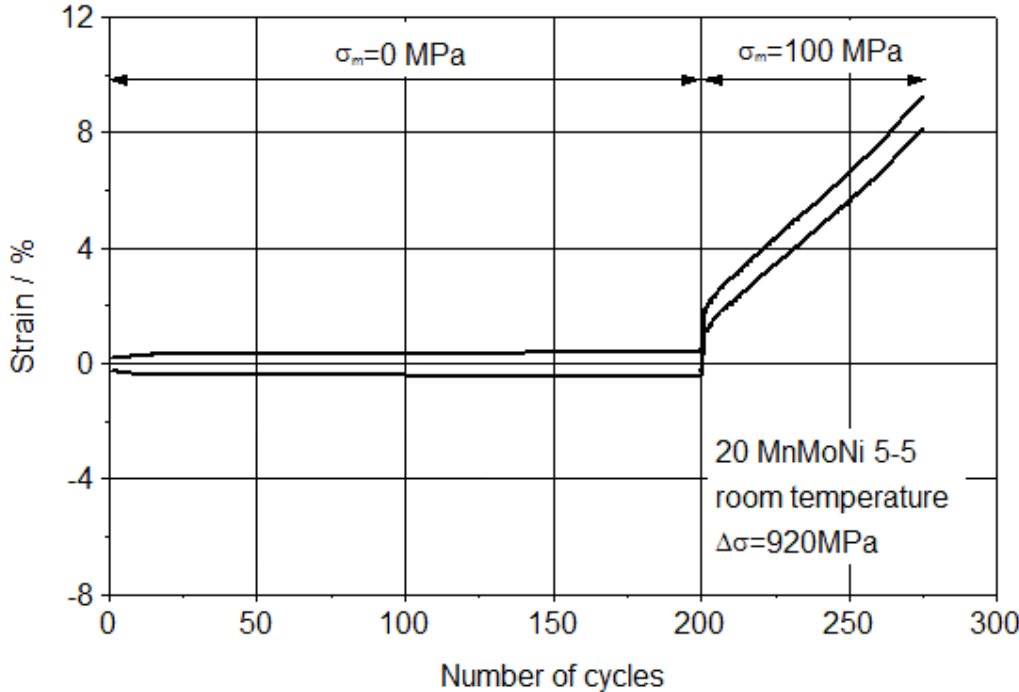
Figure 4.16: Uniaxial ratchetting test for the ferritic material at room temperature.

5 Parameter identification

As discussed in chapter 4, the viscoplastic Chaboche model contains a series of material parameters. For the application of the material model in finite element analysis (FEA), the parameters must be identified in advance. In this work, the identification of the material parameters (parameter-fitting) was realized by comparing uniaxial testing results with calculation results by using an effective optimization program, which not only implements the computation of the material model, but also optimizes the parameters. Since more than twenty parameters are to be determined for the viscoplastic Chaboche model and most of them do not represent material characteristic values in real sense, the procedure of parameter-fitting is very complex.

5.1 General introduction of optimization method

In general, parameter-fitting can be accomplished in two ways. One is so-called simultaneous parameter-fitting, while the other is so-called successive parameter-fitting. By using successive parameter-fitting, the parameters are determined stepwise and calculated by using their particularly sensitive experiments. For instance, the kinematic hardening variables can be extracted from uniaxial cyclic tension-compression tests. Literature [74] introduces a so-called Trial-and-Error method for the successive parameter-fitting. By using this method, the parameters are manually varied until a preferably better consistency with experimental results is achieved.

In simultaneous parameter-fitting, the following three tasks should be accomplished:

- Calculation of model prediction,
- Calculation of quality-rank for the consistency with experiments,
- Optimization of the quality-rank.

The material models are usually formulated as nonlinear differential equation systems, which cannot be solved analytically. However they are always solvable by using numerical integration for corresponding load type.

If the model prediction is computed in dependence of the parameters, the consistency between the computations and experiments should be check. Thereby the selected comparison-values, e.g. stress and strain, should be compared with experimental measurements. The comparison can be realized either by graphic visualization or by defining and computing a so-called quality-rank. The selection of the comparison-values strongly depends on the experimental data, the type of the material models as well as the applied optimization algorithm. Finally, the quality-rank of the consistency is to be improved iteratively until a predefined consistency quality is reached.

Beside above mentioned two methods, there are other optimization methods introduced in literatures [75][76]. Especially in [77][78], two novel optimization methods are introduced based on Darwin principles mutation and simulations of hierarchical neuron networks, respectively.

5.2 Choosing adequate optimization method

The identification of parameters requires adequate optimization methods, which provide estimations for the searched parameters, so that the test results can be described as exactly as possible. The optimization methods should possess the following characteristics [79][80]:

1. Consistency

When the number of the measuring points N trends to infinite, the estimation $\widehat{\theta}_N$ of the searched parameter θ trends to the true value θ_0.

2. Unbiasedness

The optimization method is unbiased, if $E(\widehat{\underline{\theta}}_N) - \underline{\theta}_0 = E(\widehat{\underline{\theta}}_N - \underline{\theta}_0) = 0$ for any N. E denotes an operator for the expected value.

3. Efficiency

The smaller the error of estimation is, the larger the probability will be, that the estimation locates close to the true parameter value θ_0 (asymptotic limit).

4. Robustness

An optimization method is identified as a robust method, if the estimation of the parameters is insensitive with regard to the small deflection concerning both the database and the model.

5. Minimum costs

The optimization method should be simple to program and require short computing time. Considering the economical reasons, this point is often fulfilled in complex problems.

In general an optimization method should be formulated in such a way, which is as fast, safe and economical as possible. As well known estimation methods, Moment-Method, Maximum-Likelihood-Method, and Least-Error-Square-Method are widely applied. All of these methods are consistent. The obtained estimations $\hat{\theta}_N$ are normal distributed and unbiased at the asymptotic limit around the true value θ_0. If linear models are used for the description of the measured results, the obtained estimations are unbiased regarding any N. For linear model, the Least-Error-Square-Method has the smallest variance (Gauß-Markov-Theorem). For nonlinear models the Maximum-Likelihood-Method is more efficient than the Moment-Method and the Least-Error-Square-Method. Particularly it has the highest efficiency at the asymptotic limit. The detailed discussion is included in [81].

In summary, the Least-Error-Square-Method is preferable for linear models, and the Maximum-Likelihood Method is suitable to nonlinear models. If the measured values are normal-distributed around their estimated value, both methods are equivalent [82].

The assumption of the normal-distribution of measured values Y_i around their estimated value with a standard deflection w_i is implicitly described in the following. The scalar residue function gives:

$$Q^2 = \sum_{i=1}^{N}\sum_{j=1}^{N}[Y_i - f(x_i,\underline{\theta})] \; V_{ij}^{-1}[Y_j - f(x_j,\underline{\theta})], \tag{5.1}$$

in which Y_i are measured values, f is the response of the model with regard to the parameter set $\underline{\theta}$ and the independent values x_i. V_{ij} denotes the covariance matrix. To obtain optimal parameter set, the residue function should be minimum. Based on the precondition that all Y_i are independent, V_{ij} is assumed as a diagonal matrix, consequently equation (5.1) can be simplified to:

$$Q^2 = \sum_{i=1}^{N} \left[\frac{Y_i - f(x_i, \underline{\theta})}{w_i} \right]^2,$$

(5.2)

which provides a starting point for simultaneous parameter identifications.

5.3 Applied optimization method

For the parameter identification of the Viscoplastic Chaboche model the CERN-software package MINUIT [83] was applied. Two minimization methods in MINUIT are mainly applied, which are simplex method and gradient method.

5.3.1 Simplex method

Simplex method from Nelder and Mead [84] is one of the most successful stepping methods in dealing with multiple variables. A simplex is a generalization of the notion of a triangle or tetrahedron to arbitrary dimension. Specifically, an n-simplex is an n-dimensional polytope which is the convex hull of its n+1 vertices. It is a triangle in two dimensions, a tetrahedron in three, etc [85].

To illustrate how the method works, a two-dimensional case is visualized in figure 5.1 [83]. P_1, P_2 and P_3 are three initial simplex points, which are chosen randomly. $F(P_1)$, $F(P_2)$ and $F(P_3)$ are the function values at these simplex points, respectively. It is supposed that $P_1 = P_{min}$ corresponds to the point, which has the lowest function value, and $P_3 = P_{max}$ corresponds to the point, which has the highest function value. P^* is the mass centre of all points except P_{max}, which is calculated by:

$$P^* = \frac{1}{n} \left(\sum_{i=1}^{n+1} P_i - P_{max} \right).$$

(5.3)

The first simplex step is performed by replacing P_{max} by a point which has better function value. For this object, the first attempt is executed by reflecting P_{max} with respect

to P*, so that a new point can be obtained: P'=P*+(P*- P_{max}). If F(P')<F(P_{min}), a new attempt should be start and a new point is produced at P''=P*+2(P*- P_{max}). If F(P')>F(P_{max}), a new point is produced at P'''=P*-1/2(P*- P_{max}). The new point together with points P_1 and P_2 are used for the next step of simplex. If there is no point better than P_{max}, a complete new simplex should be restarted around P_{min}, with dimensions reduced by a factor of 0.5.
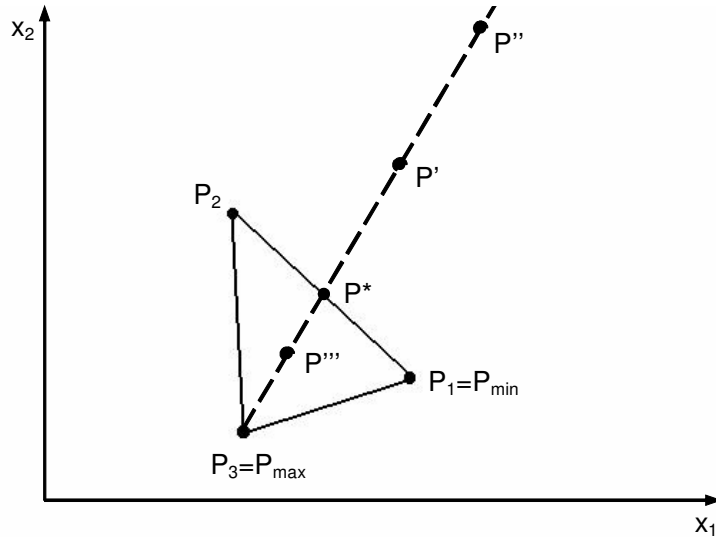

Figure 5.1: Illustration of Simplex method in a two-dimensional case.

5.3.2 Gradient method

The gradient method is based on a modified Newton-Method. Supposing a quadratic function:

$$Q^2 = Q^2(\underline{\theta}_0) + \underline{g}^T(\underline{\theta} - \underline{\theta}_0) + \frac{1}{2}(\underline{\theta} - \underline{\theta}_0)^T \underline{\underline{G}}(\underline{\theta} - \underline{\theta}_0),$$ (5.4)

in which $\underline{g}$ denotes gradient,

$$\underline{g} = \nabla Q^2 = \left(\frac{\partial Q^2}{\partial \theta_i}\right)\Bigg|_{\underline{\theta}=\underline{\theta}_0},$$ (5.5)

and $\underline{\underline{G}}$ is the second derivative matrix:

$$\underline{\underline{G}} = \left(\frac{\partial^2 Q^2}{\partial \theta_i \partial \theta_j} \right)\Bigg|_{\underline{\theta}=\underline{\theta}_0} . \tag{5.6}$$

Since the function is quadratic, $\underline{\underline{G}}$ is constant. $\underline{\theta}_0$ represents initial parameter set.

The extremum of the function is determined by:

$$\frac{\partial Q^2}{\partial \underline{\theta}} = \underline{g} + (\underline{\theta} - \underline{\theta}_0)\underline{\underline{G}} = \underline{0} . \tag{5.7}$$

Supposing $\underline{\underline{G}}$ is positive defined (sufficient condition of the minimum), the minimum of the function is derived from equation (5.7):

$$\underline{\theta}_{\min} = \underline{\theta}_0 - \underline{\underline{V}}\,\underline{g} = \underline{\theta}_0 - \underline{\underline{V}}\nabla Q^2, \quad with \ \ \underline{\underline{V}} = \underline{\underline{G}}^{-1} . \tag{5.8}$$

Since quadratic functions only exist in seldom cases, this gradient method must be generalized. MINUIT also applies another method, which belongs to a so-called Variable-Metric-Method [86] and performs in the following steps [54]:

The gradient $\underline{g}_0$ should be calculated at the initial parameter set $\underline{\theta}_0$. In addition, tensors $\underline{\underline{V}}_0$ and $\underline{\underline{G}}_0$ should be estimated from $\underline{\underline{V}}$ and $\underline{\underline{G}}$. As initial value, the unit matrix or the diagonal covariant matrix, which is formed from the parameter scattering, can be used for $\underline{\underline{V}}_0$.

By using equation (5.8), the improved parameter set $\underline{\theta}_1$ is calculated. It is known from step 1, that $\underline{\theta}_1$ is not calculated with the exact covariant matrix, therefore in the new calculation, $\underline{\underline{V}}_0$ should be iteratively improved by multiplying a scalar factor α, until function $Q^2\big(\underline{\theta}_0 - \alpha\underline{\underline{V}}_0\underline{g}_0\big)$ reaches minimum. Additionally, the gradient $\underline{g}_1$ should be calculated at $\underline{\theta}_1$.

The matrix $\underline{\underline{V}}$ is iteratively improved by

$$\underline{\underline{V}}_1 = \underline{\underline{V}}_0 + f(\underline{\underline{V}}_0, \underline{\theta}_0, \underline{\theta}_1, \underline{g}_0, \underline{g}_1) . \tag{5.9}$$

Subsequently, $\underline{g}_0$, $\underline{\theta}_0$ and $\underline{\underline{V}}_0$ are replaced by $\underline{g}_1$, $\underline{\theta}_1$ and $\underline{\underline{V}}_1$, respectively. Step 2 and step 3 are repeated as often as possible until a predefined convergence criterion is fulfilled. f is defined by different functions in literatures, which are based on the characteristics of different models.

5.4 Implementation of the viscoplastic Chaboche model in MINUIT

To identify the material parameters using the optimization program package MINUIT, a subroutine is required, where the import of test data, the computation of numerical model, as well as the output of calculation results can be implemented. An original subroutine in MINUIT should be extended by user to fulfill above requirements. The uniaxial constitutive equations of the viscoplastic Chaboche model should be defined and numerically integrated in it. This subroutine should be very generally constructed, so that tensile tests, uniaxial strain-controlled cyclic tests (not only for single step tests but also for multiple step tests), uniaxial stress-controlled cyclic tests with mean-stress, as well as if necessary creep tests can be adopted for parameter-fitting.

The flowchart of the optimization procedure is illustrated in figure 5.2. First of all, required test data and the starting values of parameter set should be prepared for the optimization program. For automatizing this procedure, an external program was written and applied to search required test data, which include strain, stress and corresponding time at certain sampling points, and export the found test data as well as the starting values of the parameter set in a standard format into a so-called MINUIT input file. The MINUIT input file can be directly accessed by the main optimization program in MINUIT.

The experiments were executed either displacement-controlled or load-controlled. The measured values are engineering stresses and engineering strains. Nevertheless for parameter-fitting in MINUIT, the true stress and strain were applied to perform numerical integrations of the constitutive model. Therefore before the optimization procedure starts, the test data are converted to true stresses and true strains, so that the calculated values can be directly compared to the test data in the optimization program. After the optimization procedure completed, the stress and strain values are converted back to engineering stress and engineering strain just like the results presented by the

figures in this chapter. Based on the incompressible material hypothesis, the measured engineering stress and engineering strain can be converted by using following formulas to corresponding true values:

$$\varepsilon_{true} = \ln\left(1 + \varepsilon_{eng.}\right), \tag{5.10}$$

$$\sigma_{true} = \sigma_{eng.}\left(1 + \varepsilon_{eng.}\right) = \sigma_{eng.}\, e^{\varepsilon_{true}} \, . \tag{5.11}$$
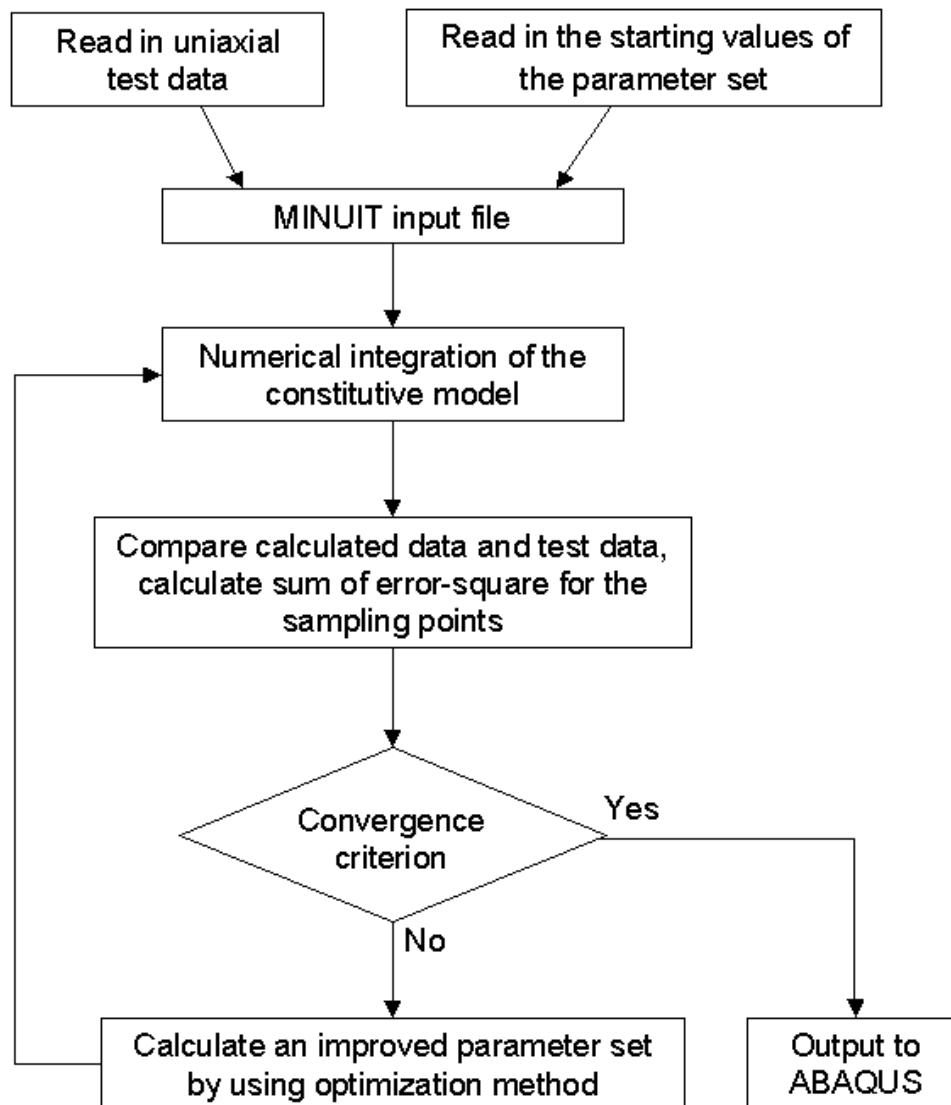
Figure 5.2: Flowchart of the parameter identification process.

In numerical integrations, the stresses and strains are calculated at each discrete time point corresponding to input data. The error-squares between calculated stresses and

measured stresses (in displacement-controlled tests) or between calculated strains and measured strains (in load-controlled tests) are summed up for all sampling points. For the calculation of the summation of error-square, a series of weighting factors can be defined and applied for each test. The weighting factors are selected in such a way, that each individual test contributes approximately the same portion in calculating the sum of error-square, so that each individual test has the same influence in identifying the parameter set.

If the sum of error-square fulfils a predefined convergence criterion, the optimization procedure is terminated and the parameter set is output for the FEA of components. Otherwise the calculated summation of error-square is submitted to the main program of MINUIT, which improves the parameter set by using previously described optimization methods. Subsequently, the updated parameter set is returned back to start an integration procedure of constitutive model as shown in figure 5.2. This procedure is repeated until the convergence criterion is fulfilled and an optimized parameter set is obtained, or the predefined maximum number of function-calls is reached.

5.5 Selection of the experimental data for parameter identification

The selection of experimental data strongly depends on the selected material model and the effects simulated by the numerical model. For instance, concerning a visco-plastic material model to describe creep behaviour, the strain-controlled cyclic tests, creep and tensile tests with different strain-rates should be applied, so that the parameters which present creep effects and time-dependent material behaviour can be reliably determined.

Regarding the austenitic material X6 CrNiNb 18-10and the ferritic material 20 MnMoNi 5-5, both of them present little difference of hardening behaviour with different strain-rates at room temperature. Nevertheless both materials show evident time-dependent behaviour at 300°C. Therefore in parameter-fitting, the strain-range and strain-rate of the selected uniaxial tests should be consistent to the corresponding equivalent values in component tests.

For the description of strain-hardening, cyclic hardening/softening and ratchetting behaviour of the selected materials, the following tests should be performed for parameter-fitting at room temperature and 300°C:

- Monotonic tensile tests.
- Uniaxial strain-controlled cyclic tests.
- Uniaxial stress-controlled multiple step cyclic tests with mean-stresses.

In tensile test, the material behaviour was rendered under monotonic increased loading. The monotonic tensile behaviour is the basis of numerical computation for the material model, in which the strain hardening behaviour of material is represented. By using strain-controlled cyclic test, the cyclic material behaviour can be determined. For instance the cyclic yield curve can be determined by such tests. During this kind of test, the specimen was cyclically loaded between the two predefined strain limits until the stress-amplitude reaches saturated state. If the stress-amplitude doesn't show saturation during cyclic loading, the cyclic curves should be adopted until the increase or decrease of stress-amplitude reaches a constant tangent. To determine uniaxial ratchetting behaviour, uniaxial stress-controlled cyclic tests with increasing mean-stresses were performed. The stress-range was specified larger than twice of the yield limit, $\Delta\sigma > 2k$, so that the plastic flow occurs not only under tension but also under compression. The mean-stresses were increased stepwise, so that the influence of mean-stress on ratchetting deformation could be studied.

5.6 Comparison between experiments and model predictions

5.6.1 Comparison for the austenitic material at room temperature

The fitted parameters by using uniaxial tests and MINUIT program for the austenitic material at room temperature are listed in table 5.1. These parameters correspond to the viscoplastic Chaboche model incorporating Ohno-Wang approach II (equation 3.18) for kinematic hardening, cyclic softening approach (equation 3.29) for isotropic hardening variable, and strain-memory-effect.

E	ν	Z	n	k	m_i	c_1	γ_1
192500	0.3	100.0	10.0	135	8	35581.8	833.3

c_2	γ_2	c_3	γ_3	c_4	γ_4	a	b
8300.2	270.3	1753.3	114.9	1300.0	15.8	50.0	1.9

c	q_1	η	μ	Q_{max}	Q_0		
3.7	0.304	0.2	400	10.1	0.1		

Table 5.1: Fitted parameters of the viscoplastic Chaboche model including Ohno-Wang approach II for the austenitic material at room temperature.
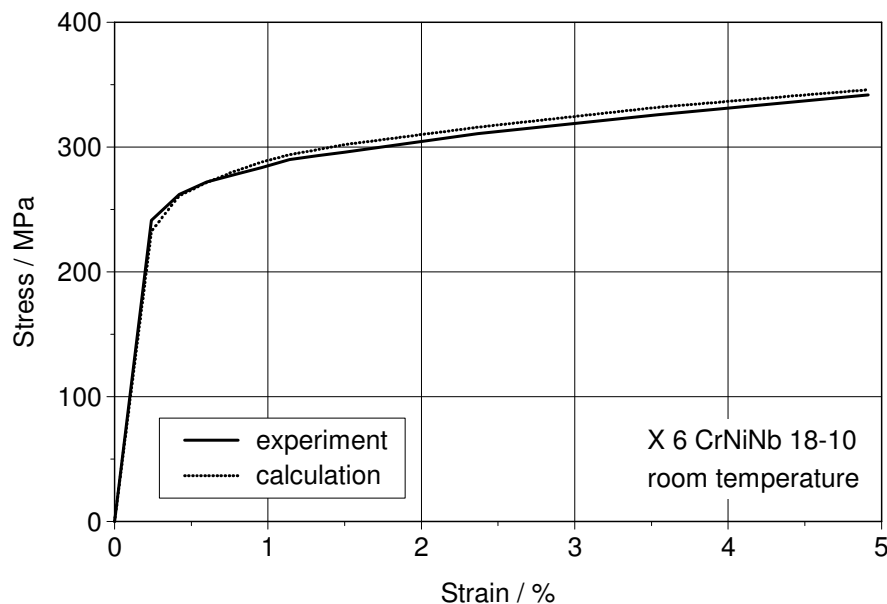

Figure 5.3: Comparison of measured and calculated uniaxial tensile curves for the austenitic material at room temperature.

In the following, the comparisons between the experiments and numerical calculations by using above mentioned viscoplastic Chaboche model will be presented. Figure 5.3 shows the comparison between calculated and experimental uniaxial tensile curves of the austenitic material at room temperature. Since there are four back-stresses applied in the kinematic hardening model, very good agreement is obtained between the experimental measurements and model prediction in a wide load range till 5.0% of strain.
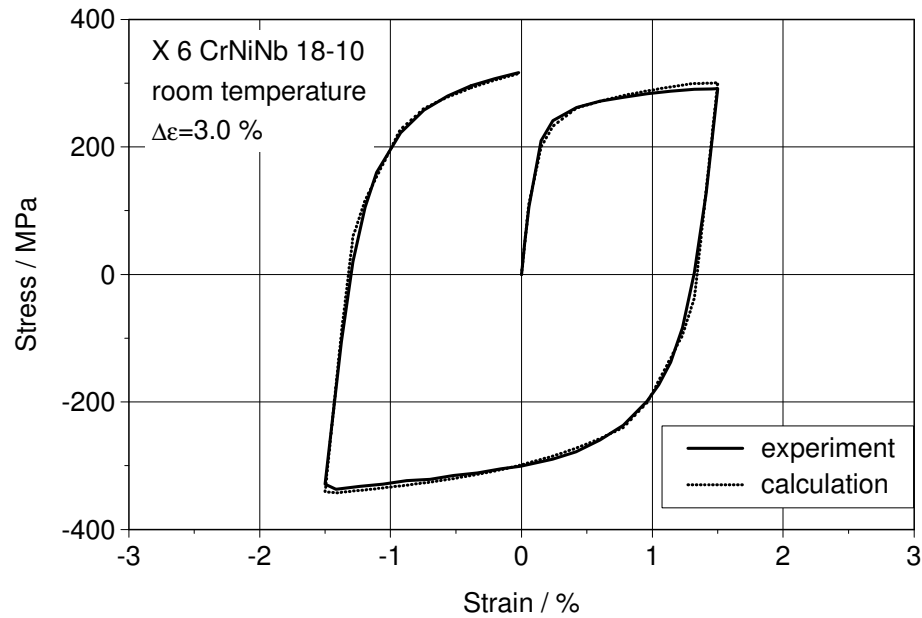

Figure 5.4: Comparison of measured and calculated hysteresis loops of the first load cycle in uniaxial cyclic test for the austenitic material at room temperature.

Figure 5.4 illustrates a uniaxial strain-controlled cyclic tension-compression test for the austenitic material at room temperature. The strain-range was 3.0% and the standard strain-rate 5×10^{-4} /s was applied, respectively. The hysteresis loop of the first load cycle from test and calculation are demonstrated in the figure. The stress and strain values represented in the figure are axial stress and axial strain. Very good consistency was achieved, so that both curves almost completely overlap. As discussed in chapter 2, for the austenitic material at room temperature, hysteresis loops has nearly the same shape during the cyclic loading, and the expansion or shrink of the of stress-range depends only on cyclic hardening/softening behaviour, which is simulated by the isotropic hardening model. Therefore, for the parameter-fitting of kinematic hardening model, it is sufficient to follow the hysteresis loop of one cycle.
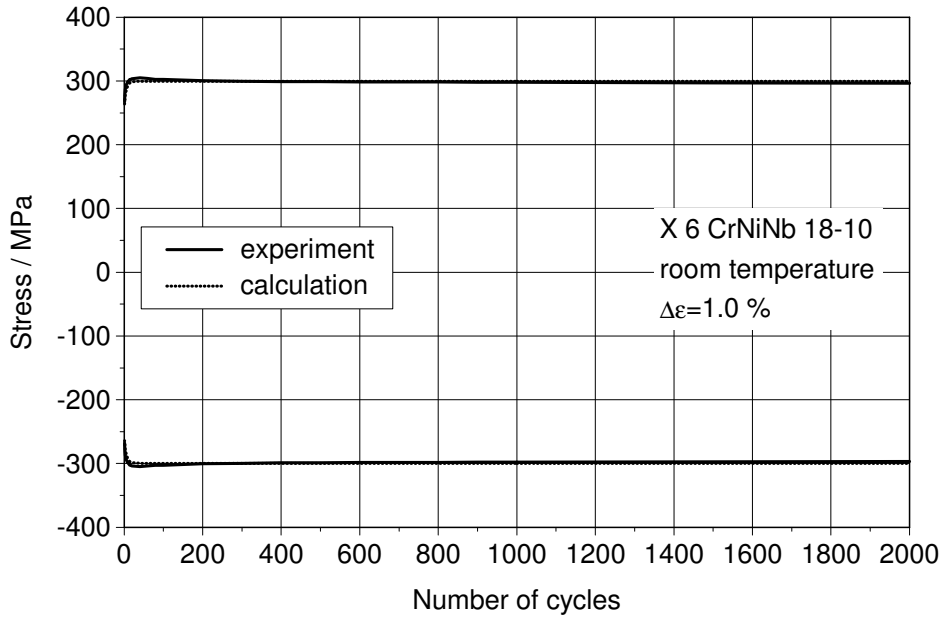
Figure 5.5: Comparison of the stress-ranges between experiment and calculation of uniaxial strain-controlled cyclic tension-compression test for the austenitic material at room temperature.
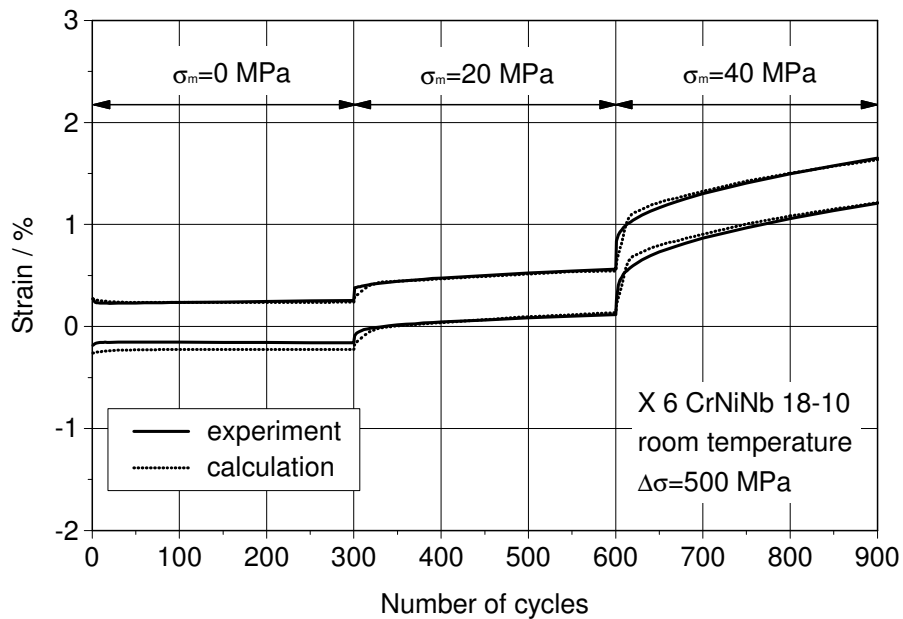

Figure 5.6: Comparison of the uniaxial ratchetting between experiment and calculation for the austenitic material at room temperature.

Figure 5.5 illustrates the curves of stress-range during a uniaxial strain-controlled cyclic tension-compression test performed with strain-range 1.0% and standard strain-

rate $5{\times}10^{-4}$ /s, by which the cyclic hardening/softening behaviour can be represented. The maximum and minimum stresses with respect to the number of cycles are plotted in the figure. It can be observed that both experimental and calculated curves show incipient cyclic hardening and subsequent neutral behaviour. The agreement between both curves is perfect, so that an overlap can be detected during the whole procedure.

Figure 5.6 shows the experimental and calculated results based on a so-called uniaxial ratchetting test. The test was performed by applying uniaxial stress-controlled cyclic loading and stepwise increased mean-stress. The test contained three steps. The stress-range was kept to be 500 MPa during the test, while the mean-stress was increased step by step: It was specified to zero in the first step, and 20 MPa and 40 MPa in the second and third steps, respectively. The accumulated strain (uniaxial ratchetting strain) induced by the mean-stress is illustrated against the number of cycles in the figure. In the first step, the zero mean-stress yields no uniaxial ratchetting. In the second and third steps, noticeable ratchetting strain is evoked due to the nonzero mean-stress. Very good consistency was achieved between the experiment and calculation. The slight deviation in the first step and the transient ratchetting in the second and third step are a compromise for getting a general good agreement with all selected test. As mentioned in chapter 5.4, a series weighting factors were applied during the procedure of parameter optimization, so that each selected test for parameter fitting contributes approximately the same portion to the optimization. In this way, the over all best fitting results for all selected tests were obtained. It was very often found that if the weighting factors were adjusted preferentially for one test, the agreements with the other tests became worse. Therefore a compromise should be made, so that the fitted parameters present acceptable fitting results for all selected tests. The more tests are selected, the more difficult it is to find parameters, which present good agreements for all the selected tests simultaneously. In this work more than 20 parameters were determined for strain-hardening, cyclic hardening/softening and ratchetting behaviour at the same time. Thereby it was very difficult to find a parameter set, which perfectly fits all the tests.

5.6.2 Comparison for the austenitic material at 300°C

The fitted parameters for the austenitic material at room temperature are listed in table 5.2. The parameters correspond to the viscoplastic Chaboche model containing Ohno-Wang approach II (equation 3.18) for kinematic hardening, cyclic softening approach (equation 3.29) for isotropic hardening variable, and strain-memory-effect.

E	ν	Z	n	k	m_i	c_1	γ_1
179000	0.3	80.0	10.0	80	8	71824.0	1200.0

c_2	γ_2	c_3	γ_3	c_4	γ_4	a	b
3100.0	387.0	144.0	36.0	2500.0	25.8	6.83	0.264

c	q_1	η	μ	Q_{max}	Q_0		
2.0	0.312	0.056	529.4	35.0	0.1		

Table 5.2: Fitted parameters of the viscoplastic Chaboche model including Ohno-Wang approach II for the austenitic material at 300°C.

A series of uniaxial tests were selected to fit the parameters for the austenitic material at 300°C. The same as above discussion for the austenitic material at room temperature, the fitted results can be verified by using the following figures.
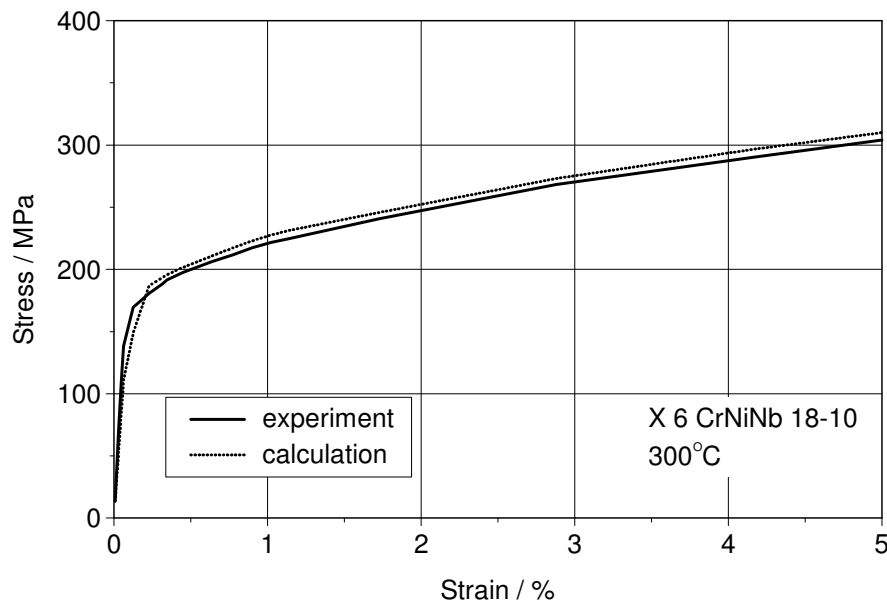

Figure 5.7: Comparison of measured and calculated uniaxial tensile curves for the austenitic material at 300°C.

Figure 5.7 shows the comparison between the calculated and measured yield curves based on a uniaxial tensile test, which was performed within strain-range 5.0%. Figure 5.8 presents the experimental and calculated hysteresis loops of the first load cycle regarding a uniaxial strain-controlled cyclic tension-compression test with strain-range 1.0%. In both tests, the standard strain-rate 5×10^{-4}/s was applied. The stress and strain values represented in the figure are axial stress and axial strain. Very good agreements are achieved between the experimental measurements and model simulation. It should be mentioned here that, since the austenitic material doesn't show explicit yield point especially at 300℃, it is difficult to find the suitable parameters to very accurately simulate the strong nonlinear hardening at the yielding stage. It is the reason, why small deflections can be detected between the strain amplitudes of 0.1% and 0.2% in both figures.
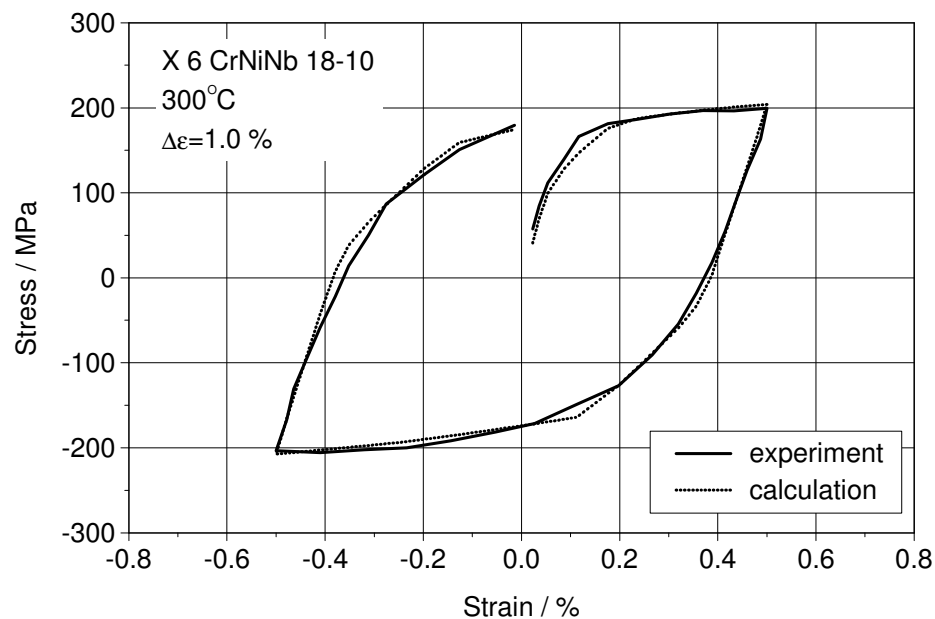

Figure 5.8: Comparison of measured and calculated hysteresis loops of the first load cycle in uniaxial cyclic test for the austenitic material at 300℃.

Figure 5.9 shows experimental and calculated stress-ranges regarding the same uniaxial strain controlled cyclic tension-compression test of figure 5.8. The curves of maximum and minimum stresses during the cyclic loading represent the cyclic hardening/softening behaviour. The experimental curve shows an explicit combined hardening-softening behaviour. By using the fitted parameters, this cyclic behaviour can be perfectly predicted.
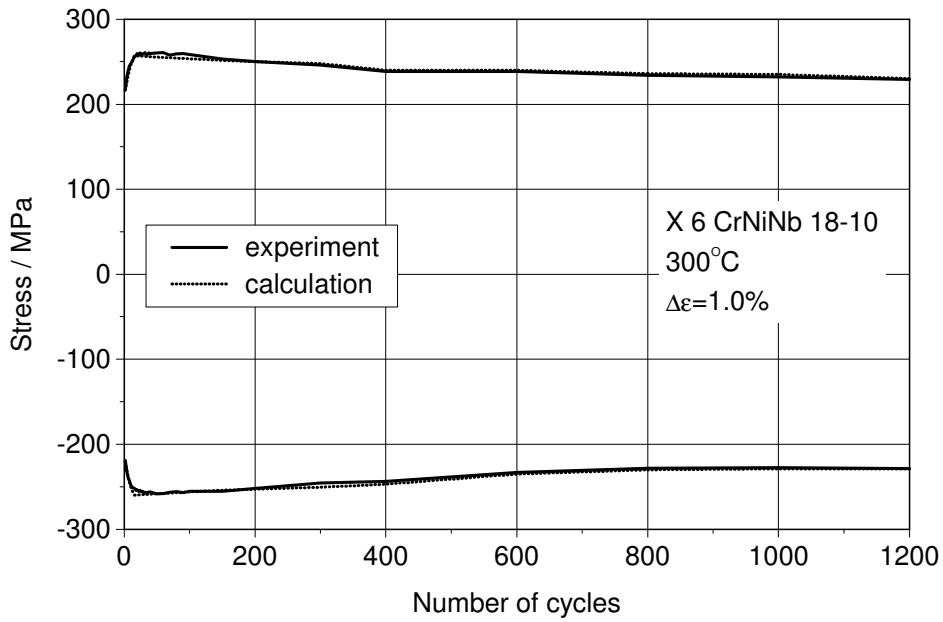
Figure 5.9: Comparison of the stress-ranges between experiment and calculation regarding uniaxial strain-controlled cyclic tension-compression test for the austenitic material at 300 °C.
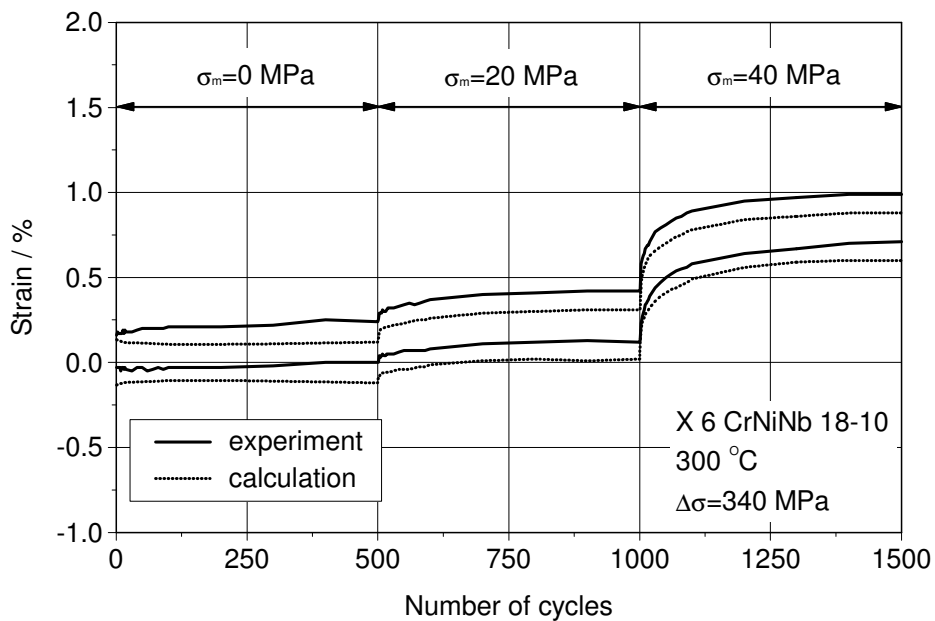

Figure 5.10: Comparison of the uniaxial ratchetting between experiment and calculation for the austenitic material at 300 °C.

Figure 5.10 illustrates experimental and calculated uniaxial ratchetting curves regarding a uniaxial stress-controlled cyclic tension-compression test with stepwise in-

creased mean-stress. The stress-range specified in the test was 340 MPa, and it was constantly maintained in the test. The mean-stress was specified to 0, 20, and 40 MPa in three steps sequentially. The strain curves shown in the figure depict the axial strain –ranges during the uniaxial cyclic loading. It can be observed that, although the tendencies, shapes and magnitudes of both curves are quite similar, there exists a noticeable deflection between measurement and calculation. The reason is also attributed to the compromise, which was made to fit the strong nonlinear strain-hardening at the beginning of plastification. In more details, both transient ratchetting in stress-controlled uniaxial ratchetting test and the nonlinear strain-hardening at the beginning of plastification in strain-controlled tensile and cyclic tension-compression tests are dominated by the parameters of the first back-stress X_1 and viscous stress σ_{vis}. Therefore to achieve acceptable calculation results for strain-hardening, the consistency to the uniaxial ratchetting has to be somehow declined. Nevertheless considering the whole accordance regarding comparisons of all selected tests, the fitted parameters can still be treated as satisfying results.

5.6.3 Comparison for the ferritic material at room temperature

The fitted parameters for the ferritic material at room temperature are listed in table 5.3. The parameters correspond to the viscoplastic Chaboche model, in which Ohno-Wang approach II (equation 3.18), cyclic hardening/softening (equation 3.29), and strain-memory-effect are applied.

E	ν	Z	n	k	m_i	c_1	γ_1
210000	0.3	98.0	9.5	240	8	110370.0	1100.0
c_2	γ_2	c_3	γ_3	c_4	γ_4	a	b
14289.0	362.3	5587.0	131.0	5016.6	71.0	16.9	1.245
c	q_1	η	μ	Q_{max}	Q_0		
0.9	0.21	0.2	536.8	54.3	0.1		

Table 5.3: Fitted parameters of the viscoplastic Chaboche model including Ohno-Wang approach II for the ferritic material at room temperature.

Figure 5.11 shows the comparison between the calculated and measured yield curves regarding a uniaxial tensile test for the ferritic material at room temperature. Figure 5.12 illustrates experimental and calculated hysteresis loops corresponding to the first cycle of a uniaxial strain-controlled cyclic tension-compression test. Both tests were performed with the standard strain-rate $5 \times 10^{-4} / s$. The strain-range 1.5% was applied in the uniaxial cyclic tension-compression test.
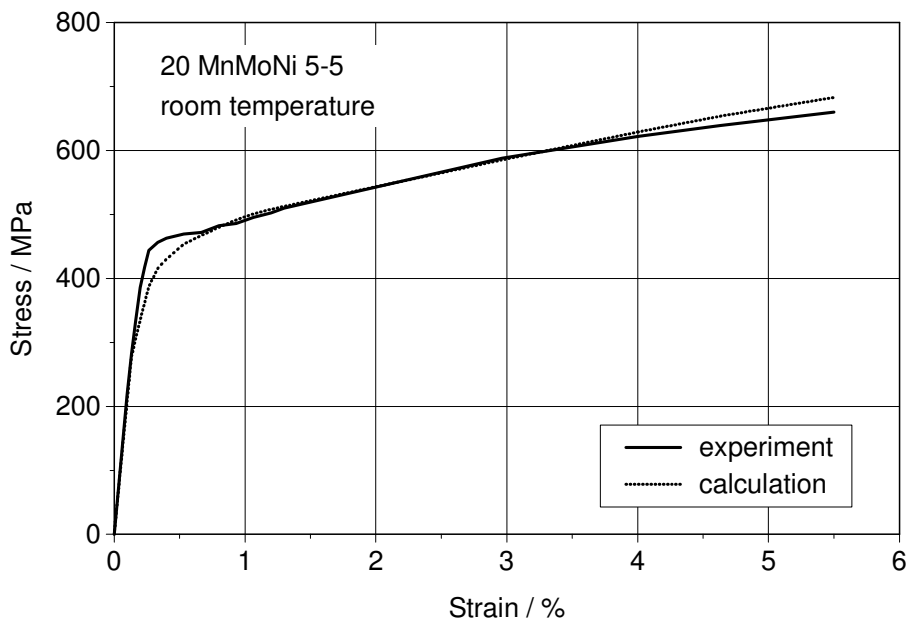

Figure 5.11: Comparison of measured and calculated yield curves for the ferritic material at room temperature.

It was known that the ferritic material 20 MnMoNi shows obvious initial yielding in the first cycle, especially at room temperature. Within the strain-range from 0.1% to 0.5%, an evident yielding stage can be detected, where a sharp bending is observed in this stage. This initial yielding stage appears only in the first loading procedure and will disappear in the loading procedure in compression of the first cycle as well as in the following cycles. This strong initial yielding in the first loading procedure of hysteresis loop is difficult to be described by the applied viscoplastic Chaboche model, therefore an obvious deflection can be found between the experimental and calculated curves in both figures. As shown in figure 5.12, since this behaviour disappears in the compression procedure of the first cycle, very good matching between experiment and calculation is again obtained during the yielding and hardening in compression.
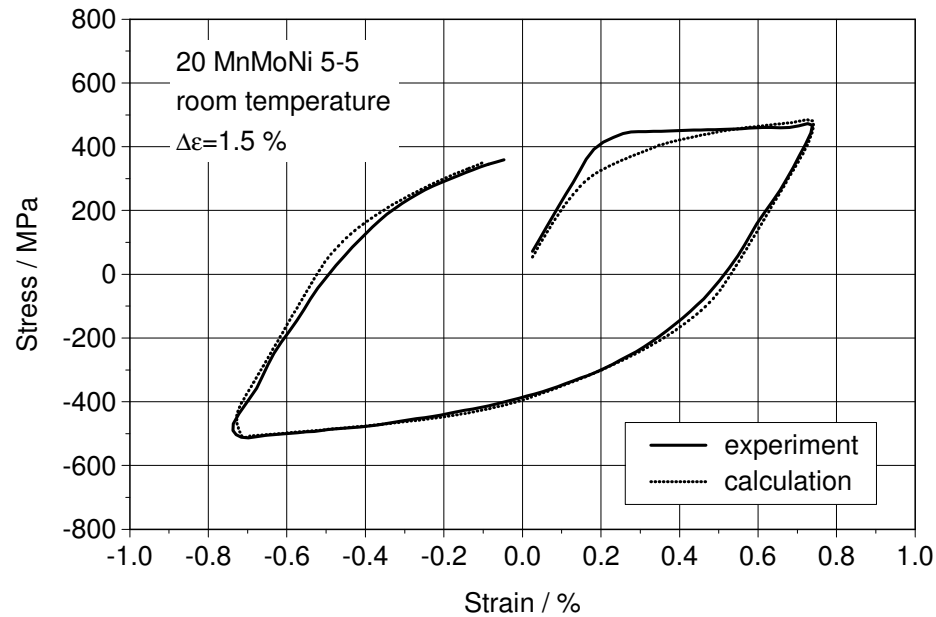
Figure 5.12: Comparison of measured and calculated hysteresis loops for the ferritic material at room temperature.
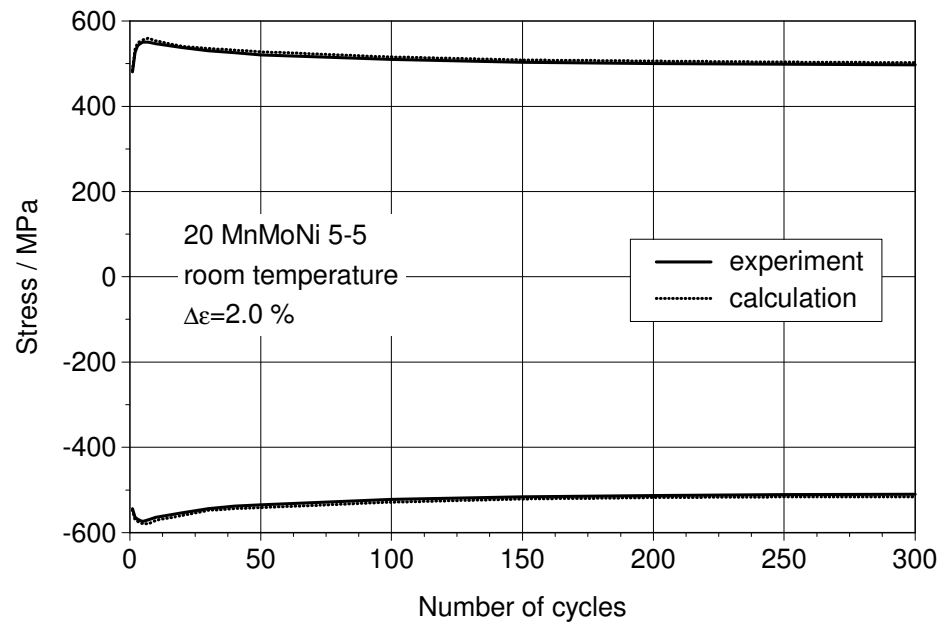

Figure 5.13: Comparison of the stress-ranges between experiment and calculation regarding uniaxial strain-controlled cyclic tension-compression test for the ferritic material at room temperature.

Figure 5.13 shows experimental and calculated cyclic hardening/softening curves regarding a uniaxial cyclic tension-compression test. The strain-range applied in the test

was 2.0% and stain-rate was specified to be the standard value $5 \times 10^{-4} / s$. As shown in the figure, the combined cyclic hardening/softening behaviour can be perfectly predicted with the material model by using the fitted parameters.

Figure 5.14 illustrates an uniaxial ratchetting test, in which stress-range 920 MPa was constantly applied in the stress-controlled uniaxial cyclic loading. The test was composed of two steps. In the first step, the stress-controlled cyclic load was fully reversed applied, namely the mean-stress equals zero and the ratio between minimum stress and maximum stress was $R = -1$. The second step started after 200 cycles, in which a mean-stress $\sigma_m = 100\text{MPa}$ was applied in the cyclic loading until the specimen failed at the 275th cycle. The experimental and calculated uniaxial ratchetting strains are demonstrated with respect to the number of cycles in the figure. Optimal consistency between the experiment and model prediction is presented, which indicates that by using adequate fitted parameters, the applied viscoplastic Chaboche model is able to correctly simulate uniaxial ratchetting induced by a large mean-stress.
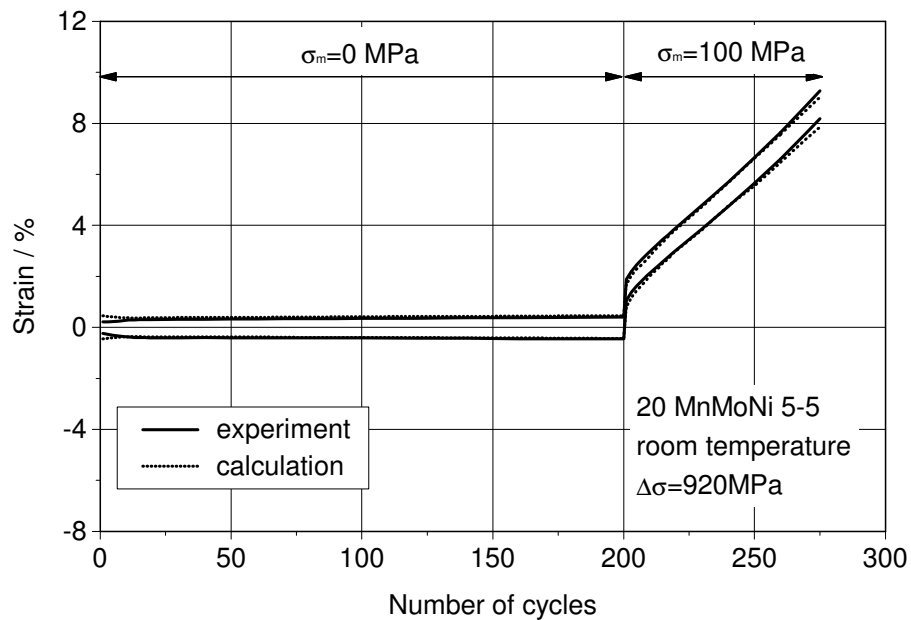

Figure 5.14: Comparison of the uniaxial ratchetting between experiment and calculation for the ferritic material at room temperature.

5.6.4 Comparison for the ferritic material at 300 °C

The fitted parameters for the ferritic material at 300 °C are listed in table 5.4. Since there were no uniaxial and multiaxial ratchetting tests performed for the ferritic material at 300 °C, the applied viscoplastic Chaboche model is composed of Armstrong-Frederick approach (equation 3.11) for kinematic hardening, combined cyclic hardening/softening approach (equation 3.29) for isotropic hardening, and evolution equations for the strain-memory-effect.

E	ν	Z	n	k	m_i	c_1	γ_1
186400	0.3	91.6	9.5	245	8	132110.0	1100.0
c_2	γ_2	c_3	γ_3	c_4	γ_4	a	b
19668.0	362.3	6000.0	131.0	3528.6	17.8	17.9	0.33
c	q_1	η	μ	Q_{max}	Q_0		
4.3	0.21	0.2	417.6	21.1	1.0		

Table 5.4: Fitted parameters of the viscoplastic Chaboche model including Armstrong-Frederick approach for the ferritic material at 300 °C.

Figure 5.15 shows the comparison between calculated yield curve and experimental measurements from a uniaxial tensile test ranging to 4.7%. Figure 5.16 presents the experimental and calculated hysteresis loops for the first cycle concerning a uniaxial cyclic tension-compression test performed with strain-range 3.0%. In both tests, the standard strain-rate 5×10^{-4} /s was applied. It can be detected that the hysteresis loops show very good agreement between experiment and model prediction. The comparison between calculated and experimental yield curves shows a slight deflection. By comparing the measured yield curve in figure 5.15 with the tensile procedure of the measured first hysteresis loop in figure 5.16, a slight deflection can be observed too. Although both tests were performed with the same strain-rate, the deflections can be found between the first loading procedures. These deflections can be attributed to the scattering of the material. Namely, the specimens made from the same material represent different hardening behaviour in the tensile and uniaxial cyclic tests due to the flaws in material. For the better prediction of cyclic behaviour, a compromise was made for the fitting of the yield curve, so that the uniaxial cyclic tension-compression test shown in figure 5.16 is better matched.
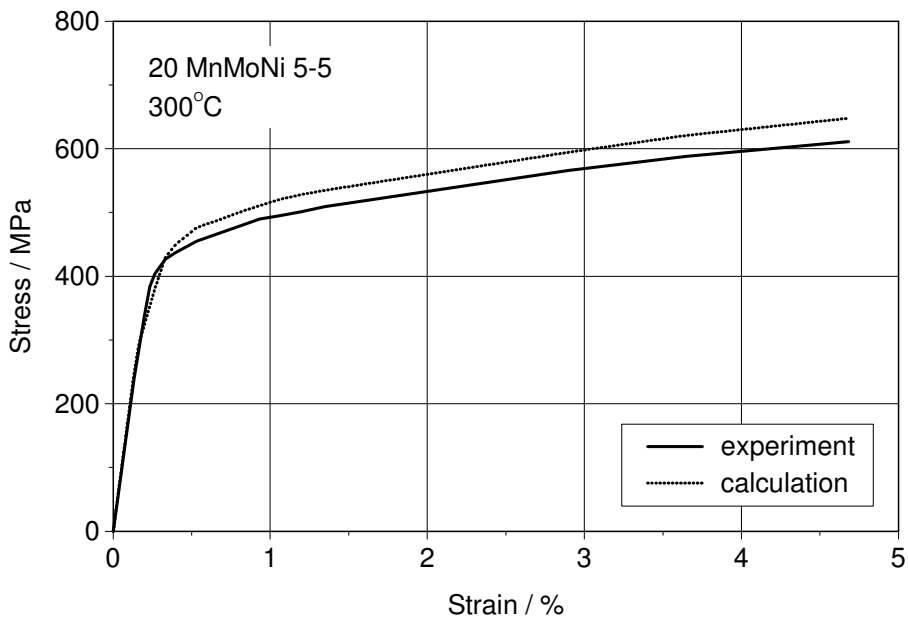
Figure 5.15: Comparison of measured and calculated yield curves for the ferritic material at 300°C.
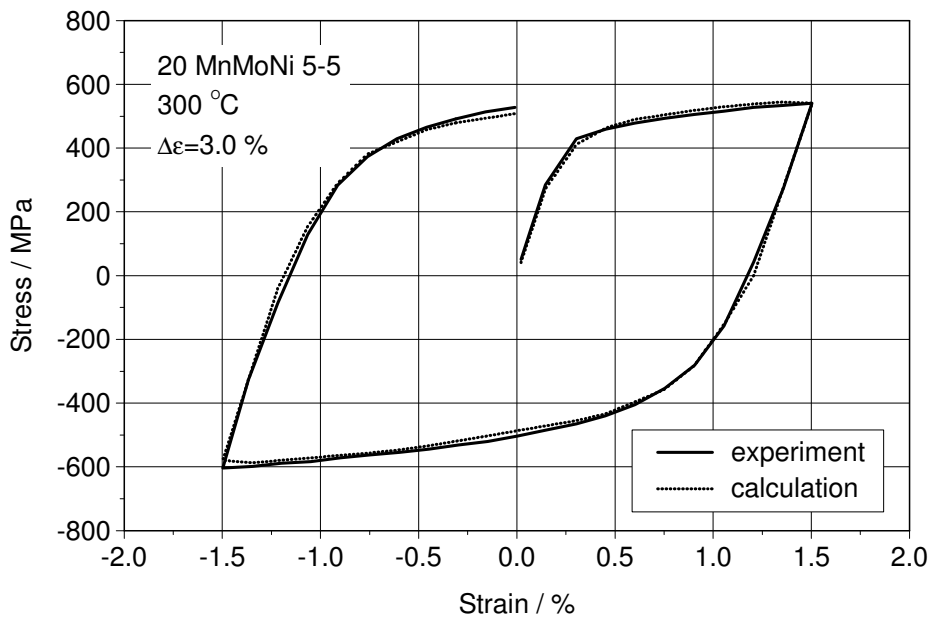

Figure 5.16: Comparison of measured and calculated hysteresis loop for the ferritic material at 300°C.

The experimental and calculated cyclic hardening/softening curves regarding an uniaxial cyclic tension-compression test with strain rage 2.0% and the standard strain-rate are illustrated in figure 5.17. The test was performed for the ferritic specimen at 300°C

using strain-range 2.0% and standard strain-rate. As shown in the figure, the com-bined cyclic hardening-softening behaviour can be perfectly predicted by the material model using corresponding fitted parameters.
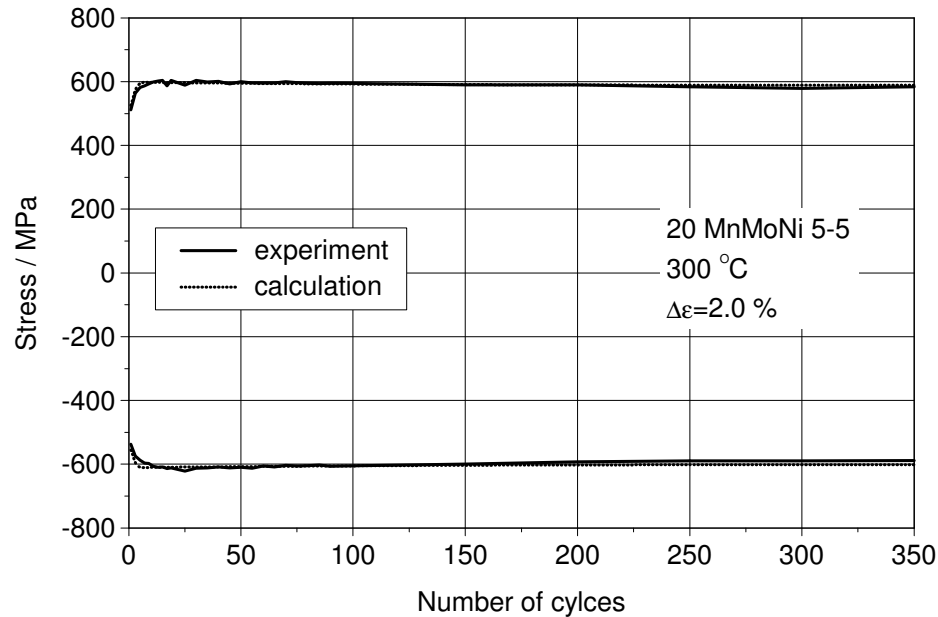

Figure 5.17: Stress-ranges comparison between experiment and calculation of uniaxial strain-controlled cyclic tension-compression test for the ferritic material at 300°C.

Furthermore, based on all comparisons of cyclic hardening/softening curves, it can be found that the calculations always present perfect predictions to the corresponding experimental curves. This is benefited from the separation of kinematic hardening and isotropic hardening in modelling. That is, by introducing kinematic and isotropic hard-ening variables into the viscoplastic material model, the cyclic hardening can be de-scribed independent from the strain-hardening, so that the fitting of cyclic harden-ing/softening behaviour is not influenced by the fitting of strain-hardening in hysteresis loops. On the other side, since the kinematic hardening is used to describe not only strain-hardening but also ratchetting behaviour, the compromise has to be made for the better predictions of both behaviour. This may reduce the accuracy of model pre-diction regarding individual test, e.g. the deflections between calculation and test shown in figures 5.6, 5.8 and 5.10.

6 Component tests

Beside the uniaxial LCF tests by using small specimens, multiaxial component tests were performed, which served as the verification of the material model in multiaxial stress-state. Straight pipe segments were used for the component tests. The total length of the component is 220mm. There are two square-shaped shoulders at the ends of the component, which is applied to fix the component in testing rig. The length of the shoulders is 60mm. The inner and outer diameter of the pipe segment is 20mm and 24mm, respectively. The cross-section of the shoulders is a hollow square with the edge length of 38mm. The component and its main dimensions are schematically illustrated in figure 6.1. The steel seal on the end surface shows the serial number of components.
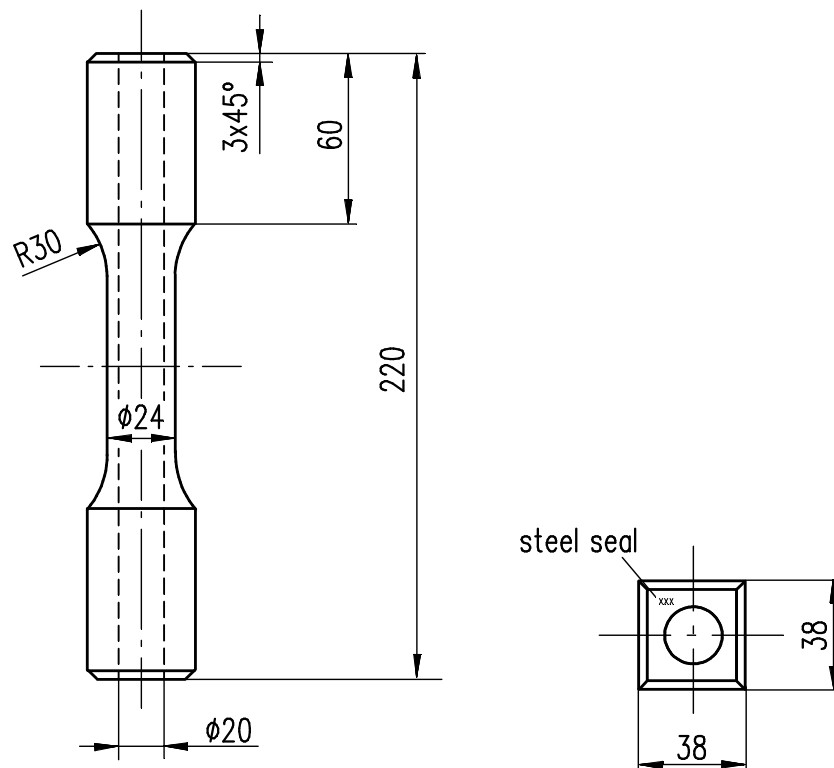

Figure 6.1: Schematic illustration of pipe component (dimensions in mm).

The multiaxial component tests were performed at room temperature and 300° by using a computer-controlled MTS testing machine. The pipe segment was vertically mounted on testing rig. It was gripped by hydraulic collets via two cylindrical blocks,

which have a square-shaped hole in the middle, as shown in figure 6.2. The function of the cylindrical blocks is to fasten the component on the testing rig, so that both torque and axial load can be applied on the shoulders of the component. During the testing process axial and torsional loads acting on component were measured by the corresponding load cells incorporated in the testing machine, while the axial and circumferential displacements on the outer surface of specimens were measured by using a two-axis-clip-gauge, which was fixed in the middle part of the pipe segment, as shown in figure 5.2. The gauge length was 50mm.
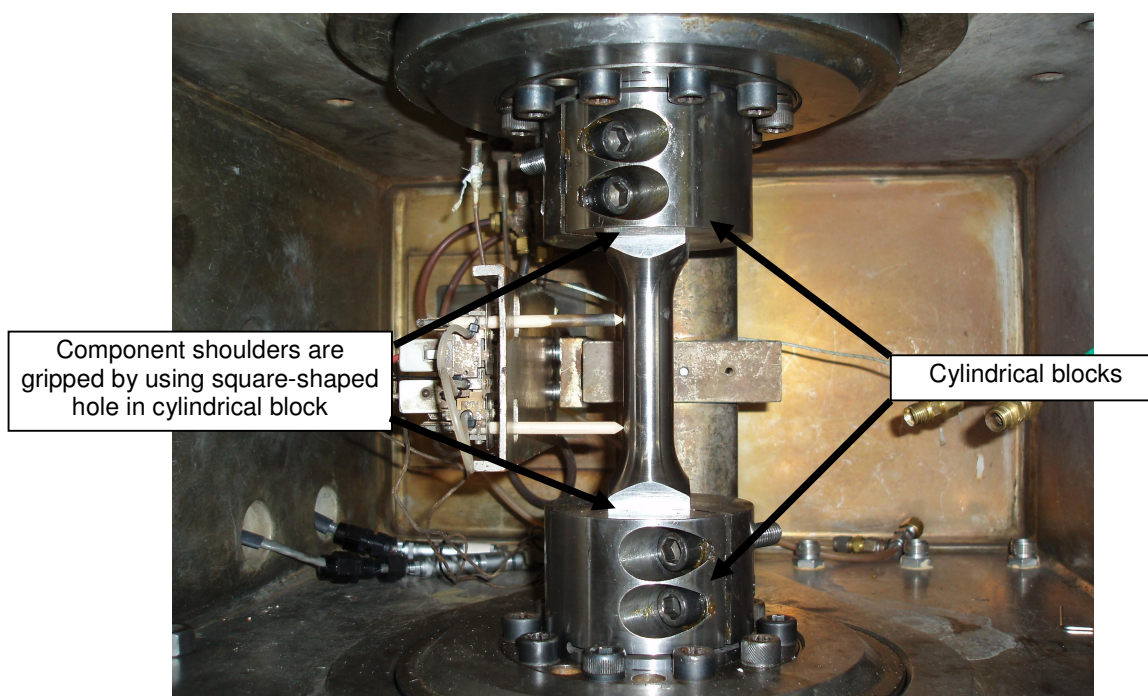

Figure 6.2: Setup of the multiaxial component test.

6.1 Experimental results of component tests for the austenitic material

For the austenitic material X6 CrNiNb 18-10, component tests were performed at room temperature and 300°C, respectively. At each temperature, a multiaxial ratchetting test, an in-phase-test and an out-of-phase-test were implemented, so that the multiaxial ratchetting behaviour as well as the effect of nonproportional cyclic loading can be studied. The multiaxial ratchetting tests were performed by applying axial constant tension and displacement-controlled cyclic torsion simultaneously. In the in-phase-tests, displacement-controlled cyclic axial load and cyclic torsion were in-phase applied, while in out-of-phase-tests, the displacement-controlled cyclic axial load and cy-

clic torsion were out-of-phase applied, which means the phase difference between cyclic tension and torsion is 90°C.

6.1.1 Ratchetting tests of the austenitic material

Ratchetting test for the austenitic material at room temperature was performed by applying axial tension and cyclic torsion simultaneously. In circumferential direction, cyclic torsion was displacement-controlled applied, so that the maximum and minimum displacements ±0.42mm in circumferential direction were reached, which yielded an equivalent strain-range $\Delta\varepsilon_{eq}$ of 1.0% and a mean-strain $\varepsilon_m = 0$. Since the torsion is linearly displacement-controlled applied and the loading period of 40 seconds was constantly for the cyclic torsion, the equivalent strain-rate $\dot{\varepsilon}_{eq}$ in the multiaxial ratchetting test corresponded to the standard strain-rate 5×10^{-4} /s applied in uniaxial tests. Here the equivalent strain-range $\Delta\varepsilon_{eq}$ was used to calculate the equivalent strain-rate $\dot{\varepsilon}_{eq}$, so that the strain-rate applied in multiaxial component test is comparable to the strain-rate applied in uniaxial tests. This equivalent strain-range and equivalent strain-rate in torsional direction were constantly applied during the whole procedure of the multiaxial ratchetting test. However, in axial direction, the application of axial tension was separated into two steps regarding different amplitudes of applied axial tension: In the first step, a constant axial tension of 2.76kN was applied in the first 100 cycles. In the second step, the axial tension was doubled to 5.53kN and kept until 7000 cycles were reached, at which incipient crack was detected in the component.

Figure 6.3 illustrates the range of torsional moment with respect to the number of loading cycle. The curves in the figure depict the maximum and minimum torsional moments at reverse points of displacement-controlled cyclic torsion. During the first 10 cycles, an obvious incipient cyclic hardening is detected. After approximate 20 cycles, the amplitude of torsional moment reaches the maximum value. In succession, the cyclic curves proceed with quasi-constant amplitude, so that it can be regarded as a neutral cyclic behaviour. In the second step, the neutral cyclic behaviour continues. The increment of axial tension does not evoke a visible change on the torsional direction, in another word: cyclic hardening in torsion is not influenced by the change of axial tension.
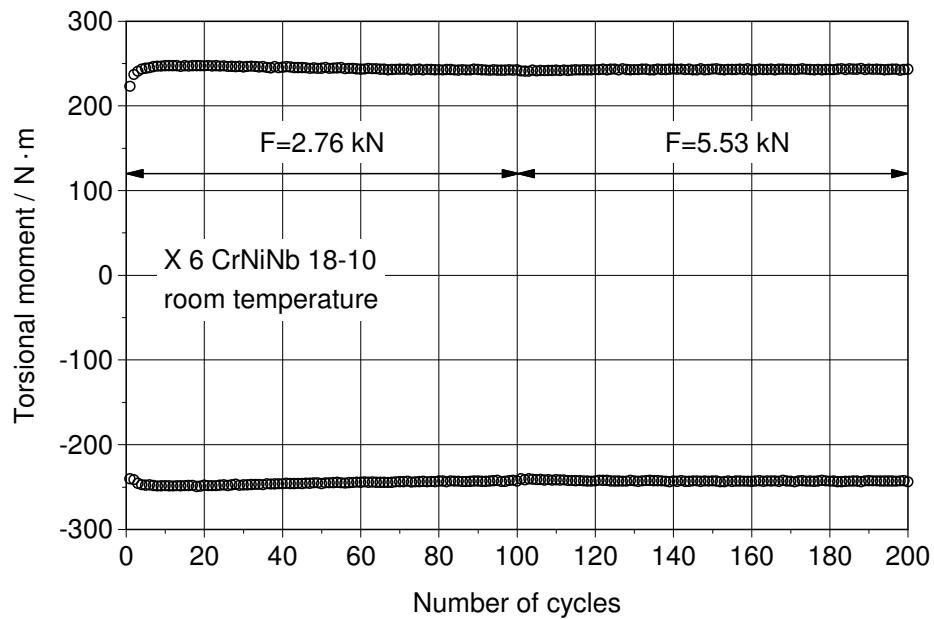
Figure 6.3: Torsional moments against the number of cycles for the austenitic material at room temperature.
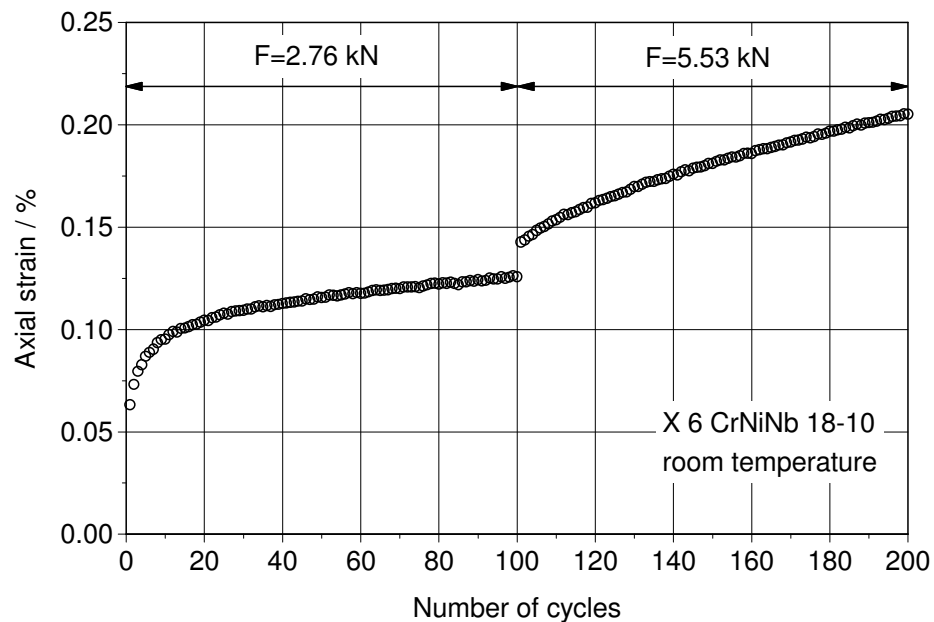

Figure 6.4: Multiaxial ratchetting strain against the number of cycles for the austenitic material at room temperature.

The accumulation of axial strain with respect to the number of cycles for the austenitic material at room temperature is illustrated in figure 6.4. Although the constant tensions were applied in axial direction, due to the cyclic plastification in torsional direction, an

accumulation plastic strain was still achieved in axial direction. This phenomenon presents the ratchetting behaviour in multiaxial stress-state, so called multiaxial ratchetting. Therefore the axial accumulated plastic strain can also be called multiaxial ratchetting strain. As discussed in chapter 2, ratchetting can be classified into transient ratchetting and asymptotic ratchetting. As shown in figure 6.4, transient ratchetting takes place during the start-up process in the first step, which corresponds to a strong nonlinear increase of ratchetting strain. After around 40 cycles, the increase of ratchetting strain is obviously diminished and trends to reach a steady state, so that a constant gradient of asymptotic ratchetting curve is achieved. At the end of the first step after 100 cycles, a ratchetting strain of 0.13% is reached. In the second step, transient ratchetting is evoked again due to the raise of axial tension. Nevertheless the magnitude of transient ratchetting is much less than that in the first step. Identical to the first step, the ratchetting strain tends to increase linearly after about 40 cycles. The gradient of the curve is obviously larger than that in the first step. After additionally 100 cycles in the second step, a ratchetting strain of 0.21% is reached.

Multiaxial ratchetting test for the austenitic material at 300°C was performed by using the same specifications as at room temperature: The amplitude of torsional displacement measured by the strain gauge was 0.42mm during the whole procedure of the test, which yields an equivalent strain-range $\Delta\varepsilon_{eq}$ of 1%. The applied equivalent strain-rate $\dot{\varepsilon}_{eq}$ accords with the standard strain-rate 5×10^{-4} /s in uniaxial tests. In axial direction, the constant axial tension of 2.76kN was applied in the first step, while in the second step the axial tension was doubled. Before the implementation of the test, the component was stepwise heated up to 300°C. The temperature was controlled via a thermal couple fixed on the surface of the component. In each step, temperature was increased slowly. After each increment, the temperature was kept for about 20 minutes before the next increase starts. Especially, after reaching 300°C, the temperature was kept for about one hour, so that the deformation of the component was homogeneous and no pre-stressing could occur.

The maximum and minimum torsional moments at reverse points of displacement-controlled cyclic torsion are shown in figure 6.5, which denote the cyclic hardening/softening behaviour of the austenitic material under multiaxial stress-state. The curves present incipient cyclic hardening in beginning stage. With the increase of load-

ing cycles, the range of torsional moment tends to reach a quasi-neutral behaviour in the first 100 cycles. In the second step, the quasi-neutral behaviour holds on. The increase of the axial tension doesn't influence the cyclic torsional behaviour. The slight discontinuity at the transient between the first and the second step is due to a restart of the testing machine for the recalibration of the clip-gauge, which should be neglected.
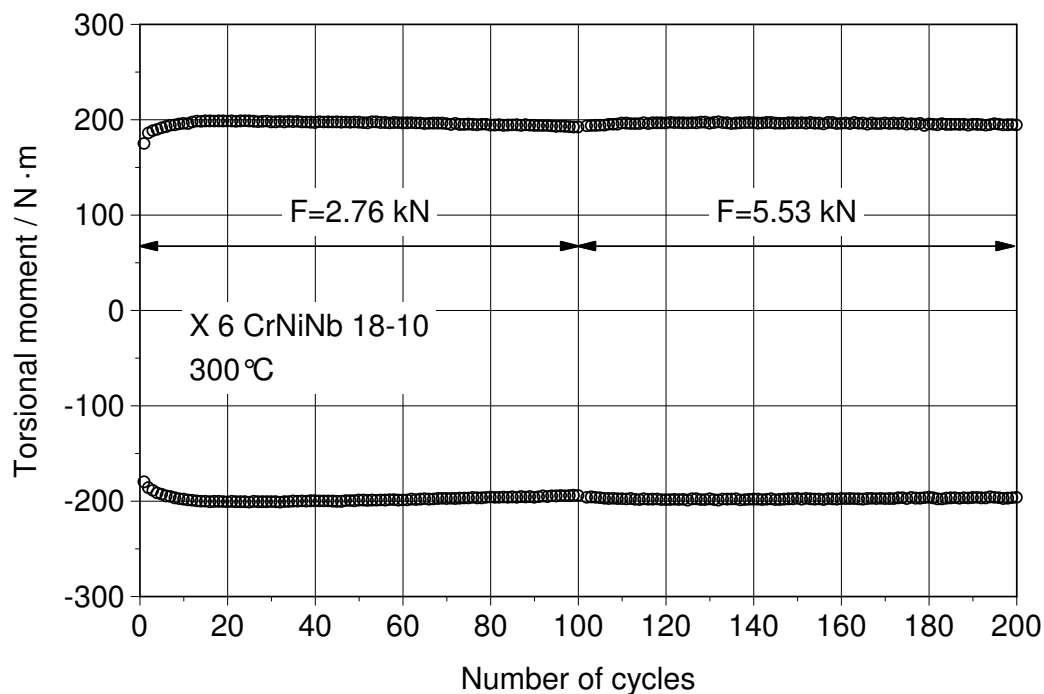

Figure 6.5: Torsional moment against the number of cycles for the austenitic material at 300°C.

The multiaxial ratchetting strain for the austenitic material at 300°C is illustrated in figure 6.6, where the axial accumulated plastic strain is depicted with respect to the increase of cyclic torsional loading. At the beginning of the test, the multiaxial ratchetting strain increases rapidly, which shows a clear transient ratchetting procedure. After approximately 40 cycles, the ratchetting curve trends to proceed with a linear increase. After 100 cycles, a ratchetting strain of 0.22% is achieved. It can be seen that the ratchetting curve isn't as smooth as that at room temperature. The slight discontinuities and oscillations in the curve can be attributed to the unexpected oscillation of temperature during the testing process, which should be ignored. In the second step, the ratchetting strain progresses with an evident increase again due to the enhancement

of axial load. Compared with the first step, the magnitude of transient ratchetting in the second step is much less, whereas the gradient of the asymptotic ratchetting is much larger than that in the first step. After 200 cycles, a ratchetting strain of 0.45% is reached.
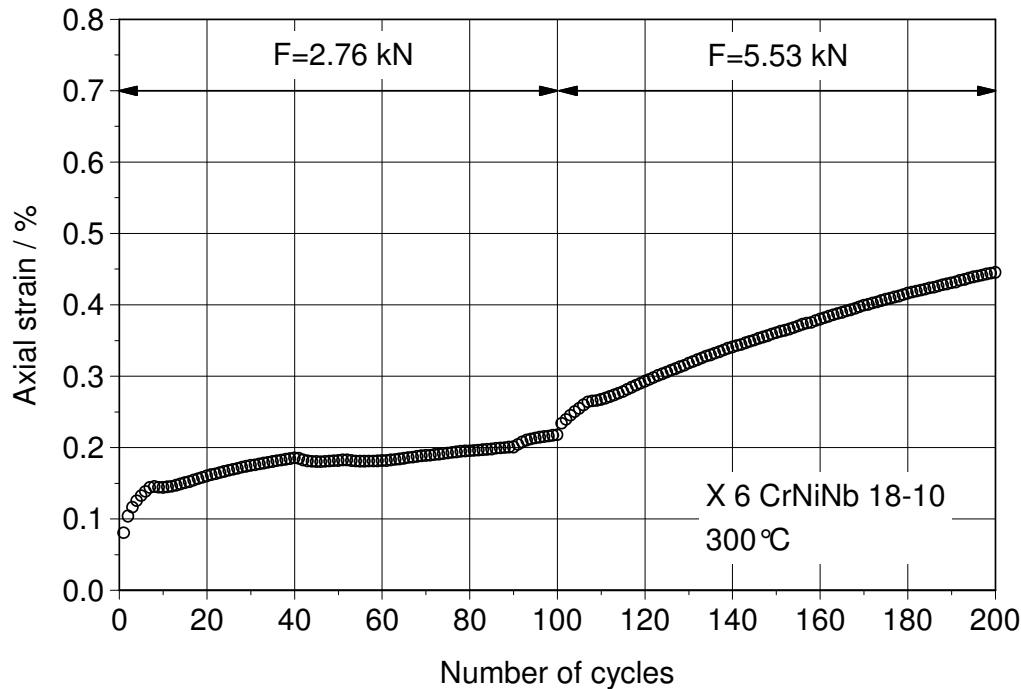

Figure 6.6: Multiaxial ratchetting strain against the number of cycles for the austenitic material at 300 °C.

In above two multiaxial ratchetting tests, the results are presented separately in torsional direction and in axial direction. In torsional direction, the displacement controlled cyclic torsion was applied, and the curves of maximum and minimum torsional moments were denoted. By these results, the cyclic hardening/softening behaviour can be studied. In axial direction, the multiaxial ratchetting, which is understood as axial accumulated plastic strain, was presented, by which the multiaxial ratchetting behaviour can be investigated. As mentioned in chapter 2.7, ratchetting may lead to earlier failure of components. In the frame of research work for ratchetting, the especially defined primary and secondary stresses are used. Correspondingly, if ratchetting occurs in multiaxial stress-state, the failure behaviour is dominated by the multiaxial ratchetting strain. Therefore the results of these multiaxial ratchetting tests are presented in axial direction, in which ratchetting is in presence, and torsional direction, separately.

6.1.2 Multiaxial component tests of the austenitic material under nonproportional cyclic loading

If the component sustains multiaxial cyclic loading, during which the directions of principal stress planes and the ratios between the magnitudes of principal stresses are changing, this kind of cyclic loading is so-called nonproportional cyclic loading. It has been found out, that the nonproportional cyclic loading yields additional cyclic hardening [33], [51]. For the investigation of the cyclic viscoplastic behaviour of the austenitic component in multiaxial stress-state and the influence of the nonproportional loading, in-phase-tests and out-of-phase-tests were performed by applying cyclic torsion and cyclic axial load simultaneously to the component at room temperature and 300°C, respectively. It should be emphasized that the tests presented in this chapter are only to study the effect of nonproportional loading, so they are not related to ratchetting.
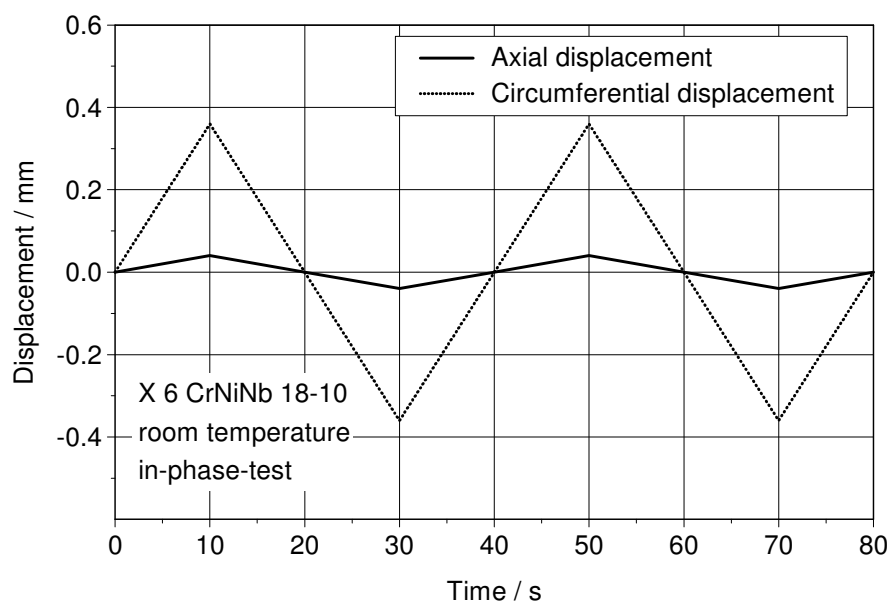

Figure 6.7: Illustration of displacement-controlled in-phase-test.

Figure 6.7 illustrates the loading-unloading method of the in-phase-test. The cyclic torsional and cyclic axial loads were displacement controlled and in-phase applied, so that the displacements in circumferential and axial directions kept always in-phase. That is, when the circumferential displacement under torsion reaches the maximum or minimum values, the axial displacement reaches corresponding maximum or minimum values too. Since the changes of displacement in circumferential and axial directions

are always in-phase, this kind of test is named as in-phase-test. For austenitic component at room temperature and 300°C, the amplitude of the cyclic circumferential displacement was specified to ± 0.36mm, while the amplitude of the cyclic axial displacement was set to 0.04mm. The equivalent strain-range $\Delta\varepsilon_{eq}$ was 1.0% and the applied equivalent strain-rate $\dot{\varepsilon}_{eq}$ was 5×10^{-4}/s.
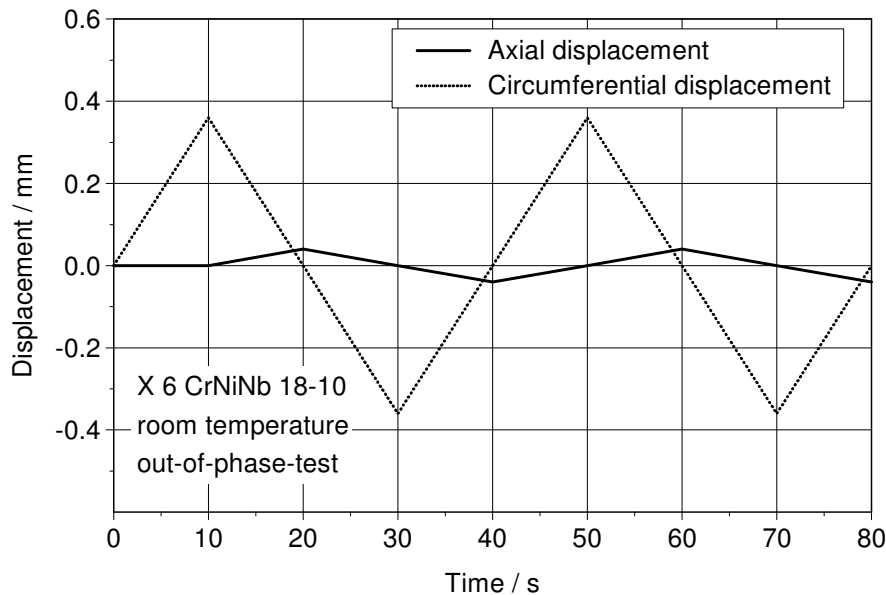

Figure 6.8: Illustration of displacement-controlled out-of-phase-test.

Figure 6.8 illustrates the loading configuration of the out-of-phase test for the austenitic material at room temperature. Instead of the in-phase applied cyclic loads, the cyclic axial load was applied in the out-of-phase test with a phase shift of π/2 to the cyclic torsion. As shown in the figure 6.8, in the out-of-phase test, the maximum and minimum torsional and axial displacements measured by the strain gauge always had a phase difference of π/2, while in the in-phase test the phase difference is zero, so that the maximum and minimum displacements were always reached at the same time. The amplitudes of cyclic torsional and axial displacements specified for the out-of-phase-tests at room temperature and 300°C are the same as those specified in the in-phase-test, so that the results of the in-phase-test and out-of-phase-test are comparable.

The results of in-phase-test and out-of-phase-test for the austenitic material at room temperature are demonstrated in figure 6.9 and figure 6.10. Figure 6.9 illustrates the

maximum and minimum of torsional moment at reverse points with respect to the number of cycles in the in-phase-test and out-of-phase-test, respectively. In both tests, the curves of torsional moment presented incipient cyclic hardening in the beginning. After about 20 cycles, the amplitudes of torsional moments reached the maximum values, and then cyclic softening occurred consequently.

Similar behaviour can be found in axial load. As shown in figure 6.10, the curves of maximum and minimum of axial loads at reverse points against the number of cycles show cyclic hardening in the beginning. Nevertheless, instead of a cyclic softening, the curves show quasi-neutral behaviour after the saturation of the hardening. It is noticed that, in the in-phase-test, the maximum and minimum curves shift down in parallel during cycle 20-40. This phenomenon did not reflect the real cyclic behaviour of the material. It was caused by an unexpected sliding of the clip-gauge on the surface of component during the cycle 20-40. In the evaluation of testing results, this phenomenon should be ignored.
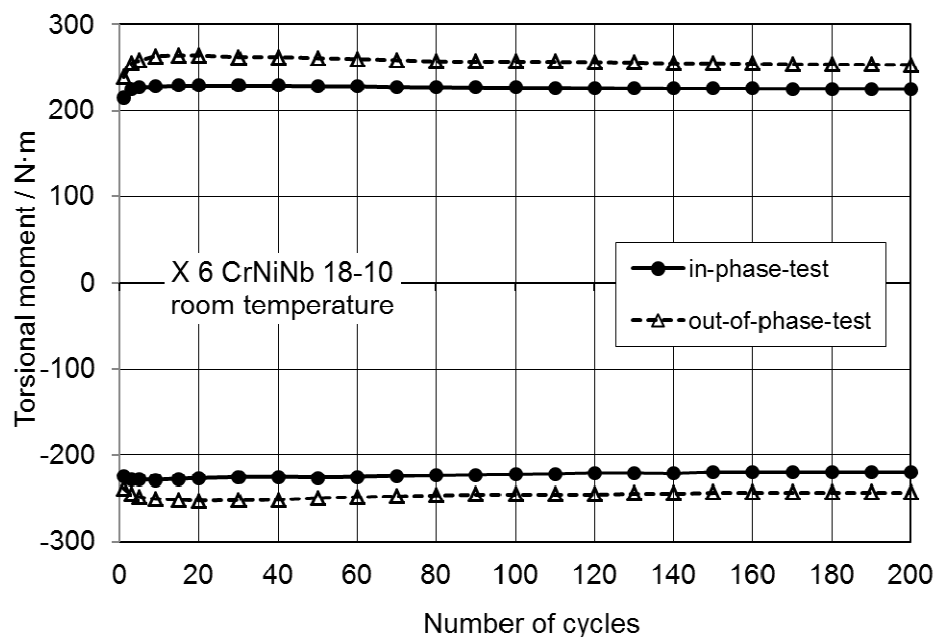

Figure 6.9: Torsional moment against the number of cycles in in-phase-test and out-of-phase-test for the austenitic material at room temperature.
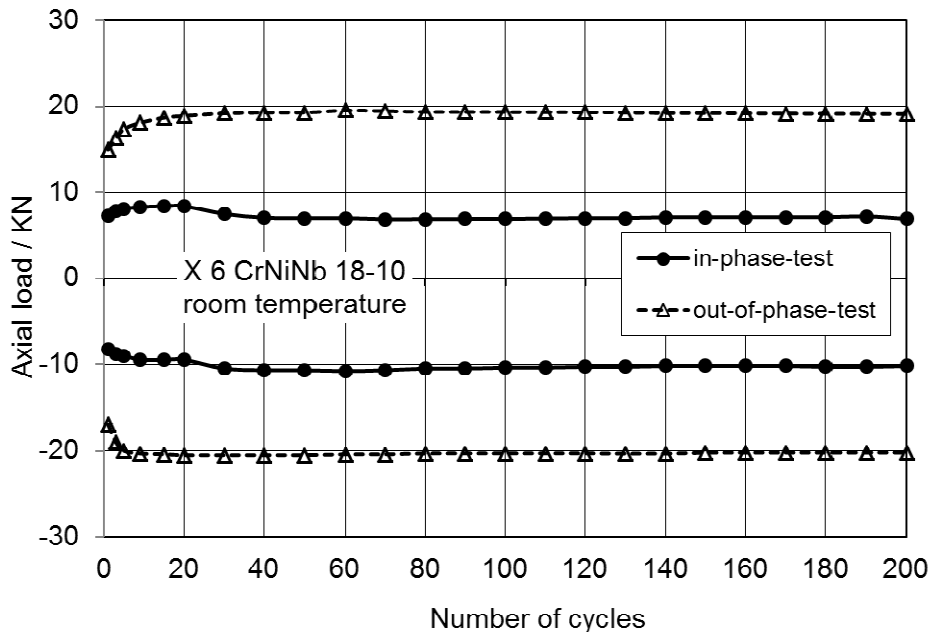
Figure 6.10: Axial load against the number of cycles in in-phase-test and out-of-phase-test for the austenitic material at room temperature.

An interesting factor, which should be emphasized here, is that additional cyclic hardening was evoked in the out-of-phase test. As shown in figure 6.9, the cyclic hardening of torsional moment in the out-of-phase-test presents an increase of around 15% compared with that in the in-phase-test. Likewise, the cyclic hardening of axial loading in out-of-phase-test is increased by a factor of 2 approximately, which is shown in figure 6.10. This phenomenon regarding evoked additional hardening in out-of-phase-test can be attributed to the effect of the multiaxial nonproportional cyclic loading.

In addition, due to the additional cyclic hardening evoked by the nonproportionality of multiaxial cyclic loading, the crack was earlier detected in the out-of-phase-test than in the in-phase-test. That is, the in-phase-test lasted 17100 cycles till an incipient crack was detected in the specimen, whereas the out-phase-test lasted only 4470 cycles. It can be seen, that although the equivalent strain-range applied in the in-phase-test and out-of-phase-test are the same, due to the effect of multiaxial nonproportional cyclic loading the fatigue life in the out-of-phase-test is much lower than that in the in-phase-test. These results proved again that if the multiaxial nonproportional cyclic loading is present in the service of component, using von Mises equivalent strain and strain-life fatigue theory to estimate the fatigue life is very inaccurate. It's the reason, why it's

worthwhile to investigate the additional cyclic hardening evoked by multiaxial nonproportional cyclic loading.

For facilitating the comparisons, in-phase- and out-of-phase-tests for the austenitic material at 300°C were performed by using the same specifications as applied at room temperature. The corresponding testing results are illustrated in figure 6.11 and figure 6.12. Same as at room temperature, the results at 300°C are demonstrated by using the cyclic hardening/softening curves of torsional moment and axial load with respect to the number of cycles. The additional hardening due to nonproportional cyclic loading can also be detected in the out-of-phase-test at 300°C. The component tests show the same temperature-dependent hardening behaviour as that in uniaxial tests. Namely, under the same cyclic loading, the amplitudes of torsional moment and axial load are lower than the corresponding values at room temperature. Nevertheless the magnitudes of the additional hardenings evoked by nonproportional loading are comparable to those at room temperature. For investigating whether the additional hardening of the austenitic material evoked by multiaxial nonproportional cyclic loading is dependent on temperature, more component tests under different nonproportionalities and different temperatures should be performed and evaluated. The current test results are insufficient to summarize the relationship between the additional hardening due to nonproportional loading and temperature.

Additionally, the effect of multiaxial nonproportional cyclic loading can also be reflected by the fatigue life of components at 300°C: The component subjected to the out-of-phase loading lasted 6586 cycles till the incipient crack appeared, whereas the component subjected to the in-phase loading lasted 10558 cycles. By comparing the fatigue lives of the in-phase-test and the out-of-phase-test at room temperature, it can be seen, that regarding the out-of-phase-test the fatigue life at 300°C is less than that at room temperature. Nevertheless regarding the in-phase-test the fatigue life at 300°C is larger. This result can be understood as the scattering of the material. For getting more accurate results of fatigue life, the statistical life should be evaluated from at least five specimens for each test.
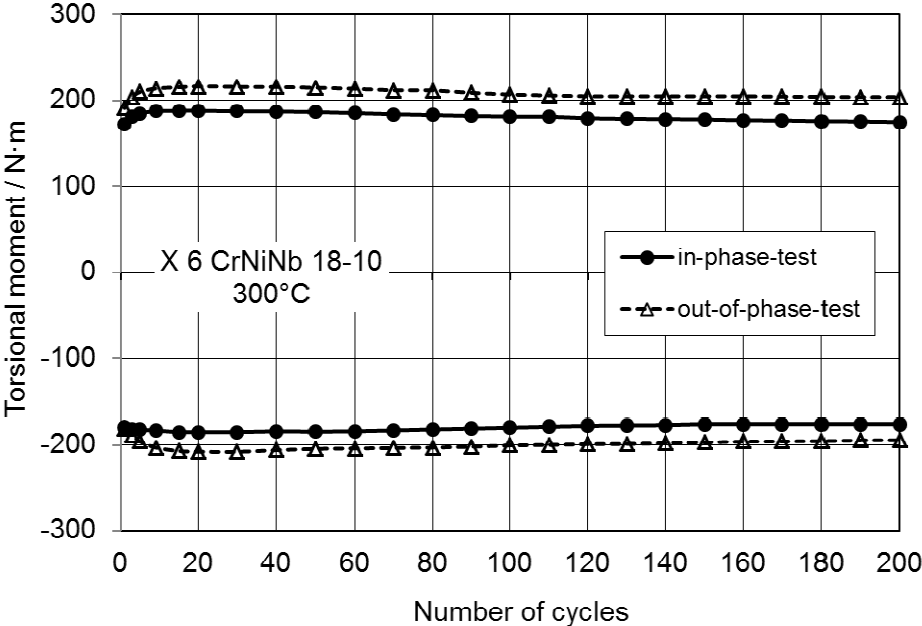
Figure 6.11: Torsional moment against the number of cycles in in-phase-test and out-of-phase-test for the austenitic material at 300 °C.
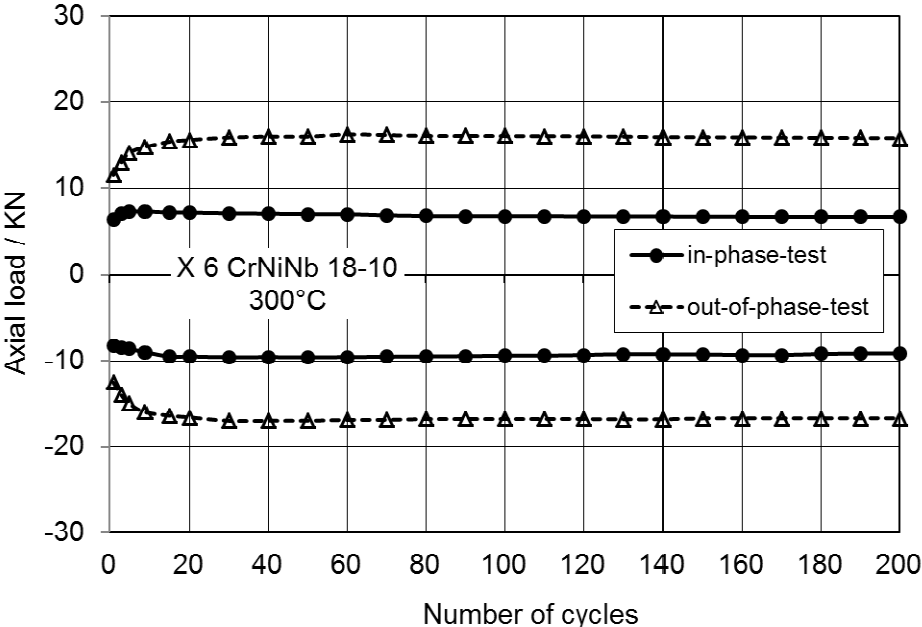

Figure 6.12: Axial load against the number of cycles in in-phase-test and out-of-phase-test for the austenitic material at 300 °C.

6.2 Experimental results of component tests for the ferritic material 20MnMoNi

Component tests were performed for the ferritic material at room temperature. Ferritic pipe components, which have the same dimensions as austenitic components were used. A ratchetting test, an in-phase-test and an out-of phase test were performed.

6.2.1 Ratchetting test of the ferritic material

Ratchetting component test for the ferritic material at room temperature was performed in the similar way as the test for the austenitic material. A cyclic torsional load and a constant axial tensile load were applied to the component. The cyclic torsional load was displacement-controlled applied. The amplitude of cyclic circumferential displacement ± 0.72mm was fully reversed applied, which yielded an equivalent strain-range $\Delta\varepsilon_{eq}$ of 2.0% and a mean-strain $\varepsilon_m = 0$. In order to study the ratchetting behaviour under a high primary stress, a higher constant axial tensile load, 15kN, was applied to the ferritic component. The period of the cyclic loading was set to 80 seconds, so that the equivalent strain-rate $\dot{\varepsilon}_{eq}$ corresponded to the standard strain-rate 5x10^-4/s in the uniaxial tests. Since a large axial load was applied, the ratchetting test lasted only 419 cycles till incipient crack was detected.

The maximum and minimum torsional moments at reverse points with respect to the number of cycles are illustrated in figure 6.13. The incipient cyclic hardening arises in the beginning of the cyclic loading and reaches saturation within 10 cycles. A cyclic softening appears following the incipient cyclic hardening stage. The magnitude of the cyclic softening is evident and significantly larger than that of austenitic material.

Figure 6.14 shows the ratchetting behaviour of the ferritic material at room temperature, where the ratchetting strain is illustrated with respect to the number of cycles. Since a high axial load was applied, the gradient of asymptotic ratchetting is significantly increased, so that asymptotic ratchetting dominates the whole ratchetting behaviour, and there is no clear dividing between transient ratchetting and asymptotic ratchetting. The increase of the ratchetting strain arises from beginning. After about 50

cycles, it proceeds quasi linearly with a steep slope. After 100 cycles, the ratchetting strain of 4.35% is achieved.
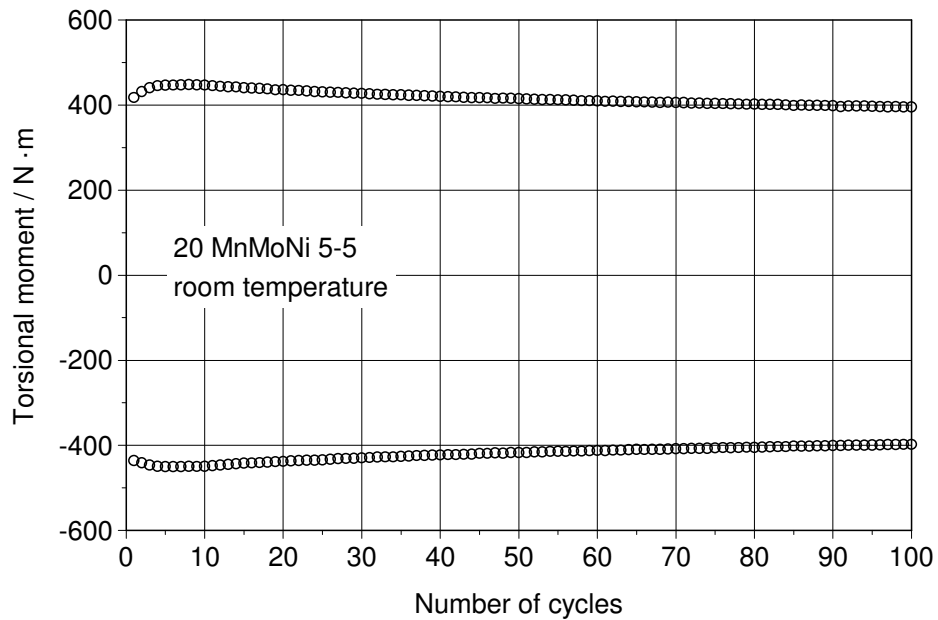

Figure 6.13: Torsional moment against the number of cycles for the ferritic material at room temperature.
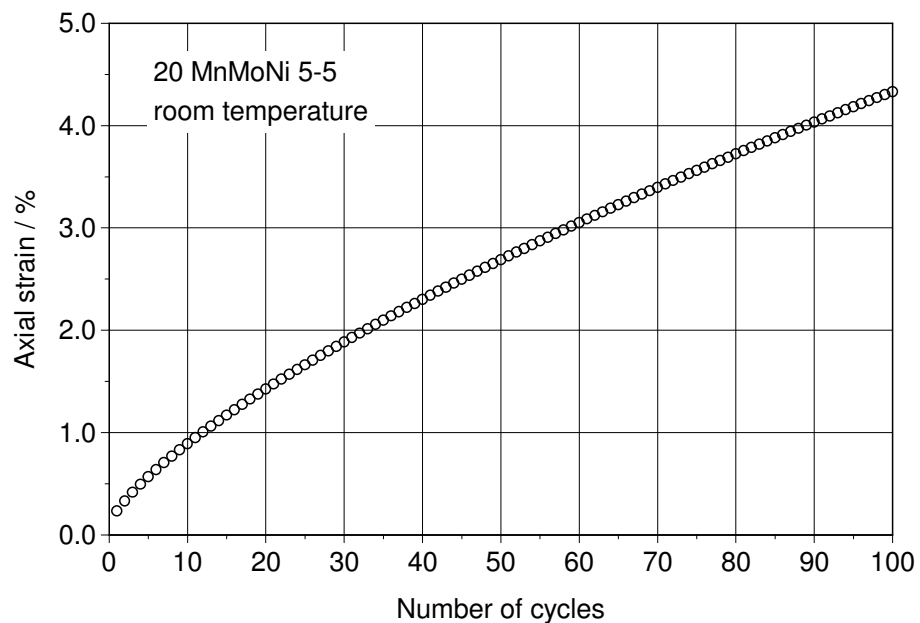

Figure 6.14: Multiaxial ratchetting strain against the number of cycles for the ferritic material at room temperature.

6.2.2 Multiaxial component tests of the ferritic material under nonproportional loading

To study the effect of multiaxial nonproportional cyclic loading for the ferritic material, the multiaxial component tests under proportional cyclic loading and nonproportional cyclic loading were performed by using ferritic components too. The applications of proportional and nonproportional cyclic loading were realized via the in-phase-test and out-of-phase-test like for the austenitic material. The in-phase and out-of-phase cyclic torsion and cyclic axial tension/compression were applied using the way as illustrated in figures 6.7 and 6.8. However the amplitudes of circumferential and axial displacements for the ferritic material were changed to 0.72mm and 0.08mm, respectively, which were twice of the equivalent strain-range applied for the austenitic material, namely $\Delta\varepsilon_e = 2\%$. Accordingly, the periods of applied cyclic loads were specified to 80 seconds, so that the applied equivalent strain-rate $\dot{\varepsilon}_{eq}$ equals the standard strain-rate 5×10^{-4} /s in uniaxial test.

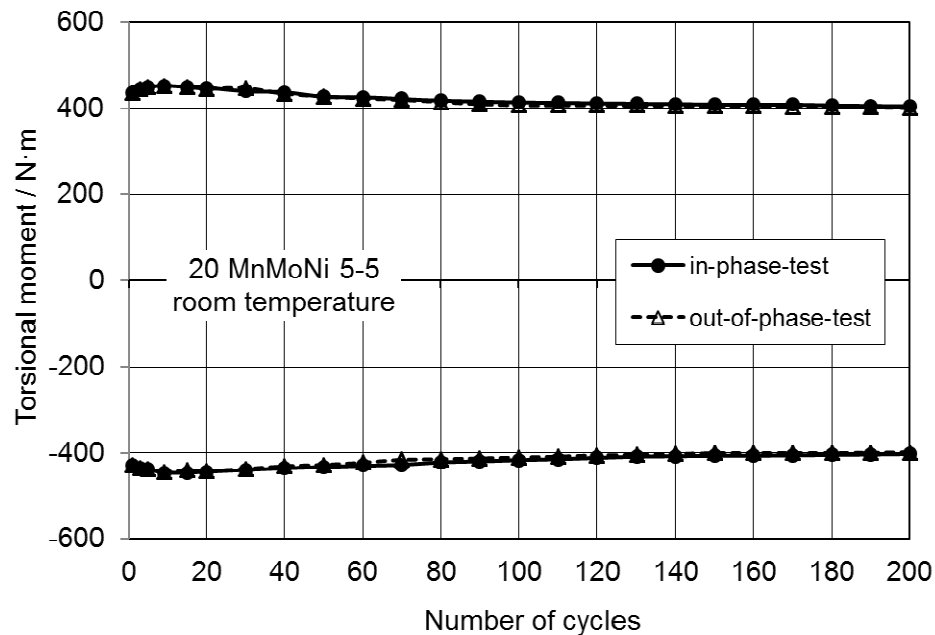Figure 6.15: Torsional moment against the number of cycles in in-phase-test and out-of-phase-test for the ferritic material at room temperature.

Figure 6.15 illustrates the ranges of torsional moments in the in-phase-test and out-of-phase-test with respect to the number of cycles at room temperature. It can be seen that both curves show incipient cyclic hardening in the beginning. After several cycles,

cyclic softening occurs instead of cyclic hardening. Furthermore the torsional moments in both tests present almost the same cyclic behaviour, so that two curves congruent with each other.

In the axial direction, as shown in figure 6.16, the out-of-phase test presented significant cyclic softening like in the circumferential direction, whereas the in-phase-test showed quasi-neutral cyclic behaviour. Regarding the effect of nonproportional loading, pronounced additionally hardening can be found in the out-of-phase-test in the axial direction.
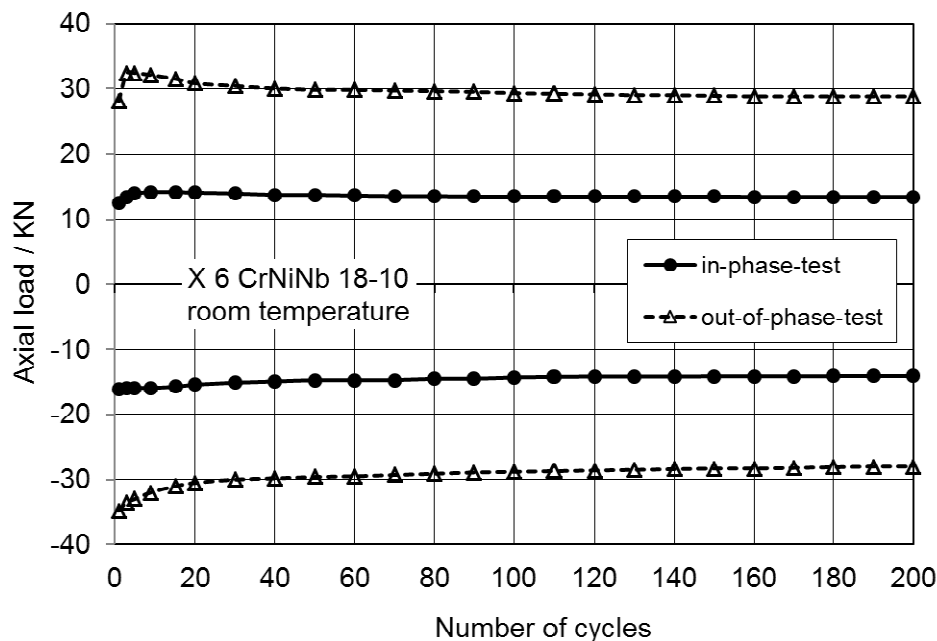
Figure 6.16: Axial load with respect to the number of cycles in in-phase-test and out-of-phase-test for the ferritic material at room temperature.

Considering the effect of nonproportional loading, additional hardening was expected in the out-of-phase test in both axial and circumferential directions. Nevertheless, as shown in figures 6.15 and 6.16, additional hardening was only detected in axial direction, in which the amplitude of axial load in the out-of-phase-test is 2 times larger than that in the in-phase-test, while in circumferential direction, the cyclic hardening/softening curves of the in-phase-test and the out-of-phase-test present completely the same magnitude in hardening and softening. The reason can be supposed that this special behaviour presented in these two tests is either due to the special material property of the ferritic material 20 MnMoNi 5-5, or because of the scattering of the ma-

terial. Due to the lack of testing samples, the real reason of it is still in doubt. Therefore more in-phase- and out-of-phase-tests should be performed for the further study of nonproportional effect for the ferritic material.

Although there is no additional hardening was observed in torsional direction, the additional hardening evoke in axial direction still causes earlier failure in the out-of-phase-test. That is, the in-phase-test lasted 999 cycles till the occurrence of incipient crack, while the out-of-phase-test lasted only 261 cycles.

7   Finite element analyses

7.1   Construction of FE model

The Finite-Element-Method (FEM) is the most widely used numerical method for the computation of stress- and strain-state in complex structure. To perform FE analysis, FE model should be setup. Compared to calculations for monotonic loading, numerical analyses by using FEM for cyclic loaded components are more complicated. Since the computational time and disk space required for cyclic loaded calculations are greatly multiplied in comparison with the monotonic loaded analyses. Due to this reason, the FE model should be simplified as far as possible, so that computational time and disk space for the storage of calculated data can be maximum saved.
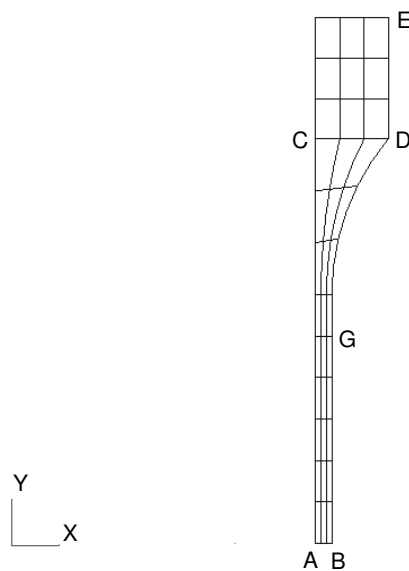
Figure 7.1: Axisymmetric FE model of the pipe segment component.

In the frame of this research work, a FE model was constructed by using commercial FEM pre-processing software PATRAN [88]. Based on the symmetric conditions, an axisymmetric model was built up by using axisymmetric 8-node biquadratic elements, which corresponds to a quarter of the cross-section of the pipe segment component, as shown in figure 7.1. The model contains 36 elements and 139 nodes.

According to symmetric conditions, displacement in y direction and rotation around y axis are fixed at all nodes along path AB at the bottom of the model. Axial load and torsional moment were acted on nodes along path CD and DE, respectively. Point G corresponds to the application point of the strain gauge in component tests. In displacement-controlled component tests as discussed in chapter 6, the displacements of strain gauge clip were recorded regarding the gauge application point. While the recorded displacements at the gauge application point reached the maximum values, the applied loads reversed. Accordingly, in FE analyses, the displacement at point G should be studied. Due to the change of the plastification and hardening during the cyclic loading, the ratio of the circumferential displacement on the path DE to that at point G is not constantly kept. Therefore by using model in figure 7.1, it is difficult to guarantee constant amplitude of circumferential displacement and constant strain-rate at the gauge point G. Consequently, for implementing FE analyses more efficiently, the model shown in figure 7.1 should be further simplified.
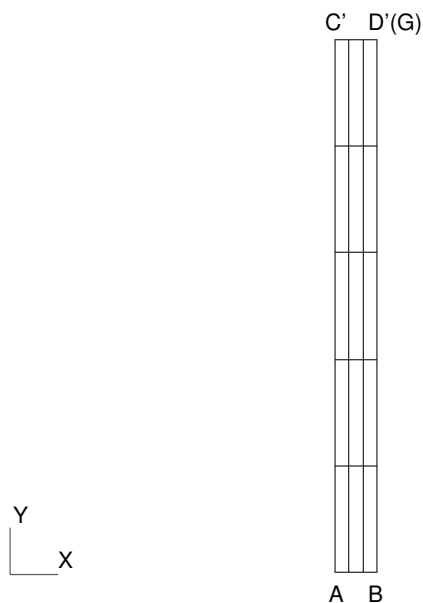

Figure 7.2: Simplified FE model.

Figure 7.2 illustrates a simplified FE model, which is composed of 15 elements and 62 nodes. It is a fraction of the model shown in figure 7.1, where the shoulder of the component is neglected. The length of this simplified model corresponds to the half of the length between the two application points of strain gauge clip. The boundary condi-

tions were identically defined along path AB as in figure 7.1. Distributed axial load was applied on path C'D', while torsional moment around Y axis was displacement-controlled applied at nodes along path C'D'. Point D' corresponds to the gauge application point G in figure 7.1.

7.2 Investigation of introduced kinematic and isotropic hardening approaches in the viscoplastic Chaboche Model

In the frame of this work, FE analyses were performed by using commercial FEM program ABAQUS 6.3 [72]. The complete viscoplastic Chaboche model was constructed in ABAQUS user's subroutine UMAT, as discussed in chapter 3. The newest version of ABAQUS provides its own material models for the simulation of time-dependent cyclic plasticity. Nevertheless they are not flexible and comprehensive compared to the viscoplastic Chaboche model developed in this work. Especially, the models provided by ABAQUS are not sufficient to describe ratchetting behaviour and nonproportional loading effect for metallic materials.

In this chapter, the results of FEA using the viscoplastic Chaboche model with different kinematic and isotropic hardening approaches, which were introduced in chapter 3, will be presented and discussed. These results can be used to qualitatively compare the functionalities of applied kinematic and isotropic hardening approaches and perform parameter studies. The FEA results using the viscoplastic Chaboche model and fitted parameters from chapter 5 and the results of components tests will be compared and discussed in chapter 7.3.

7.2.1 Qualitative investigation of the material model for multiaxial ratchetting

First of all, the functionalities of the viscoplastic Chaboche model with different isotropic hardening approaches for predicting cyclic hardening/softening behaviour are investigated. As discussed in chapter 3, by using different isotropic hardening approaches in the viscoplastic Chaboche model, different cyclic hardening/softening behaviour can be simulated. Namely, continuous cyclic hardening, saturated cyclic hardening and combined cyclic hardening and softening. For study the functionality of the material model, FE calculations corresponding to a pure torsional test were imple-

mented by using the simplified FE model for the austenitic material at room temperature. A cyclic displacement-controlled torsional load was applied, so that the amplitude of the cyclic strain was kept to be 0.87%. The period of a loading cycle was specified to 40 seconds, so that the applied equivalent strain-rate $\dot{\varepsilon}_{eq}$ was $5 \times 10^{-4} / s$.
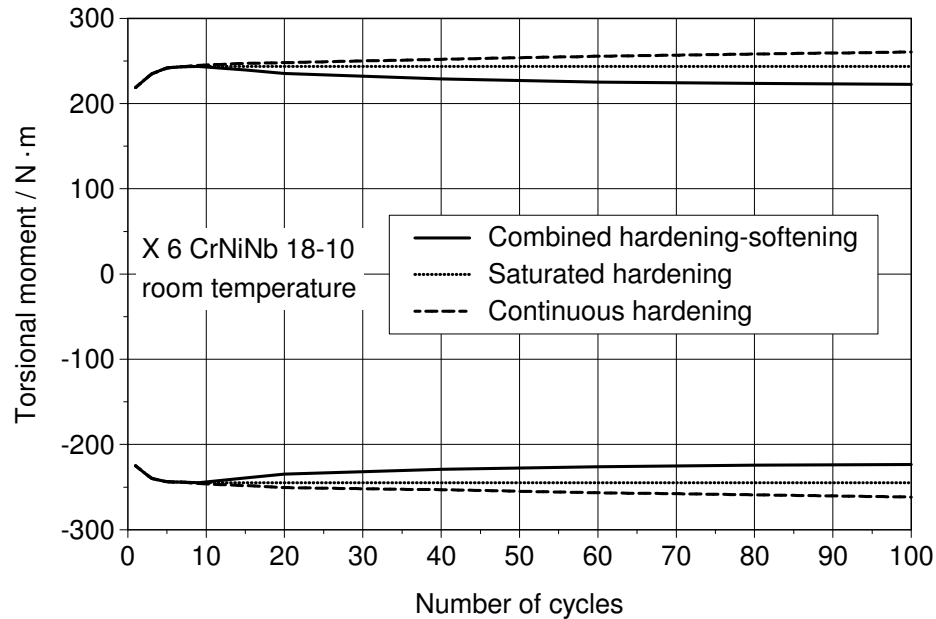
Figure 7.3: Calculated cyclic hardening/softening by applying different isotropic hardening models.

As shown in figure 7.3, the FE calculations were performed by using three different isotropic hardening approaches (equation 3.26, equation 3.27 and equation 3.29), respectively. In the beginning, all three curves present cyclic hardening in maximum and minimum torsional moments. Successively, the curves proceed differently regarding the application of different isotropic hardening approaches. By using the combined cyclic hardening-softening approach (equation 3.29), mixed cyclic hardening/softening behaviour is described. That is, after the cyclic hardening, a cyclic softening procedure arises. The cyclic softening proceeds in form of an exponential curve and reaches saturation after about 100 cycles. Furthermore, the cyclic hardening followed by a neutral behaviour is simulated by applying the saturated hardening approach (equation 3.27), and the cyclic hardening with a linear continuous increment is described by using the continuous cyclic hardening approach (equation 3.26). The shapes and magnitudes of cyclic hardening and softening as well as the gradient of the continuous cyclic harden-

ing curves depend on corresponding material parameters applied in isotropic hardening approaches.

The multiaxial ratchetting behaviour was investigated by performing FE analyses, in which displacement-controlled cyclic torsion and a constant axial load were applied simultaneously, so that the ratchetting strain can be accumulated in axial direction. The specification of the cyclic torsional load was identical with that in above pure torsional calculation, so that the amplitude of the cyclic torsional strain was kept to be 0.87%, and the equivalent strain $\dot{\varepsilon}_{eq}$ was 5×10^{-4} /s. The magnitude of the axial load prescribed in the FE calculations was 2.76KN, which yields 20 MPa on axial stress.
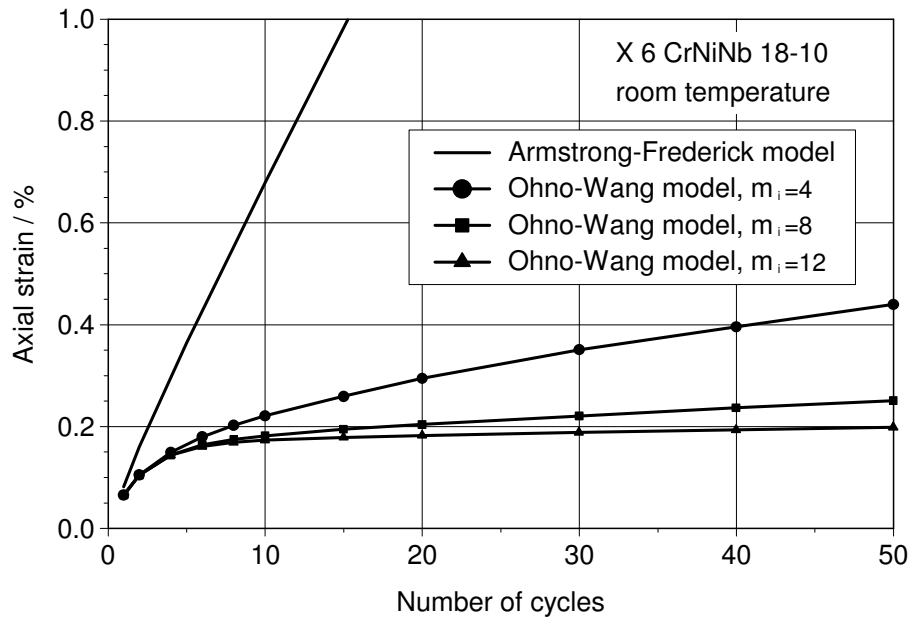
Figure 7.4: Calculated ratchetting strains against the number of cycles using Armstrong-Frederick approach (equation 3.11) and Ohno-Wang approach II (equation 3.18).

In figure 7.4, the ratchetting strain is calculated by using Armstrong-Frederick approach and Ohno-Wang approach II. As discussed in chapter 2.7.2, since the ratchetting strain is presented in form of accumulation of axial strain in multiaxial stress state, it can be called multiaxial ratchetting. As shown by the ratchetting strain curves in the figure, the ratchetting strain was accumulated with the increase of load cycles. Armstrong-Frederick approach predicts a quasi linear accumulation with a steep gradient, in which the procedure of transient ratchetting is almost not noticeable, whereas the

ratchetting calculated by Ohno-Wang approach II is much lower and can be clearly divided into transient ratchetting and asymptotic ratchetting.

As discussed in chapter 3, the material parameter m_i is used in Ohno-Wang approach II to diminish the overestimation of ratchetting strain, because the change of the value m_i, modifies the effect of dynamic recovery. The material parameter m_i is an integer, which is greater than zero. In this FE analyses, different values of m_i were applied for Ohno-Wang approach II, so that the influence of the material parameter m_i on the magnitude of multiaxial ratchetting can be investigated.

The results of the FE calculations are illustrated in figures 7.4 and 7.5. As shown in figure 7.4, the ratchetting curves calculated by using Ohno-Wang approach II shows that the shape of transient ratchetting and the gradient of asymptotic ratchetting are greatly influenced by the material parameter m_i. A larger m_i leads to smaller amount of transient ratchetting and lower gradient of asymptotic ratchetting. In addition, the increase of m_i is not proportional to the decrease of multiaxial ratchetting stain. As shown in figure 7.4, the decrement of ratchetting stain corresponding to an increment of m_i from 4 to 8 is much greater than that corresponding to an increment of m_i from 8 to 12.
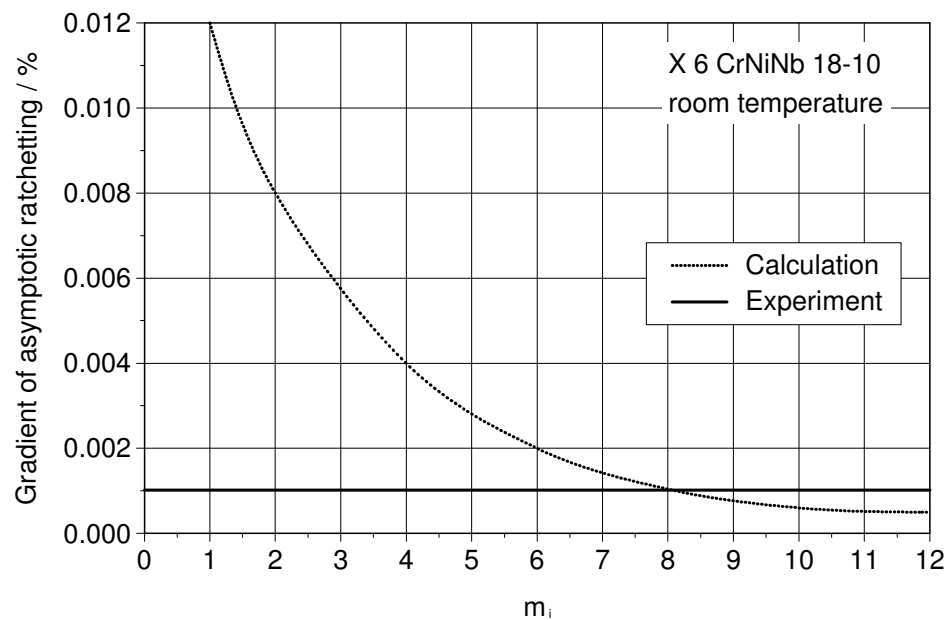

Figure 7.5: Dependence of multiaxial asymptotic ratchetting on parameter m_i.

As presented in figure 7.5, different FE calculations were performed by using a series of m_i. The gradients of asymptotic ratchetting corresponding to different values of m_i are illustrated in the figure the dotted curve. Asymptotic ratchetting has been introduced in chapter 2.7, while the gradient of asymptotic ratchetting is the slope of the ratchetting curve after linear increment of asymptotic ratchetting is achieved. Regarding the investigation presented by figured 7.4, it was determined by the gradient of ratchetting curve after 40 cycles. It can be seen that with the increase of the value of m_i, the gradient of asymptotic ratchetting drops rapidly. When m_i is greater than 10, the decrease of gradient is minor. The straight line in the figure shows the experimental result from corresponding component test, which was presented in figure 6.4 (accumulated multiaxial ratchetting strain at the end of step one) of chapter 6.1.1. It can be found that $m_i=8$ gives the best prediction for asymptotic ratchetting. The result accords with the results of parameter fitting presented in table 5.1 of chapter 5.6.1, in which the fitted parameter m_i equals 8. This accordance proves that the fitted parameter using uniaxial test is able to predict the gradient of multiaxial asymptotic ratchetting accurately.
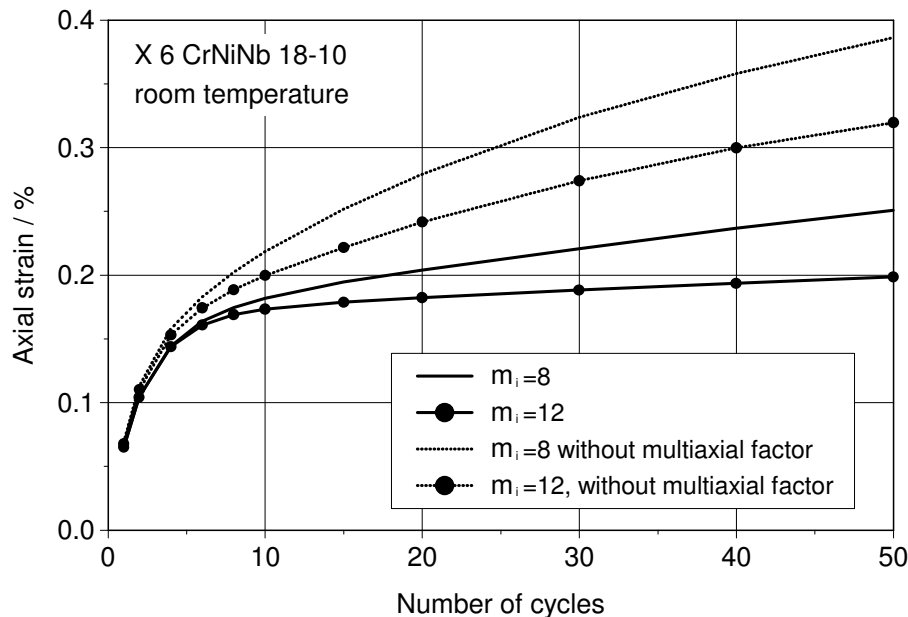

Figure 7.6: Influence of the multiaxial factor on the calculated multiaxial ratchetting.

As mentioned in chapter 2, in multiaxial stress-state, the magnitude of ratchetting under multiaxial loading is less than that under equivalent uniaxial loading. This multiaxial ratchetting effect can be simulated by involving a multiaxial factor like in Ohno-Wang

approach II (equation 3.18), in which the term $\langle \underline{n} : \underline{k}_i \rangle$ is considered as the multiaxial factor. It records the angle between the directions of inelastic strain-rate and back-stress. Since $\langle \underline{n} : \underline{k}_i \rangle \le 1$ under multiaxial nonproportional cyclic loading, it makes the dynamic recovery of back-stress less active, so that a less accumulation of multiaxial ratchetting strain can be simulated. Figure 7.6 illustrates the influence of the multiaxial factor $\langle \underline{n} : \underline{k}_i \rangle$ to multiaxial ratchetting strain. The solid curves depict the calculated ratchetting strains with the application of the multiaxial factor $\langle \underline{n} : \underline{k}_i \rangle$ and material parameter $m_i=8$ and $m_i=12$ respectively, while the dotted lines describe the corresponding calculated ratchetting curves without applying the multiaxial factor $\langle \underline{n} : \underline{k}_i \rangle$. The decrement of ratchetting due to the application of the multiaxial factor $\langle \underline{n} : \underline{k}_i \rangle$ depends on the nonproportionality of the multiaxial loading. In multiaxial ratchetting, the nonproportionality depends on the magnitude of the primary load. Regarding applied loading in this calculation, the nonproportionality depends on the magnitude of the axial load. That is, the larger the axial load, the more significant the nonproportionality.
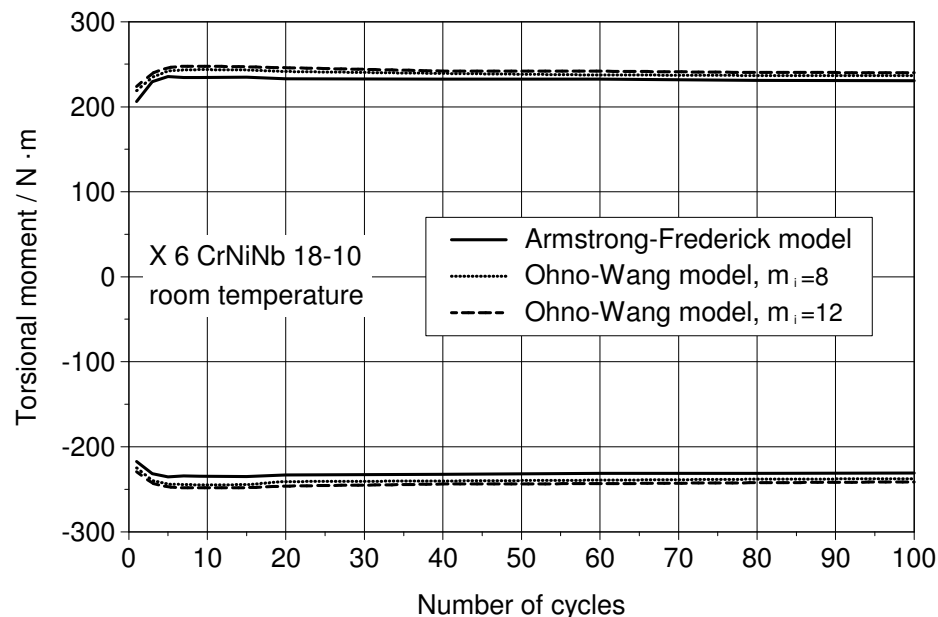

Figure 7.7: Calculated torsional moment with respect to the number of cycles by using different kinematic hardening models.

Figure 7.7 illustrates the calculated cyclic hardening/softening curves regarding the multiaxial ratchetting FE calculations by using Armstrong-Frederick approach and Ohno-Wang approach II with two different parameter m_i. It can be seen, that although the curves of the maximum and minimum torsional moments at loading reverse points with respect to the number of cycles proceed very close and parallel to each other, small differences between amplitudes of torsional moments of different curves still can be observed. The Armstrong-Frederick approach predicts the most conservative magnitude. Ohno-Wang approach II with $m_i=8$ present larger amplitude of torsional moment, so that it's curve locates above the curve of Amstrong-Frederick approach. If m_i is increased to 12, the amplitude of torsional moment increases only slightly, so that the difference between curves of $m_i=8$ and $m_i=12$ is very insignificant. The reason can be summarized as following:
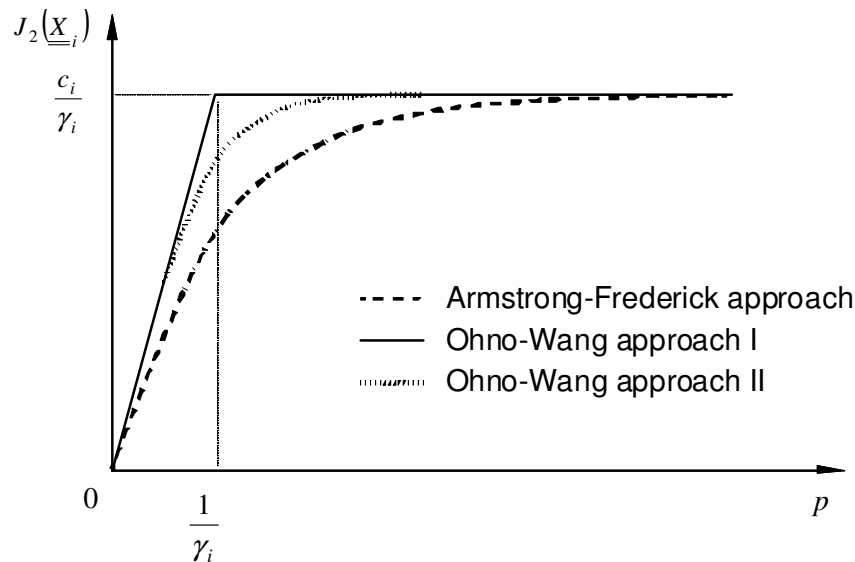
Figure 7.8: Change of $J_2(\underline{\underline{X}}_i)$ by using different kinematic hardening models.

As discussed in chapter 3, Armstrong-Frederick model is an extreme case of Ohno-Wang approach II, when the material parameter m_i equals zero. Additionally, the Ohno-Wang approach I (equation 3.17) is another extreme case of the approach II, when m_i tends to infinite. Figure 7.8 illustrates the course of the second invariant of back-stress $J_2(\underline{\underline{X}}_i)$ depending on application of different kinematic hardening approaches. Armstrong-Frederick approach describes the relationship between $J_2(\underline{\underline{X}}_i)$ and the accumulated plastic strain p in an exponential curve, while the Ohno-Wang approach I gives a bilinear curve, which is the asymptotic lines of the exponential

curve calculated by Armstrong-Frederick approach. The curve of Ohno-Wang approach II locates between the exponential curve from Armstrong-Frederick approach and the bilinear curve from Ohno-Wang approach I. If $m_i=0$, the curve of Ohno-Wang approach II is identical to the curve of Armstrong-Frederick approach. With the increase of m_i, the curve of Ohno-Wang approach II moves towards the bilinear curve of Ohno-Wang approach I. When the value m_i is large enough, the curve of Ohno-Wang approach II superposes with the bilinear curve. Before the saturations in curves of Armstrong-Frederick approach and Ohno-Wang approach II are reached, there are always deflections between theses three curves, and these deflections in back-stresses lead to different amplitudes in cyclic hardening/softening curves shown in figure 7.7.
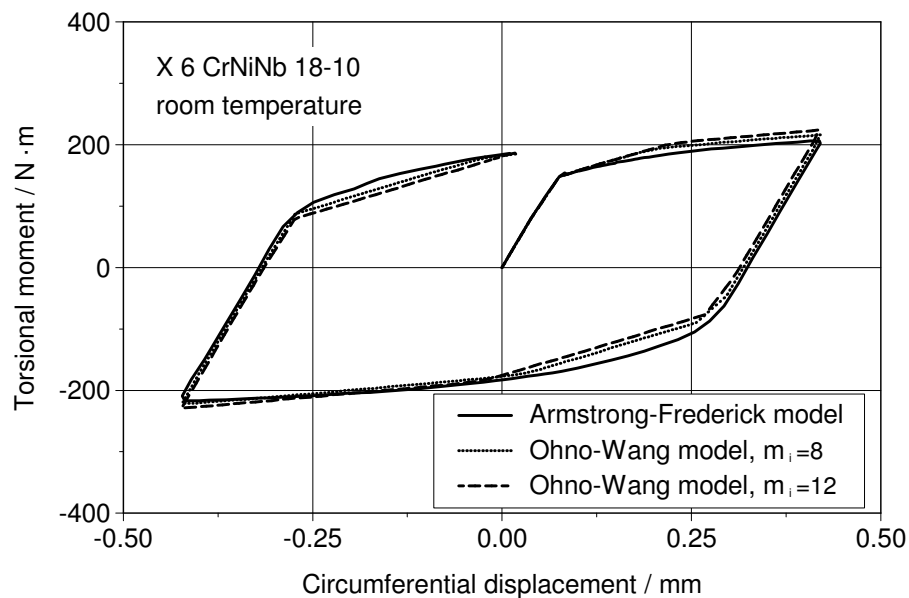
Figure 7.9: Calculated the first hysteresis loops by using different kinematic hardening approaches.

The calculated hysteresis loops concerning the first load cycle by using Armstrong-Frederick approach and Ohno-Wang approach II with different values of parameter m_i are demonstrated in figure 7.9. As discussed above, Ohno-Wang approach I presents a bilinear curve for the back-stress. Since four back-stresses were applied in the unified viscoplastic Chaboche model in this work, the calculated hysteresis loop by using Ohno-Wang approach I is a superposition of four different bilinear curves, which is a polygonal line, as shown in figure 3.2(a). As discussed above, if the parameter m_i in Ohno-Wang approach II is large, the back-stress curve calculated by Ohno-Wang ap-

proach II will be very close to the curve calculated by Ohno-Wang approach I, therefore in figure 7.9, the hysteresis loops calculated by Ohno-Wang approach II with material parameters m_i=8 and m_i=12 are composed of a series of polygonal lines, while the hysteresis loop calculated by Armstrong-Frederick approach is composed of a series of exponential curves.

7.2.2 Qualitative investigation of the material model for multiaxial nonproportional cyclic loading

For investigating the functionality of the viscoplastic Chaboche model in predicting the effect of multiaxial nonproportional cyclic loading, a series of FE calculations were performed by using different strain-controlled load-paths. First of all, five strain-paths were defined as shown in figure 7.10, in which cyclic axial load and cyclic torsional load are applied separately or simultaneously. Path 1 and Path 2 depict cyclic axial tension-compression and cyclic torsion, respectively. Path 3 describes a multiaxial cyclic in-phase loading, in which cyclic axial tension-compression and cyclic torsion is in-phase applied. Path 4 is a kind of out-of-phase test, in which cyclic tension-compression and cyclic torsion have a phase-lag of a quarter of a period $\pi/2$. In path 5, the cyclic tension-compression and cyclic torsion are defined as sinus and cosine functions, respectively, so that the strain-path proceeds along a circle.

Path1: Tension-Compression   Path2: Torsion   Path3: Tension+Torsion
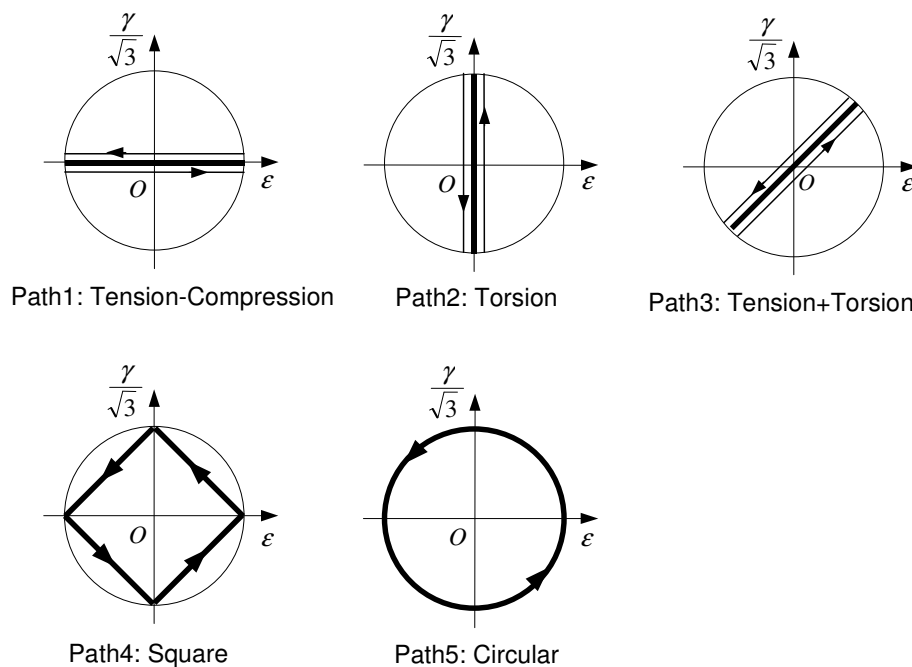
Path4: Square   Path5: Circular

Figure 7.10: Illustration of different cyclic strain paths.

For the equivalence between the axial and torsional loading conditions, Von-Mises criterion was considered. Consequently, the equivalence for the cases of strain-controlled tension and torsion can be approximated by:

$$\Delta\varepsilon_{eq} = \frac{\Delta\gamma}{\sqrt{3}} = \Delta\varepsilon ,\qquad(7.1)$$

where $\Delta\varepsilon_{eq}$ is the range of equivalent strain, and $\Delta\varepsilon$ and $\Delta\gamma$ represent the axial strain-range and shear strain-range, respectively. In above five load-paths, the ranges of strain components in axial direction and circumferential direction correspond to an identical range of equivalent strain. Therefore the five paths can be illustrated with the help of a circle, whose radius is the amplitude of the equivalent strain, as shown in figure 7.10.

As discussed in chapter 3.3.4, chapter 6.1.2 and chapter 6.2.2, an additional cyclic hardening can be evoked due to the attendance of multiaxial nonproportional cyclic loading. The Krämer-Krolop approach (equation 3.23 and 3.25) provides the possibility to simulate the effect of nonproportional cyclic loading. In this work, a simplified Krämer-Krolop approach was applied:

$$\underline{\dot{X}} = \frac{2}{3}c\underline{\dot{\varepsilon}}_p - \gamma(1-\gamma'(1-e^{-p^*}))\underline{X}\dot{p} ,\qquad(7.2)$$

$$\dot{p}^* = c''\left|\sin\varphi\right|\dot{p} ,\qquad(7.3)$$

$$\text{with } \varphi := \arccos\left[\frac{\underline{\dot{\varepsilon}}_p : \underline{\varepsilon}_p}{\left\|\underline{\dot{\varepsilon}}_p\right\|\left\|\underline{\varepsilon}_p\right\|}\right].$$

where γ' is a material parameter ranging from 0 to 1, and c'' is greater than 0. Since the five load-paths defined above show very simple shapes, it's not necessary to take into account the curvature of the strain-paths κ in equation 3.23. Namely, the factor φ, which records the angle between the viscoplastic strain tensor and viscoplastic strain-rate tensor, alone is able to describe the effect of nonproportional cyclic loading. Due to above reason, equation 3.23 was simplified to equation 7.3. Since so far no experiments were performed for the determination of the parameters used in this

model, the trial values, $c'' = 4.0$ and $\gamma' = 0.8$, were applied in the FE analyses for the qualitative investigation of the approach.
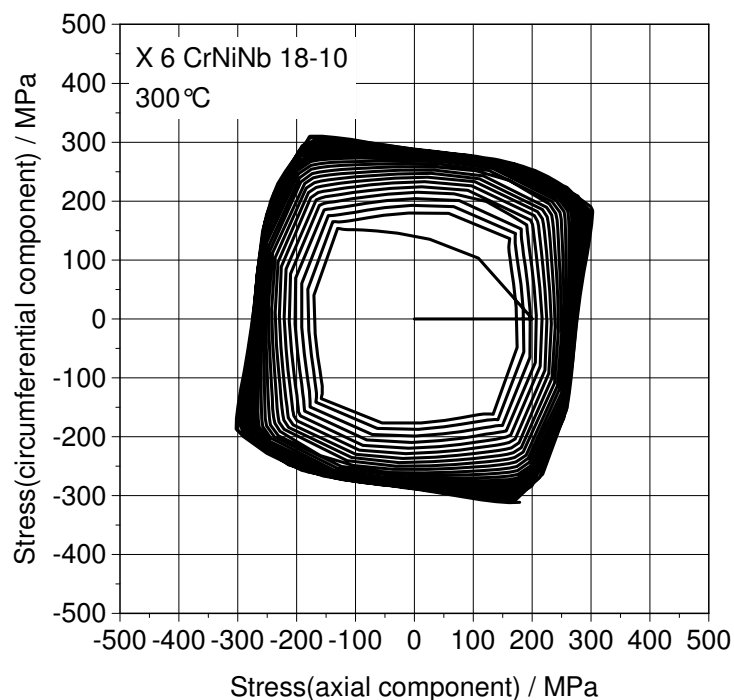
Figure 7.11: Calculated stress-path according to the square strain-path.
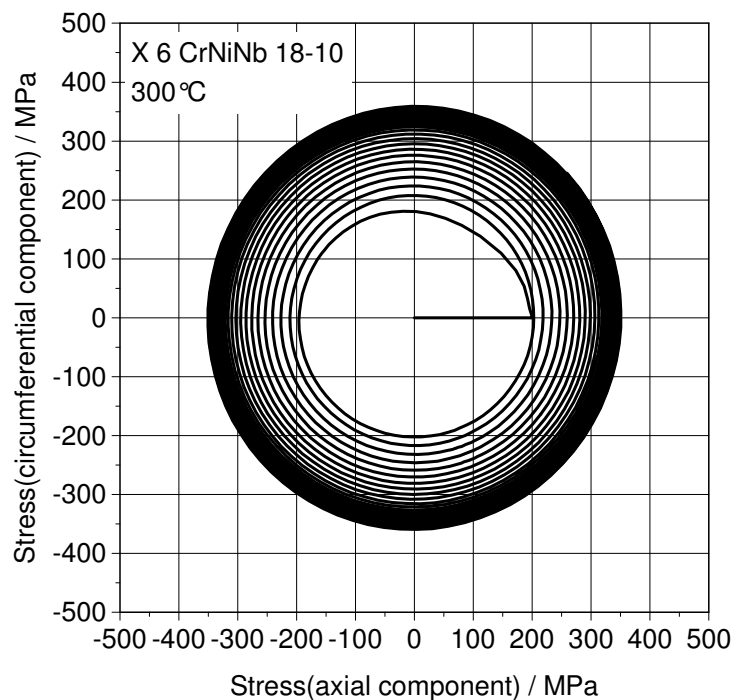
Figure 7.12: Calculated stress-path according to the circular strain-path.

In FE calculations by using the five load-paths, the amplitude of equivalent strain was prescribed to $\dfrac{\Delta\varepsilon_{eq}}{2} = 0.5\%$. Figures 7.11 and 7.12 demonstrate the calculated stress-paths corresponding to the path 4 and path 5. It can be seen, that the stress-paths follow the basic shapes of strain-paths, and cyclic hardening can be shown clearly by the tracks of stress-paths in both figures. The magnitudes of cyclic hardening and the rotation of the stress-paths regarding the square load-path as shown in figure 7.11 depend on the values of material parameter c'' and γ'.
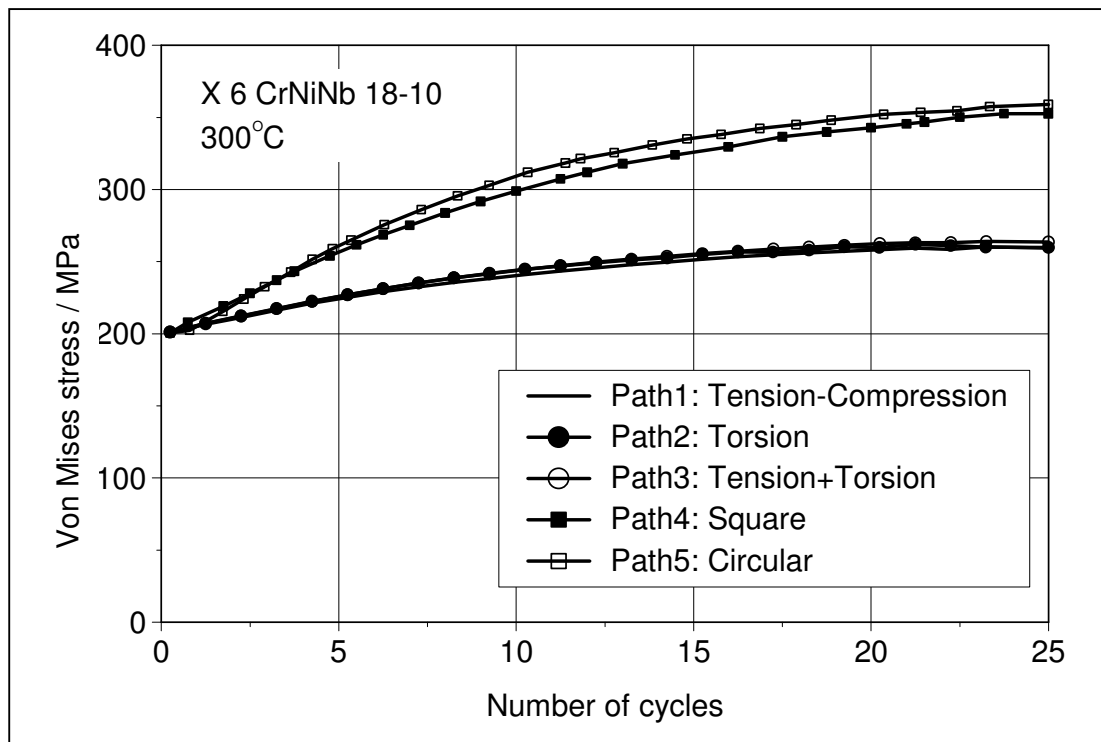
Figure 7.13: Influence of the shapes of strain-paths on cyclic hardening behaviour.

Calculated von Mises stresses regarding the five strain-paths with respect to the number of cycles are illustrated in figure 7.13. One essential feature abstracted from the figure is the clear dependence of the cyclic hardening on the shape of strain-path. As shown in the figure, every curve starts with the identical magnitudes in the incipient stage. With the increase of loading cycles, the identical cyclic hardenings regarding the uniaxial tension-compression, pure torsion and superposition of tension and torsion (tension + torsion) load-paths are achieved. Cyclic hardenings calculated based on the square and circular load-paths are significantly larger. Furthermore the largest

cyclic hardening is attained by the circular path, which is slightly larger than that achieved by the square path. The reason of these results can be summarized as following.

The angle φ between viscoplastic strain tensor and viscoplastic strain-rate tensor is always 0° or 180° under proportional cyclic loading, path 1, 2 and 3, therefore the internal variable p^* doesn't influence the dynamic recovery term of the kinematic hardening model. Whereas under nonproportional cyclic loading the angle φ is nonzero values, so that p^* influences the dynamic recovery term. Regarding the circular load-path, the angle φ is always 90°, so that the largest nonproportional effect is obtained in the circular load-path, which leads to the most significant cyclic hardening.

7.3   Comparison between experiments and FE calculations

7.3.1   Comparison for the austenitic material

In chapter 7.2, the material models for simulating multiaxial ratchetting and the effect of multiaxial nonproportional cyclic loading were qualitatively investigated via FE analyses. In order to verify the material models quantitatively, a series of FE analyses corresponding to the component tests, which have been introduced chapter 6, were performed. The calculation results are compared with the experimental results in this chapter.

For the comparison to the multiaxial ratchetting component test in chapter 6.1.1, figure 6.3 and figure 6.4, the FE calculations were performed, and results are illustrated in figure 7.14 and figure 7.15. Calculation1 corresponded to a FE analysis implemented by using viscoplastic Chaboche model with integrated Ohno-Wang approach II and combined cyclic hardening/softening approach and evolution equations of strain-memory-effect as well as fitted parameters in table 5.1. Calculation2 was performed by using the same material model and a refitted value for the parameter c_4. The c_4 was refitted by specifying a higher priority for the uniaxial ratchetting test during the material fitting procedure.

Figure 7.14 shows the comparison between the measurement (figure 6.4) and calculated multiaxial ratchetting strains. In the first 100 cycles, the multiaxial ratchetting curve of calculation1 shows good consistency to the experimental results regarding asymptotic ratchetting, so that the calculated ratchetting curve (dotted curve) proceeds parallel to the experimental multiaxial ratchetting curve after 20 cycles. Nevertheless the transient ratchetting in the fist 20 cycles is overestimated. The deflection between experiment and calculation1 due to the overestimation of transient ratchetting is about 0.08%. For improving the prediction for transient ratchetting, calculation2 was performed by using a refitted parameter c_4=12000. The c_4 was achieved by specifying that the uniaxial ratchetting test has a higher priority than the strain-controlled cyclic tension-compression test during the parameter fitting, so that the fitted parameters prefer to close the error to the uniaxial ratchetting first. As shown in the figure, the ratchetting curve of calculation2 (dashed curve) presents very good agreements to the experiment not only for asymptotic ratchetting but also for transient ratchetting.

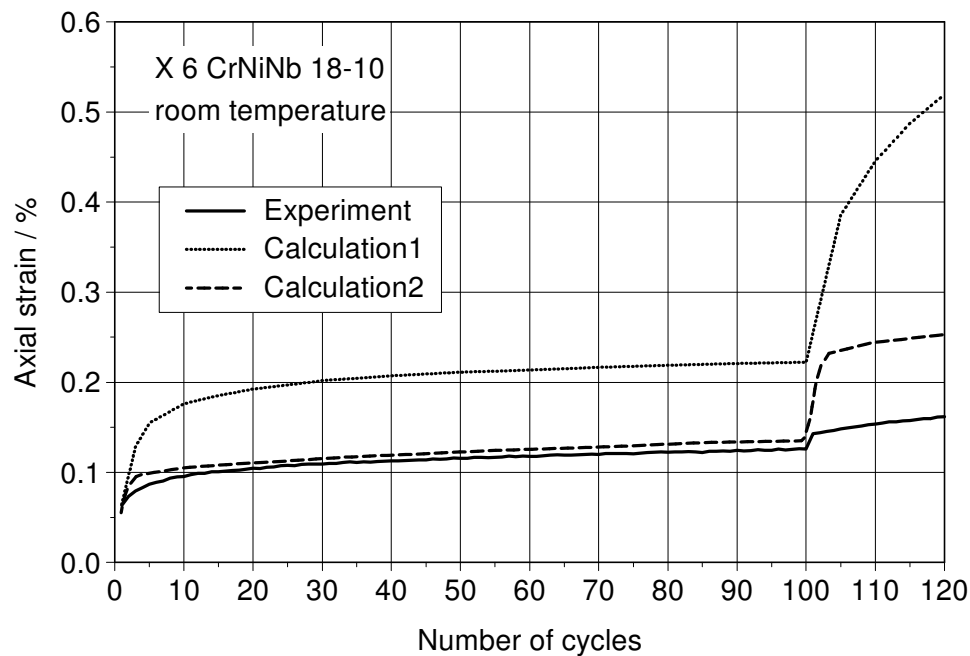Figure 7.14: Comparison between measurement (figure 6.4) and calculated ratchetting strains for the austenitic material at room temperature

In the second step, after 100 cycles, the axial load (primary load) was doubled, the calculations predict much larger transient ratchetting compared to measurements. This deflection between experiment and calculations can be attributed to a characteristic of

multiaxial ratchetting: As discussed in previous chapters, the material parameters were fitted based on the uniaxial test results. As shown in figure 5.6, while the mean-stress increases from 20 MPa to 40 MPa, a pronounced transient ratchetting strain is evoked. Nevertheless it is not the case for multiaxial ratchetting. In multiaxial stress-state, a doubled primary stress induced only a slight increment of transient ratchetting strain as shown in figure 7.14. Namely, the same increment of primary stress (mean-stress for uniaxial ratchetting) yields different transient ratchetting increments in uniaxial ratchetting and multiaxial ratchetting in multiple step uniaxial and multiaxial ratchetting tests.

Via analysing the measurement and calculation results regarding uniaxial and multiaxial ratchetting, it can be summarized that the multiaxial ratchetting behaviour differs from the uniaxial ratchetting behaviour regarding a comparable increase of primary load in multiple step ratchetting test. The Ohno-Wang approach II can very good predict the uniaxial ratchetting in multiple step test, as shown in figure 5.6, and multiaxial ratchetting in single step test, as shown the first 100 cycles in figure 7.14. For better simulating the magnitude of the increase of multiaxial transient ratchetting in multiple tests, the applied Ohno-Wang approach II should be improved, so that the ratio between increments of transient ratchetting in uniaxial and multiaxial ratchetting tests can be taken into account.

For comparing the strain hardening and cyclic hardening behaviour between component test and FE calculation, the results of the maximum and minimum torsional moments against the number of cycles for the same multiaxial ratcheting test are illustrated in figure 7.15. As mentioned above Ohno-Wang approach II was applied with fitted material parameters In the calculation1. Very good agreement between experiment and calculation is shown in the figure: The calculated curves for torsional moment show incipient cyclic hardening and subsequent quasi-neutral cyclic behaviour. The increase of axial load after 100 cycles does not influence the continuity of cyclic behaviour. The quasi-neutral behaviour can be attributed to smaller values of material parameters, b (equation 3.29), Q_{max} and Q_o (equation 3.36), which were fitted based on the uniaxial tests. A smaller value of the parameter b gives a slower decrease of cyclic hardening, while a less difference between Q_{max} and Q_o yields an insignificant magnitude of cyclic softening. By using refitted parameter $c_4=12000$, calculation 2 presents similar cyclic hardening and softening behaviour. Nevertheless, as mentioned

above, since during parameter refitting, the uniaxial ratchetting test is specified to have a higher priority than the strain-controlled uniaxial tension-compression test in order to get better fitting results for ratchetting behaviour, compensation has to be made regarding the strain hardening behaviour. Consequently calulation2 simulates larger torsional moments compared to experimental results and calculation1.
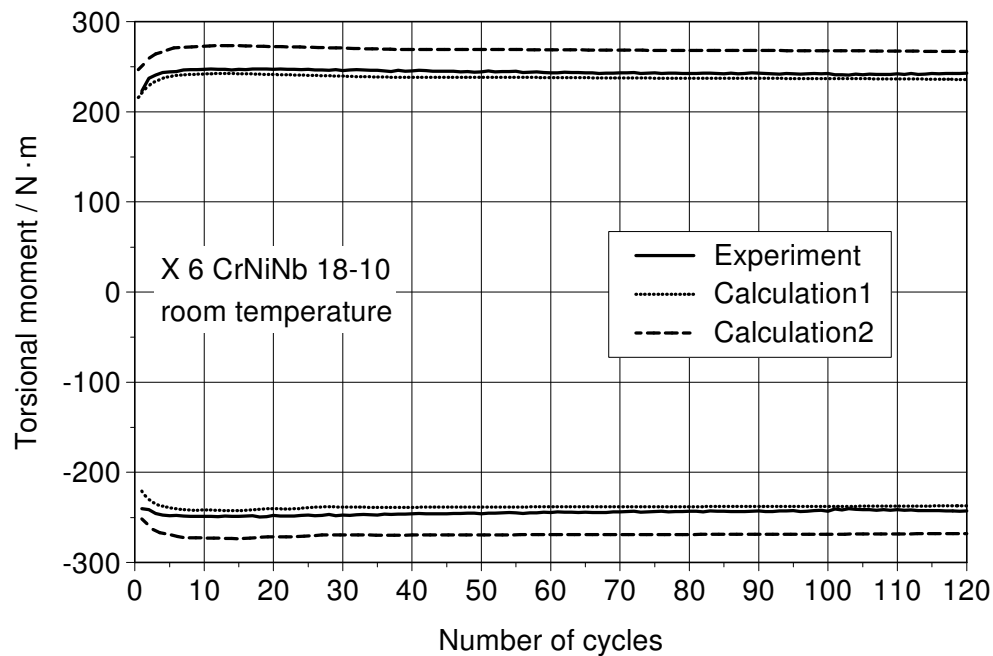
Figure 7.15: Comparison between measured and calculated torsional moments for the austenitic material at room temperature.

For comparing the results between component test and FE calculation for the austenitic material at $300°C$, the FE calculations were performed regarding the multiaxial ratchetting test introduced in chapter 6.1.1 (figure 6.5 and 6.6). The viscoplastic Chaboche model with integrated Ohno-Wang approach II for kinematic hardening, combined cyclic hardening-softening approach for isotropic hardening and evolution equations of strain-memory-effect was applied in FE calculation. The fitted parameters in table 5.2 are used in the viscoplastic Chaboche model. The comparison results are illustrated in figures 7.16 and 7.17.
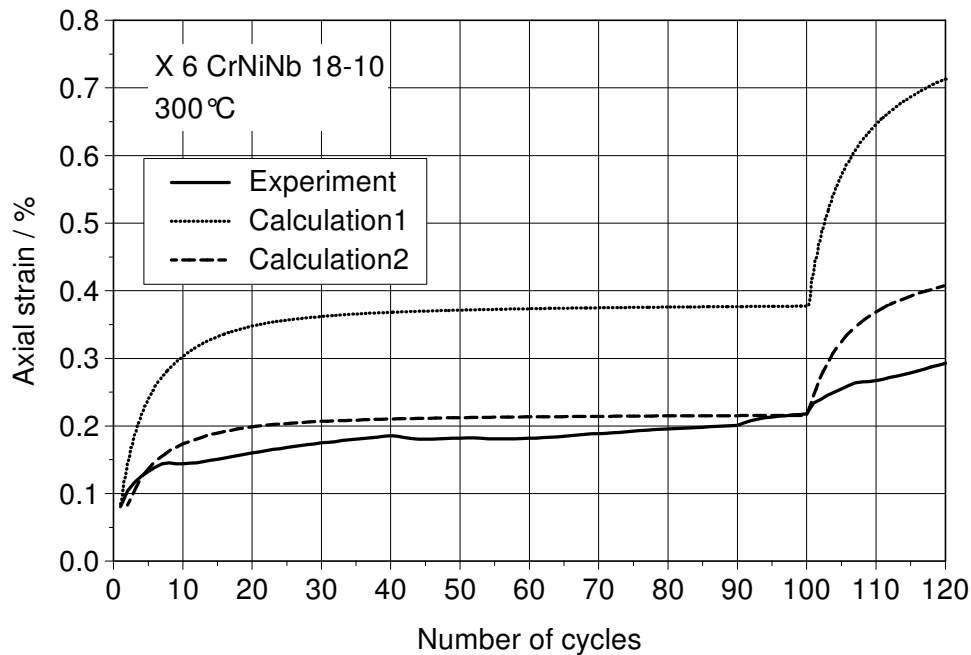
Figure 7.16: Comparison between measured and calculated ratchetting strains for the austenitic material at 300°C.

Figure 7.16 shows multiaxial ratchetting curves regarding the experimental results and calculation results. By using the fitted parameters, good agreement between experiment and calculation1 for the asymptotic ratchetting is presented in the first step, so that the curve of calculation1 precedes parallel to the experimental curve from 30 to 100 cycles. Nevertheless the transient ratchetting in the first 30 cycles is overestimated. By specifying the higher priority of the uniaxial ratchetting test in parameter fitting procedure, a refitted parameter $c_4=7000$ was got, by which the overestimation for the transient ratchetting can be eliminated in calculation2. Identical to the results for the austenitic material at room temperature, the calculated ratchetting strain at 300°C is overestimated in the second step by both calculation1 and calculation2. The reason is the same as discussed above: Since the increase of transient ratchetting strain in multiple uniaxial ratchetting and multiple multiaxial ratchetting tests are quite different, for better simulating the multiaxial ratchetting strain in multiple step test, the applied kinematic hardening approach, Ohno-Wang approach II, should be improved to take into account this difference between uniaxial ratchetting and multiaxial ratchetting behaviour.
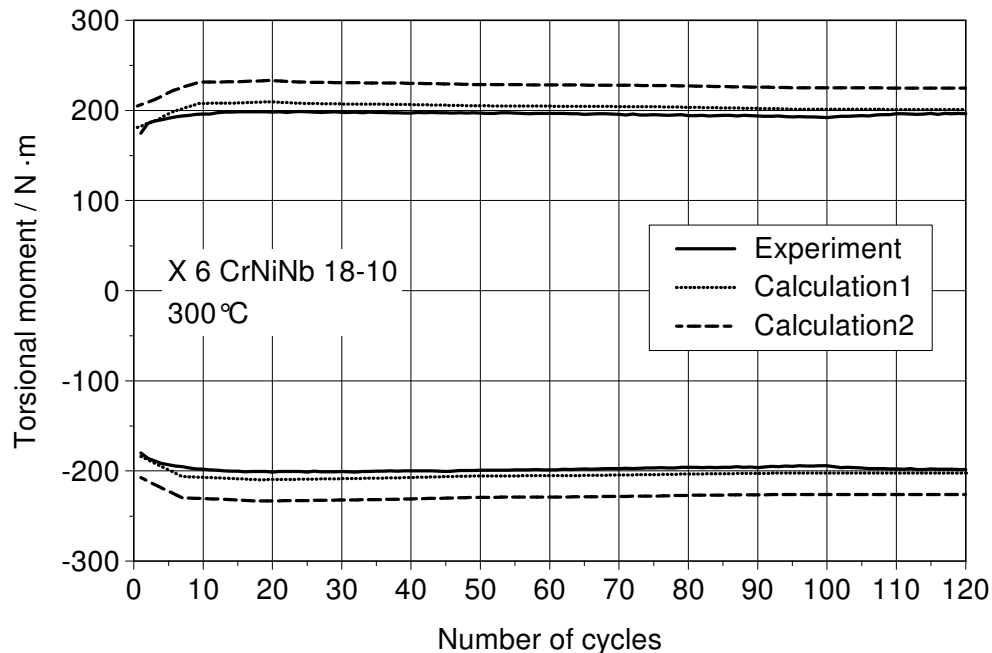
Figure 7.17: Comparison between measured and calculated torsional moments for the austenitic material at 300° C.

Figure 7.17 shows the maximum and minimum values of measured and calculated torsional moments with respect to the number of cycles regarding the multiaxial ratchetting test for the austenitic material at 300°C. As seen in the figure, good agreement between experiment and calculation1 can be achieved. Compared to the results at room temperature, the cyclic hardening curve at 300°C presents a less gradient, which was due to a smaller value for the parameter a (equation 3.29). The magnitude of hardening depends on the parameter c (equation 3.29), Q_{max} and Q_o (equation 3.36). In addition, calculation2 presents similar cyclic hardening and softening behaviour, nevertheless the range of torsional moment is overestimated since the strain-hardening is influenced by the refitted parameter c_4. As discussed for the multiaxial ratchetting test for the austenitic material at room temperature, since the high priority was specified for the uniaxial ratchetting test in the parameter fitting, the fitted parameters are preferred to provide better fitting results for ratchetting. As compensation, the results regarding hardening simulation was correspondingly slightly degraded.

Based on above results, it can be found that the predictions of hardening and ratchetting are two different applications, which should be incorporated in the viscoplastic Chaboche model. In the frame of this work, both hardening and ratchetting behaviour

should be simulated by using the kinematic hardening approach, Ohno-Wang approach II. That means the parameters should be properly determined, so that the Ohno-Wang approach II can accurately describe both material behaviour. Nevertheless, the experience showed that it was very difficult to find appropriate parameters, which presented accurate predictions for hardening and ratchetting simultaneously. Therefore the parameters should be fitted either moderately for achieving acceptable results for both ratchetting and hardening at the same time, or inclining to certain behaviour by predefining higher privilege for it. For instance, if ratchetting is more of interest, the higher weighting factor should be given to ratchetting tests in the procedure of parameter fitting. The consequence of it is that the accuracy of the simulation for hardening can be slightly degraded.

For verifying the effect of multiaxial nonproportional cyclic loading, the FE calculations were performed for the in-phase-test and out-of-phase-test introduced in chapter 6.1.2. In the applied viscoplastic Chaboche model, Krämer-Krolop approach was used instead of Ohno-Wang approach II for the kinematic hardening. As shown by the experimental results of the in-phase- and out-of-phase-tests, the additional hardening was evoked in the out-of-phase test. It should be emphasize that although the path 3 and path 4 in chapter 7.2.2 (figure 7.10) are a kind of in-phase-test and out-of-phase test, respectively, they were defined in different way from the in-phase- and out-of-phase-tests mentioned in chapter 6.1.2. Path 3 and path 4 were defined by applying the same equivalent strain-ranges in both loading directions, namely the strain-ranges in torsion and axial direction corresponded to the same equivalent strain-range. Whereas in the performed component tests in chapter 6.1.2, due to the limitation of testing conditions, the equivalent strain-range applied in axial direction was much less than that applied in torsional direction:

As mentioned in chapter 6, component was fastened by two cylindrical clamping blocks on the testing rig, and the axial loading was transferred to the shoulders of components via the friction force between the clamping blocks and the component shoulders. If the applied axial load is too large, so that it exceeds the friction force, relative sliding between clamping blocks and component will take place in axial direction. To avoid the relative sliding, the axial load could not be defined too large. Since the axial strain-range was much less than the equivalent strain-range in torsion in the

component tests, the nonproportionality in the out-of-phase-tests is smaller than that defined in load-path 4.

As discussed in chapter 7.2.2, the application of Krämer-Krolop kinematic hardening approach provides the possibility to simulate the additional hardening evoked by the multiaxial nonproportional cyclic loading. Nevertheless how to fit the additional material parameters c'' and γ', defined in Krämer-Krolop approach, is a difficulty, because for fitting multiaxial nonproportional cyclic behaviour, the whole parameter fitting procedure with the optimization program MINUIT has to be extended from one-dimensional to three-dimensional. That is, on the one hand, for fitting the material parameters, which takes into account the effect of multiaxial nonproportional cyclic loading, multiaxial nonproportional cyclic tests should be performed beside uniaxial tests; on the other hand, the one-dimensional constitutive equations constructed in the optimization program MINUIT should be updated to three-dimensional. Since this complicated fitting procedure is not included in the frame of this work, only two trial values of parameters $c'' = 4.0$ and $\gamma' = 0.8$ were applied in Krämer-Krolop approach. Since these two parameter values are just the estimations, the effect of multiaxial nonproportional cyclic loading can only be qualitatively investigated with them.
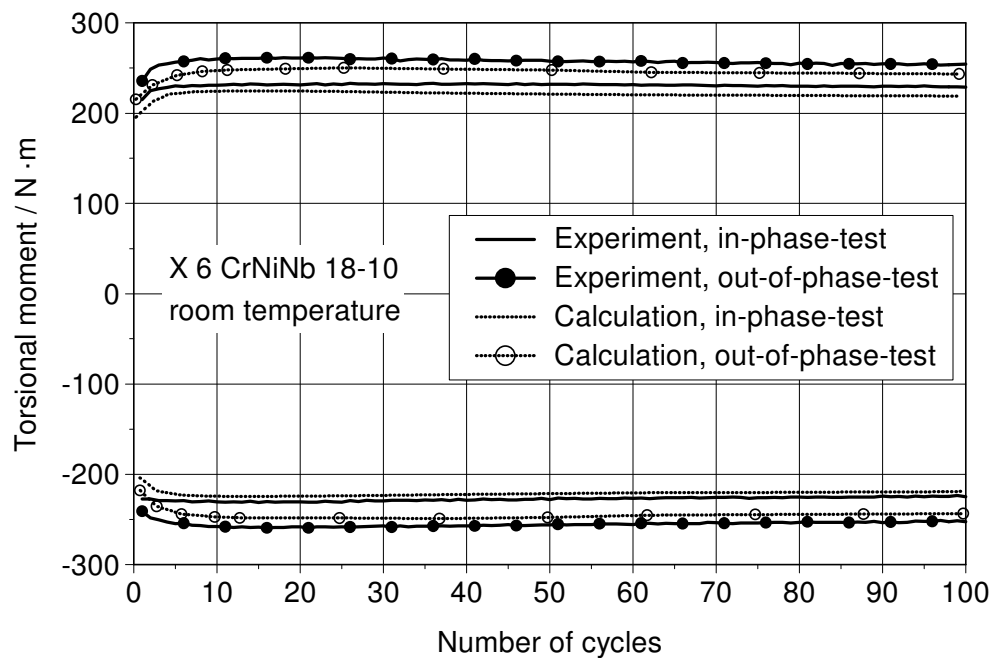
Figure 7.18: Comparison of measured and calculated torsional moments based on the in-phase- and out-of-phase-tests for the austenitic material at room temperature.
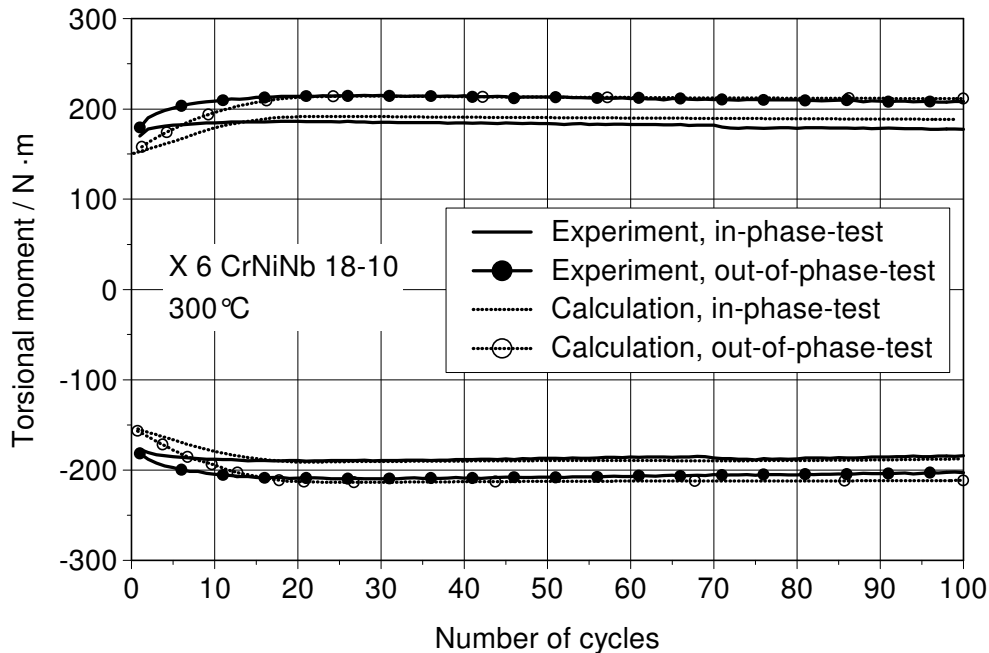
Figure 7.19: Comparison of measured and calculated torsional moments based on the in-phase- and out-of-phase-tests for the austenitic material at 300 °C.

Figures 7.18 and 7.19 illustrate the experimental and calculated maximum and minimum torsional moments with respect to load cycles based on the in-phase- and out-of-phase-tests for the austenitic material at room temperature and 300 °C, respectively. It can be found that, by using Krämer-Krolop approach, the additional hardening in out-of-phase-tests due to multiaxial nonproportional cyclic loading can be simulated by the viscoplastic Chaboche model. Since the values of the parameters c'' and γ' are estimated values, there exist deflections on the shape and magnitude of the cyclic hardening/softening curves. As discussed above, for the quantitative simulation of the nonproportional loading effect, the parameters applied in Krämer-Krolop model should be fitted by perform corresponding multiaxial tests.

7.3.2 Comparison for the ferritic material

In order to verify the viscoplastic Chaboche model for the multiaxial ratchetting test containing a relatively large primary stress, the multiaxial component ratchetting test, was performed with a primary stress, 108 MPa, for the ferritic material at room temperature as described in chapter 6.2.1 (figure 6.13 and figure 6.14). Corresponding FE calculation was carried out by using viscoplastic Chaboche model including Ohno-

Wang approach II for kinematic hardening, combined cyclic hardening/softening approach for isotropic hardening, and evolution equations for strain-memory-effect, as well as the fitted parameters in table 5.3. The comparisons between experiment and calculation are illustrated figures 7.20 and 7.21.
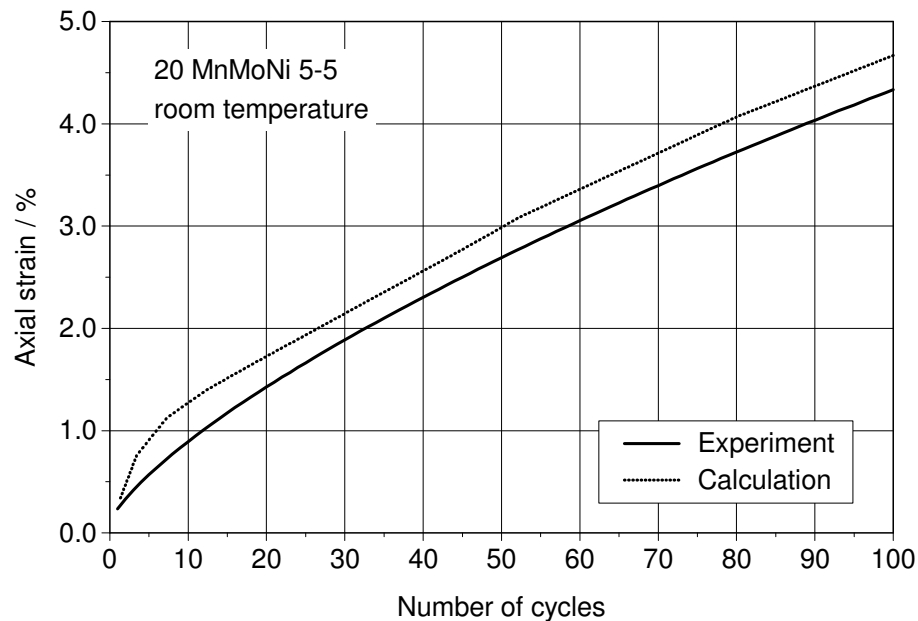
Figure 7.20: Comparison of measured and calculated multiaxial ratchetting curves for the ferritic material at room temperature.

The multiaxial ratchetting strains of experimental measurements and calculation results can be compared in figure 7.20: Under a higher primary stress, the gradient of asymptotic ratchetting is pronounced increased, so that the experimental ratchetting curve is dominated by the asymptotic ratchetting. Oppositely, based on experimental results for the austenitic material, it can be found that under restively small primary stress less than 40 MPa, multiaxial ratchetting is dominated by transient ratchetting. The FE calculation presents an accurate prediction for asymptotic ratchetting from cycle 10 to cycle 100, while the transient ratchetting in the first 10 cycles is overestimated. Nevertheless since the asymptotic ratchetting dominates the multiaxial ratchetting procedure, the error due to the overestimation of transient ratchetting is less than 7% after 100 cycles. Similar to the multiaxial simulations introduced in chapter 7.3.1 for the austenitic material, the overestimation of transient ratchetting can also be eliminated by using refitted parameter of c_i by means of specifying higher priority for uniaxial ratchetting test in parameter fitting, nevertheless the cost is that the strain-hardening

would be overestimated. Considering the fitted parameters in table 5.3 provide a good result regarding asymptotic ratchetting and the overestimation in transient ratchetting is less than 7% of the total ratchetting strain after 100 cycles. The calculation results can be regarded as a good prediction for multiaxial ratchetting under high primary stress.
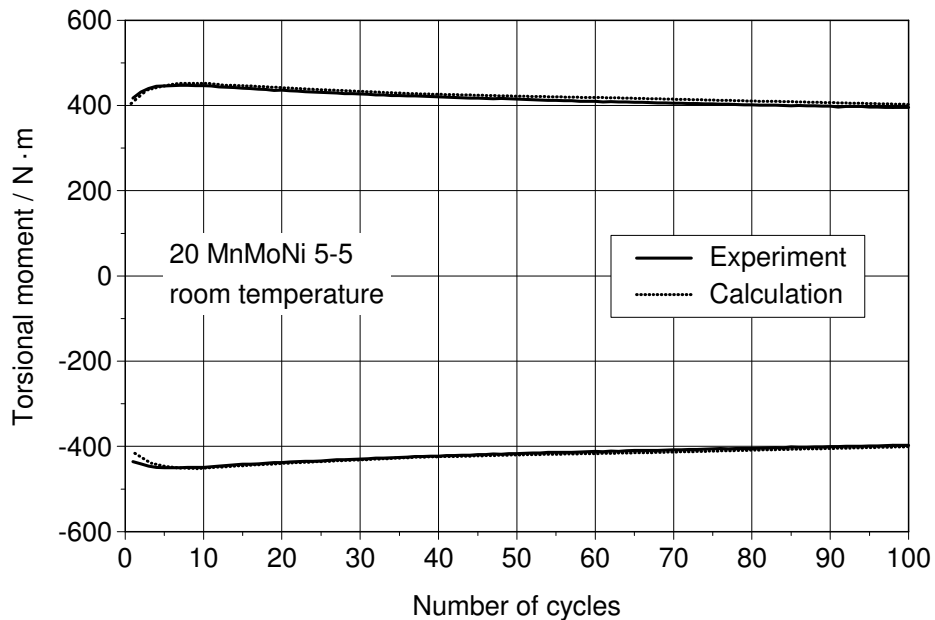
Figure 7.21: Comparison of measured and calculated torsional moments for the ferritic material at room temperature.

The measured and calculated maximum and minimum torsional moments with respect to load cycles are illustrated in figure 7.21. It can be seen that the incipient cyclic hardening and subsequent cyclic softening can be simulated very accurately by using the applied material model and fitted material parameters.

8 Discussion, conclusion and outlook

To describe viscoplastic material behaviour under cyclic loading, the viscoplastic Chaboche model was applied in the frame of this work. This model can be regarded as a unified model, because there is no separation between plastic strain and viscous strain. The model was extended based on the time-independent AFC model through the introduction of time-dependent effect by using viscous stress. The cyclic material behaviour was described by a series of internal variables in the model. The kinematic hardening variable, which is so-called back-stress, was used to describe the direction-dependent hardening, which is so-called strain-hardening. Different nonlinear kinematic hardening approaches were applied for the back-stress in this work, among which Armstrong-Frederick approach was applied as basic nonlinear kinematic hardening approach; Ohno-Wang approach II was applied especially for the prediction of ratchetting; Krämer-Krolop approach was used to take into account the effect of multiaxial nonproportional cyclic loading. Furthermore, four back-stresses were applied in the material model, so that the strain-hardening in a large strain-range can be accurately described. The direction-independent hardening/softening behaviour, which can be detected by means of cyclic hardening/softening, was described by using isotropic hardening variables. In this research work, different isotropic hardening approaches were developed and applied, through which saturated cyclic hardening, continuous cyclic hardening, pure cyclic softening and combined cyclic hardening/softening can be simulated. In addition, the evolution equations for describing strain-memory-effect were incorporated in the viscoplastic Chaboche model to take into account history of previous achieved maximum strain-range.

For investigating material behaviour and fitting parameters for the viscoplastic Chaboche model, uniaxial tests by using small specimens were performed for the selected materials. The austenitic material X6 CrNiNb 18-10 shows obvious nonlinear strain-hardening in tension and compression, whereas it doesn't show distinct yield limit under monotonic tension at room temperature and 300 °C. In uniaxial cyclic tests performed at room temperature, the austenitic material presents evident cyclic hardening in the beginning. After a certain number of cycles, it shows strain-range-dependent cyclic behaviour. Namely, when strain-range is low e.g. $\Delta\varepsilon = 1.0\%$, the material trends to present slight cyclic softening; When strain-range is modest, e.g. $\Delta\varepsilon = 1.5\%$, the

material shows neutral cyclic behaviour; When strain-range is relatively high, e.g. $\Delta\varepsilon = 3.0\%$, continuous increase of cyclic hardening can be observed during the increase of loading cycles. At 300 °C, this strain-range-dependency of the austenitic material is enlarged. Namely, $\Delta\varepsilon = 1.0\%$ yields obvious cyclic softening, while $\Delta\varepsilon = 2.0\%$ gives continuous cyclic hardening.

The ferritic material 20 MnMoNi 5-5 shows significant nonlinear strain-hardening and obvious yield limit. Especially at room temperature, a clear yielding stage can be observed in the monotonic tensile test. Under uniaxial cyclic loading at room temperature, the ferritic material shows incipient cyclic hardening at the beginning. Subsequently, cyclic softening arises for all tested strain-ranges, 1.0%, 2.0% and 4.0%. The magnitudes of cyclic hardening and cyclic softening are enlarged with the increase of the strain-range. At 300 °C, the ferritic material presents just different cyclic behaviour to the austenitic material. Namely, after the incipient cyclic hardening, lower strain-range trends to yield cyclic hardening, while the higher strain-range trends to show cyclic softening.

To fit the material parameters in the viscoplastic Chaboche model, the optimization program MINUIT was used. The uniaxial form of the constitutive equations of the viscoplastic Chaboche model was programmed in MINUIT. During the parameter fitting procedure, the complete differential equation system of the material model is integrated at each discrete time point, so that the calculated values can be compared with the measurements in the uniaxial tests. The error between experiment and calculation is calculated for each time point. The new parameter set is calculated by using optimization methods provided by MINUIT, and the integration restarts by using the optimized parameters. This process is repeated until the minimum error is obtained. To ensure that the material model is able to describe the comprehensive cyclic behaviour of the selected materials, a series of uniaxial tests were applied, which include uniaxial tensile tests, uniaxial strain-controlled cyclic tests and stress-controlled multiple step cyclic tests with mean-stresses. The comparisons between the experiments and calculates show good consistencies for the austenitic material at room temperature and 300 °C. For the ferritic material, the model predictions demonstrate also good agreements to the experiments at room temperature and 300 °C. The small deflections concerning the tensile yield curves and hysteresis loops at room temperature can be ex-

plained by the initial yielding in monotonic tension and the first cycle of uniaxial cyclic tests.

For the investigation of the multiaxial ratchetting behaviour and effect of nonproportional cyclic loading in multiaxial stress-state, component tests were performed for the selected materials at room temperature and 300 °C by using straight pipe segments. For the austenitic material, multiaxial ratchetting test, in-phase-test and out-of-phase test were carried out at room temperature and 300 °C, respectively. For the ferritic material, multiaxial ratchetting test, in-phase-test and out-of-phase test were performed at room temperature.

To investigate and verity the viscoplastic Chaboche model, a series of FE analyses were performed by using commercial FEM software ABAQUS. The material model was defined in ABAQUS user's subroutine UMAT, and FE model of pipe component was set up by using pre-processing software PATRAN.

The functionality of the viscoplastic Chaboche model was qualitatively investigated by performing a series of FE calculations with different kinematic hardening and isotropic hardening approaches. For various cyclic hardening/softening behaviour of the selected material, different isotropic hardening approaches were applied and further developed in this work, so that cyclic continuous hardening, cyclic saturated hardening and combined cyclic hardening and softening can be simulated. For strain-hardening and multiaxial ratchetting behaviour, Armstrong-Frederick approach, Ohno-Wang approaches II were employed regarding back-stresses. By comparing FEA results using different kinematic hardening approaches with experimental results, it has been detected that although both kinematic hardening approaches provide satisfying results for strain-hardening, Armstrong-Frederick approach always overestimates ratchetting strain, whereas using Ohno-Wang approach II the overestimation of multiaxial ratchetting can be diminished.

To qualitatively investigate the material model for the effect of multiaxial nonproportional cyclic loading, five different load-paths were defined. By using Krämer-Krolop approach for the back-stress, the viscoplastic Chaboche model is able to simulate additional hardening evoked by the effect of nonproportional cyclic loading. The magni-

tude of the additional hardening depends on the nonproportionality of the multiaxial cyclic loads. Nevertheless the introduction of the additional parameters in Krämer-Krolop approach increases the complexity of parameter fitting, since for fitting these parameters, the procedure of parameter fitting should be extended from one-dimensional to three-dimensional.

For the quantitative verification of the material model, FE calculations were performed corresponding to the component tests. Regarding the multiaxial ratchetting tests, the FE calculations by using viscoplastic Chaboche modal with integrated Ohno-Wang approach II, combined cyclic hardening-softening approach, and evolution equations of strain-memory-effect presented good agreements to the experiments regarding strain-hardening, cyclic hardening/softening. Regarding multiaxial ratchetting, above mentioned material model presented good agreement to test results of asymptotic ratchetting. The transient ratchetting in single step multiaxial ratchetting test can be accurately predicted by the model with a refitted material parameter c_i by specifying a higher priority in parameter fitting. The cost of it was the quality of strain-hardening calculated by the material model decreased slightly. In multiple step ratchetting tests, when the primary load suddenly jumped up in the transit of two steps, the material model presented an overestimation in transient ratchetting strain. This result can be explained by different features between uniaxial ratchetting and multiaxial ratchetting. That is, the same change of primary stress (mean-stress for uniaxial ratchetting) leads to different change of ratchetting strain in uniaxial stress-state and multiaxial stress-state. This specially feature of multiaxial ratchetting is very complex and is not investigated in this work.

Regarding the in-phase- and out-of-phase tests, corresponding FE calculations were performed using the viscoplastic Chaboche model with Krämer-Krolop approach for isotropic hardening, and combined cyclic hardening/softening approach for isotropic hardening, and the evolution equations of strain-memory-effect for the austenitic material at room temperature and 300°C. Two trial parameter values were applied for Krämer-Krolop approach in the FE calculations. Via the evaluation of cyclic hardening behaviour, it can be found that the material model is able to simulate additional cyclic hardening under nonproportional cyclic loading, which accords with the experimental results qualitatively. For the quantitative predict of the effect of nonproportional load-

ing, the parameters in Krämer-Krolop approach should be fitted using corresponding experiment data.

Based on above summaries and discussions, conclusions can be drawn as following: By using the viscoplastic Chaboche model with adequate kinematic and isotropic hardening approaches, various material behaviour under multiaxial cyclic loading can be simulated by means of FE analysis. For simulating multiaxial ratchetting, Ohno-Wang approach II should be applied, which presented good agreements to the experiments in single step multiaxial ratchetting test. Regarding the simulation of the effect of multiaxial nonproportional cyclic loading, Krämer-Krolop approach should be applied. The strain-range-dependent cyclic hardening/softening behaviour of the austenitic and ferritic materials can be simulated by using different isotropic hardening approaches introduced and developed in this work.

The following work can be done for the further investigation and improvement of current material model: The relationship between the changes in uniaxial ratchetting and multiaxial ratchetting evoked by the change of primary stress in multiple step ratchetting tests should be investigated, so that multiaxial ratchetting in multiple step tests can be better predicted. Additionally, for the quantitative description of the effect of multiaxial nonproportional cyclic loading, the parameters in Krämer-Krolop approach should be fitted through appropriate experiments.

9 Literatures:

[1] Sicherheitstechnische Regeln des Kerntechnischen Ausschusses (KTA), Komponenten des Primärkreises von Leichtwasserreaktoren, KTA 3201, C. Heymann Verlag, Köln.

[2] Bundesminister des Innern, Sicherheitskriterien für Kernkraftwerke vom 21. Oktober 1977, Gesellschaft für Reaktorsicherheit mbH, Köln, 1977.

[3] RSK-Leitlinien für Druckwasserreaktoren, 3. Ausgabe, mit Anhang „spezifikationnen Basissicherheit", Gesellschaft für Reaktorsicherheit mbH, Köln, 1977.

[4] Mròz Z., On the description of anisotropic work-hardening, J. Mech. Phys. Solids 15, 163-175, 1967.

[5] Krieg R. D. A practical two surface plasticity theory, J. Appl. Mech. 42, 641-646 1975.

[6] Krempl E., Yao D., The viscoplastic theory based on overstress applied to ratchetting and cyclic hardening. In: K.-T. Rie, Hrsg., Low cycle fatigue and elastoplastic behaviour of materials, Elsevier Applied Science, London, 137-148, 1987.

[7] McDowell D. L., A two suface model for transient nonproportional cyclic plasticity – Part 1 and 2, J. Appl. Mech., Trans. ASME 52, 298-308, 1985.

[8] Miller A., An inelastic constitutive model for monotonic, cyclic and creep deformation, J. Eng. Mat. Techn. 97-105, 1976.

[9] Hornberger K., Anwendung viskoplastischer Stoffgesetze in Finite Element Programmen, Dissertation, Universität Karlsruhe, 1988.

[10] Chaboche J. L., Time-independent constitutive theories for cyclic plasticity. Int. J. of Plasticity, 2(2), 149-188, 1986.

[11] Chaboche J. L., Cailletaud G., On the calculation of structures in cyclic plasticity and viscoplasticity, ONERA-Report, no. 1986-1, 23-31, 1986.

[12] Chaboche J. L., Constitutive equations for cyclic plasticity and cyclic viscoplasticity, Int. J. Plast. 5, 247-302, 1989.

[13] Lemaitre J., Chaboche J. L., Mechanics of solid materials, Cambridge University Press, 1990.

[14] Mendelson A., Plasticity, Theory and application, Macmillen Company, New York, 1968.

[15] Kröner E., in Sommerfeld A., Vorlesungen über theoretische Physik, Band 2, Mechanik der deformierbaren Medien, Akademische Verlagsgesellschaft, Leipzig, 1970.

[16] Hill R., The Mathematical Theory of Plasticity, Oxford University Press, 1950.

[17] Martin J. B., Plasticity: Fundamentals and General Results, MIT Press, Cambridge, Mass., 1975.

[18] Stouffer D. C, Dame L. T., Inelastic Deformation of Metals, John Wiley & Sons, Inc. 1996.

[19] Odqvist F. K. G. Mathematical theory of creep and creep rupture. The ClarendonPress, Oxford, 1974

[20] Burgreen D., Design Methods for Power Plant Structures, C.P. Press, 80-60 190th St., Jamaica, N.Y. 11423, 1975.

[21] Chaboche J. L., Nouaihas D., Constitutive modelling if ratchetting effects, Trans. ASME 111, 384-416, 1989.

[22] Bingham E. C., Fluidity and plasticity, McGraw hill, New York, 1922.

[23] Cristescu N., Suliciu I., Viscoplasticity, Martinus Nijhoff Publishers, The Hague/Boston/London.

[24] Prager W., The theory of plasticity: a survey of recent achievements, Proc. Inst. Mech. Eng., 169, 41. 1955.

[25] Besseling J. F., A Theory of Elastic, Plastic and Creep Deformations of an Initially Isotropic Material showing Anisotropic Strain-Hardening, Creep Recovery and Secondary Creep, J. Appl. Mech., 80, 529, 1958.

[26] Meuers P., Description of Multiaxial Creep behaviour using the Overlay Model. A short presentation, IUTAM Symp. on Creep in Structures, Leicester, Springer-Verlag, 1980.

[27] Dafalias Y. F., Popov E. P., Plastic Internal Variables Formalism of Cyclic Plasticity, J. Appl. Mech., 98, 645, 1976.

[28] Robinson D. N., Pugh C. E., and Corum J. M., Constitutive Equations for Describing High Temperature Inelastic Behaviour of Structural Alloys, ORNL Report 766027, 1976.

[29] Kawai M., Ohashi Y., Coupled Effect between Creep and Plasticity of Type 316 Stainless Steel at Elevated Temperature, 2nd Int. Conf. On Constitutive Laws for Engineering Materials: Theory and Applications, Tucson, Arizona, Desai et al. (eds.), Elsevier, 1987.

[30] Chaboche J. L., Rousselier G., On the Plastic and Viscoplastic Constitutive Equations, Parts I and II, J. Pressure Vessel Technol., 105, 153, 1983.

[31] Krempl E., On the Interaction of Rate and History Dependence in Structural Metals, Acta Mech., 22, 53, 1975.

[32] Ghonheim H., Matsouka S., Chen Y., Viscoplastic Modelling with Strain Rate History Dependency, J. Apply. Mech. 20, 465-468, 1983.

[33] Tanaka E., Murakami S. and M Ooka, Effects of strain path shapes on nonproportional cyclic plasticity, J. Mech. Phys. Solids, 33, 559-575, 1985.

[34] Chaboche J. L., A new constitutive framework to describe ratchetting effects, 2nd Int. Symp. on plasticity and its current application, Plasticity '89, MIE University, Japan. 1989.

[35] Chaboche J. L., Nouailhas D., Paulmier P, Policella, H., Problems of describing ratchetting effects in cyclic plasticity and viscoplasticity, ONERA-Report. no. 1989-1, 63-79, 1989.

[36] Chaboche J. L., Nouaihas D., A unified constitutive model for cyclic viscoplasticity and its application to various stainless steels, Trans. ASME 111, 424-430, 1989.

[37] Chaboche J. L., Nouailhas D., Pacou D., Paulmier P., Modelling of the cyclic response and ratchetting effects on Inconel-718 Alloy, Eur. J. Mech., A/Solids 10 [1], 101-121, 1991.

[38] Chaboche J. L., Nouailhas D. An Analysis of a New Class of Integration Algorithms for Elastoplastic Constitutive Equations, Int. J. Num. Meth. Eng. 23, 353, 1986.

[39] Rice J. R., On the structure of stress-strain relations for time dependent plastic deformation in metals, ASME Journal of Applied Mechanics, Vol.37, 728-733, 1970.

[40] Malinin, N. N., Knadjinsky, G. M. Theory of creep with anisotropic hardening, J. Mech. Sci., 14, 235. 1972

[41] Ziegler H., A modification of Prager's hardening rule, Quart. Appl. Math., 17, 55-60, 1959.

[42] Walker K. P., Research and development program for non-linear structural modelling with advanced time-temperature dependent constitutive relationships, Report PWA-5700-50, NASA, 1980.

[43] Ohno N., A constitutive model of cyclic plasticity with a non-hardening strain region, J. Appli. Mech., 49, 721-727, 1982.

[44] Krempl E., McMahon J. J. and Yao D., Viscoplasticity based on overstress with a differential law for the equilibrium stress, Mech. Materials, 5, 35-48, 1986.

[45] Watanabe O. and Atluri S. N., Constitutive modelling of cyclic plasticity and creep, using an internal time concept, Int. J. Plasticity, 2(2), 107-134, 1986.

[46] Armstrong P. J., Frederick C. O., A mathematical representation of the multiaxial Bauschinger effect, G. E. G. B. report RD/B/N 731, 1966.

[47] Chaboche J. L., Viscoplastic constitutive equations for the description of cyclic and anisotropic behaviour of metals, 17th Polish Conf. On Mechanics of Solids, Szczyrk. Bul. De l'Acad. Polonaise des Sciences, Série Sc. Et Techn., 25, p.33, 1977.

[48] Harrison G. F., and Evans, W. J., A creep deformation map for nimonic 90—Its construction, interpretation and implications for life prediction, International Conference on Engineering Aspects of Creep, Sheffiels, 1980.

[49] Chaboche J. L., Dang-Van k., and Cordier G., Modelization of the strain-memory-effect on the cyclic hardening of 316 stainless steel, SMIRT-5, Division L. Berlin, 1979.

[50] Chaboche J. L., Cyclic plasticity modelling and ratchetting effects, 2nd Int. Comf. On Constitutive Laws for Engineering Materials: Theory and applications, Tucson, Arizoma, Desai et al. (eds.), Elsevier, 1987.

[51] Krolop S., et. al., Die numerische Simulation inelastischen Werkstoffverhalten und deren Bewertung anhand von Bauteilversuchen im Temperaturbereich unter $400^{o}C$, Forschungsvorhaben 1500955, Zwischenbericht, MPA Stuttgart, 1995.

[52] Krolop S., et. al., Die numerische Simulation inelastischen Werkstoffverhalten und deren Bewertung anhand von Bauteilversuchen im Temperaturbereich unter $400^{o}C$, Forschungsvorhaben 1500955, Abschlußbericht, MPA Stuttgart, 1997.

[53] Chaboche J. L., On some modifications of kinematic hardening to improve the description of ratchetting effects, Int. J. Plast. 7, 661-678, 1991.

[54] Scheffold A., Experimentelle und numerische Untersuchungen zum zyklischen, inelastischen verformungsverhalten austenitischer Stähle, Doktorarbeit, MPA Stuttgart, 1997.

[55] Burlet H., Cailletaud G., Modelling of cyclic plasticity in finite element codes, 2nd Int. Conf. Of Constitutive Laws for Engineering Materials: Theory and Application, 1987, 1157-1164, 1987.

[56] Hassan T., Corona E., Kyriakides S., Ratchetting in cyclic plasticity, Int. J. Plasticity, 8, 117, 1992.

[57] Dafalias Y. F., Modelling cyclic plasticity: Simplicity versus sophistication, Int. Conf. On Constitutive Laws for Engineering Materials, Tucson, Desai and Gallagher(eds.), 1983.

[58] Inoue T., Igari T, Yoshida F., Suzuki A., and Murakami, S., Inelastic behaviour of 2¼ Cr-Mo steel under plasticity-creep interaction conditions, Nucl. Eng. And Design, 90, 1985.

[59] Inoue T., Ohno N., Suzuki A., and Igari T., Evaluation of inelastic constitutive models under plasticity-creep interaction for 2¼Cr-1Mo steel at 600°C, Nucl. Eng. Design, 114, 285, 1989.

[60] Inoue T., Yoschida F., Ohno N., Kawai M., Niitus Y., and Imatani S., Evaluation of inelastic constitutive models under plasticity-creep interaction in multiaxial stress states, Nucl. Eng. Design, 126, 1, 1991.

[61] Freed A. D., Walker K. P., Model development in viscoplastic Ratchetting, NASA report, TM-102509, NASA, 1990.

[62] Ohno N., Wang J. -D., Kinematic hardening rules with critical state of dynamic recovery, part I: Formulation and basic features for ratchetting behaviour, Int. J. of Plasticity, 9, 375-390, 1993.

[63] Ohno N., Wang J. -D., Kinematic hardening rules with critical state of dynamic recovery, part II: Application to experiments of ratchetting behaviour, Int. J. of Plasticity, 9, 375-390, 1993.

[64] Dieter G. E., Mechanical metallurgy, 2nd el., McGraw-Hill, New York, 160-165,1976.

[65] Moosbrugger J. C., McDowell D. L., On a class of kinematic hardening rules for nonproportional cyclic plasticity, ASME J. Eng. Mat. Techn., 111, 87, 1989.

[66] Lamba H. S., Sidebottom O. M., Cyclic plasticity for nonproportional paths: Part 1, Cyclic hardening, erasure of memory, and subsequent strain hardening experiments; Part 2, Comparison with predictions of three incremental plasticity models, ASME J. Eng. Mat. Techn., 100, 96, 1978.

[67] Krämer D, Krolop S, Scheffold A, Stegmeyer R, Investigations on the ratchetting behaviour of austenitic pipes, 20th MPA-seminar, 1994.

[68] Krempl E., Lu H., The hardening and rate-dependent behaviour of fully annealed AISI type 304 stainless steel under biaxial in-phase and out-of-phase strain cycling at room temperature, ASME J. of Eng. Mat. & Tech, Vol. 106, 376-382, 1984.

[69] Moosbrugger J. C., McDowell D. L., A rate-depedent bounding surface model with a generalized image point for cyclic nonproportional viscoplasticity, J. Mech. Phys. Solids, 38, 627, 1990.

[70] Marquis D., Etude thèorique et vèrification expèrimentale d'un modèle de plasticitè, Thèse Paris VI, 1979.

[71] Rousselier G. Etude Comparative de Modèles de Comportement pour la Simulation d'Essais en Traction-Pression sur Tubes en Acier Inoxydable, Document EDF, Annexe du rapport no. 8, 1985.

[72] Hibitt, Karlsson & Sorensen, Inc., ABAQUS, User's Manual, Version 6.3, 2003.

[73] Ortiz M., Simon J. C., An analysis of a new class of integration algorithms for elastoplastic constitutive equations, Int. J. Num. Meth. Eng. 23, 353, 1986.

[74] Chan K. S., Bodner S. R., Lindholm U. S., Phenomenological Modelling of Hardening and Thermal Recovery in Metals, J. Eng. Mat. Techn. 110, 1-8, 1988.

[75] Dixon L. C. W., Non-linear optimization, English Universities Press, London, 1972.

[76] Gill P. E., Murray W., While M. H., Pratical optimization, Academic Press, 1981.

[77] Müller D., Hartmann G., Identification of Materials Parameters for Inelastic Constitutive Models Using Principles of Biologic Evolution, J. Eng. Mat. Tech, 111, 299-305, 1989.

[78] Yoshimura S., Hishida H., Yagawa G., Parameter Optimization of Viscoplastic Constitutive Equations Using Hierarchical Neural Network, The Experimental Mechanics Conference, Las Vegas, USA, 1992.

[79] Maibaum G., Wahrscheinlichkeitstheorie und mathematische Statistic, VEB Deutscher Verlag der Wissenschaften, Berlin, 1980.

[80] Schwertel J., Modellierung des einachsigen mechanischen Verhaltens von Werksoffen durch viskoplastische Stoffmodelle, Dissertation, Universität Karlsruhe, 1992.

[81] Eadie W. T., Drijard D., James F. R., Roos M., Sadoulet B., Statistical Methods in Experimental Physics, North-Holland Public. Co., Amsterdam, 1971.

[82] James F., Roos M., Function Minimization and Error Analysis, CERN computer centre, program library, D506, 1992.

[83] MINUIT function minimization and error analysis reference manual, GERN Program Library Long Writeup D506, 1992.

[84] Nelder J. A., Mead R., A Simplex Method for Function Minimization. Comput. J. 7, 308, 1965.

[85] Dennis J. E., jr., Schnabel R. B., Numerical Methods for Unconstrained Optimization and Nonlinear Equations, Prentice-Hall, Inc., Englewood Cliffs, New Jersey 07632, 1983.

[86] Fletcher R, A New Approach to Variable Metric Algorithms, Comput. J. 13, 317, 1970.

[87] Hibitt, Karlsson & Sorensen, Inc., ABAQUS, Theory Maunal, Version 6.3, 2003.

[88] MSC. Patran 2005 User's Guides & Reference Manuals.

[89] Nukleare Sicherheits- und Entsorgungsforschung - Vorhaben-Nr. 1501392; Sicherheitsbewertung kerntechnischer Komponenten bei komplexer, mehrachsiger Schwingbeanspruchung." MPA Universität Stuttgart

Appendix

A1. Formulation of the viscoplastic Chaboche model incorporating Armstrong-Frederick approach for kinematic hardening variable and continuous cyclic hardening approach for isotropic hardening variable.

Stress calculation:

$$\dot{\underline{\underline{\sigma}}} = \underline{\underline{E}}\dot{\underline{\underline{\varepsilon}}}_{el} = \underline{\underline{E}}(\dot{\underline{\underline{\varepsilon}}} - \dot{\underline{\underline{\varepsilon}}}_{p})$$

Yield condition:

$$f = J_2(\underline{\underline{\sigma}} - \underline{\underline{X}}) - R - k > 0, \quad J_2(\underline{\underline{\sigma}} - \underline{\underline{X}}) = \sqrt{\frac{3}{2}(\underline{\underline{\sigma}}' - \underline{\underline{X}}') : (\underline{\underline{\sigma}}' - \underline{\underline{X}}')}$$

Flow rule:

$$\dot{\underline{\underline{\varepsilon}}}_{p} = \frac{3}{2}\dot{p}\frac{\underline{\underline{\sigma}}' - \underline{\underline{X}}'}{J_2(\underline{\underline{\sigma}} - \underline{\underline{X}})}$$

$$\dot{p} = \left\langle \frac{J_2(\underline{\underline{\sigma}} - \underline{\underline{X}}) - R - k}{Z} \right\rangle^{n}$$

$$H(F) := \begin{cases} 1 & if \quad F \geq 0 \\ 0 & if \quad F < 0 \end{cases}; \quad \langle F \rangle := F \cdot H\langle F \rangle$$

Viscous stress (over stress):

$$J_2(\underline{\underline{\sigma}} - \underline{\underline{X}}) - R - k - \sigma_{vis} = 0$$

$$\sigma_{vis} = Z \cdot \dot{p}^{1/n}$$

Kinematic hardening:

$$\dot{\underline{\underline{X}}}_1 = \frac{2}{3}c_1\dot{\underline{\underline{\varepsilon}}}_{p} - \gamma_1\underline{\underline{X}}_1\dot{p}$$

$$\dot{\underline{\underline{X}}}_2 = \frac{2}{3}c_2\dot{\underline{\underline{\varepsilon}}}_{p} - \gamma_2\underline{\underline{X}}_2\dot{p}$$

$$\dot{\underline{\underline{X}}}_3 = \frac{2}{3}c_3\dot{\underline{\underline{\varepsilon}}}_p - \beta_3\underline{\underline{X}}_3\dot{p}; \quad \beta = \begin{cases} \gamma_{31} & \text{for} \quad J_2(\underline{\underline{X}}_3) \leq X_L \\ \gamma_{32}\left(1 - \dfrac{X_L}{J_2(\underline{\underline{X}}_3)}\right) & \text{for} \quad J_2(\underline{\underline{X}}_3) > X_L \end{cases}; \quad \gamma_{31} << \gamma_{32}$$

$$\dot{\underline{\underline{X}}}_4 = \frac{2}{3}c_4\dot{\underline{\underline{\varepsilon}}}_p - \gamma_4\underline{\underline{X}}_4\dot{p}$$

$$\underline{\underline{X}} = \underline{\underline{X}}_1 + \underline{\underline{X}}_2 + \underline{\underline{X}}_3 + \underline{\underline{X}}_4$$

Isotropic hardening:

$$\dot{R} = [b(Q - R)H(q_s - q_1) + aH(q_s - q_2)p]\dot{p}$$

strain memory:

$$F = \frac{2}{3}J_2\left(\underline{\underline{\varepsilon}}_p - \underline{\underline{\xi}}\right) - q_s \leq 0; \quad J_2\left(\underline{\underline{\varepsilon}}_p - \underline{\underline{\xi}}\right) = \sqrt{\frac{3}{2}\left(\underline{\underline{\varepsilon}}_p{}' - \underline{\underline{\xi}}'\right):\left(\underline{\underline{\varepsilon}}_p{}' - \underline{\underline{\xi}}'\right)}$$

$$\dot{q}_s = \eta H(F)\left\langle \underline{\underline{n}}:\underline{\underline{n}}^* \right\rangle\dot{p}$$

$$\dot{\underline{\underline{\xi}}} = (1 - \eta)\sqrt{\frac{3}{2}}H(F)\left\langle \underline{\underline{n}}:\underline{\underline{n}}^* \right\rangle\underline{\underline{n}}^*\dot{p}$$

$$\underline{\underline{n}} = \sqrt{\frac{2}{3}}\frac{\dot{\underline{\underline{\varepsilon}}}_p}{\dot{q}_s} = \sqrt{\frac{3}{2}}\frac{\underline{\underline{\sigma}}' - \underline{\underline{X}}'}{J_2\left(\underline{\underline{\sigma}} - \underline{\underline{X}}\right)}$$

$$\underline{\underline{n}}^* = \sqrt{\frac{2}{3}}\frac{\underline{\underline{\varepsilon}}_p - \underline{\underline{\xi}}}{q_s}$$

$$\dot{Q} = 2\mu(Q_{max} - Q)\dot{q}_s \Rightarrow Q = Q_{max} + (Q_0 - Q_{max})e^{-2\mu q_s}; \quad Q_0 = Q(t = 0)$$

A2. Formulation of the viscoplastic Chaboche model incorporating Ohno-Wang approach II for kinematic hardening variable and mixed cyclic hardening/softening approach for isotropic hardening variable.

Stress calculation:

$$\dot{\underline{\underline{\sigma}}} = \underline{\underline{E}}\dot{\underline{\underline{\varepsilon}}}_{el} = \underline{\underline{E}}(\dot{\underline{\underline{\varepsilon}}} - \dot{\underline{\underline{\varepsilon}}}_p)$$

Yield condition:

$$f = J_2(\underline{\underline{\sigma}} - \underline{\underline{X}}) - R - k > 0, \quad J_2(\underline{\underline{\sigma}} - \underline{\underline{X}}) = \sqrt{\frac{3}{2}(\underline{\underline{\sigma}}' - \underline{\underline{X}}') : (\underline{\underline{\sigma}}' - \underline{\underline{X}}')}$$

Flow rule:

$$\dot{\underline{\underline{\varepsilon}}}_p = \frac{3}{2}\dot{p}\frac{\underline{\underline{\sigma}}' - \underline{\underline{X}}'}{J_2(\underline{\underline{\sigma}} - \underline{\underline{X}})}$$

$$\dot{p} = \left\langle \frac{J_2(\underline{\underline{\sigma}} - \underline{\underline{X}}) - R - k}{Z} \right\rangle^n$$

$$H(F) := \begin{cases} 1 & if \quad F \geq 0 \\ 0 & if \quad F < 0 \end{cases}; \quad \langle F \rangle := F \cdot H\langle F \rangle$$

Viscous stress (over stress):

$$J_2(\underline{\underline{\sigma}} - \underline{\underline{X}}) - R - k - \sigma_{vis} = 0$$

$$\sigma_{vis} = Z \cdot \dot{p}^{1/n}$$

Kinematic hardening:

$$\dot{\underline{\underline{X}}}_1 = \frac{2}{3}c_1\dot{\underline{\underline{\varepsilon}}}_p - \gamma_1\left(\frac{J_2(\underline{\underline{X}}_1)}{h_1}\right)^{m_i}\sqrt{\frac{3}{2}}\langle \underline{\underline{n}} : \underline{\underline{k}}_1 \rangle\underline{\underline{X}}_1\dot{p}, \quad i=1, 2, 3, 4$$

$$h_i = \frac{c_i}{\gamma_i}, \quad \underline{\underline{k}}_i = \frac{\underline{\underline{X}}_i}{J_2(\underline{\underline{X}}_i)}$$

$$\underline{\underline{X}} = \underline{\underline{X}}_1 + \underline{\underline{X}}_2 + \underline{\underline{X}}_3 + \underline{\underline{X}}_4$$

Isotropic hardening:

$$\dot{R} = [a(cQ - R)H(q_1 - p) - b((1 - c)Q + R)H(p - q_1)]\dot{p}$$

strain memory:

$$F = \frac{2}{3} J_2\left(\underline{\underline{\varepsilon}}_p - \underline{\underline{\xi}}\right) - q_s \leq 0; \quad J_2\left(\underline{\underline{\varepsilon}}_p - \underline{\underline{\xi}}\right) = \sqrt{\frac{3}{2}\left(\underline{\underline{\varepsilon}}_p{}' - \underline{\underline{\xi}}{}'\right) : \left(\underline{\underline{\varepsilon}}_p{}' - \underline{\underline{\xi}}{}'\right)}$$

$$\dot{q}_s = \eta H(F)\left\langle \underline{\underline{n}} : \underline{\underline{n}}^* \right\rangle \dot{p}$$

$$\dot{\underline{\underline{\xi}}} = (1-\eta)\sqrt{\frac{3}{2}} H(F)\left\langle \underline{\underline{n}} : \underline{\underline{n}}^* \right\rangle \underline{\underline{n}}^* \dot{p}$$

$$\underline{\underline{n}} = \sqrt{\frac{2}{3}} \frac{\dot{\underline{\underline{\varepsilon}}}_p}{\dot{q}_s} = \sqrt{\frac{3}{2}} \frac{\underline{\underline{\sigma}}{}' - \underline{\underline{X}}{}'}{J_2\left(\underline{\underline{\sigma}} - \underline{\underline{X}}\right)}$$

$$\underline{\underline{n}}^* = \sqrt{\frac{2}{3}} \frac{\underline{\underline{\varepsilon}}_p - \underline{\underline{\xi}}}{q_s}$$

$$\dot{Q} = 2\mu(Q_{max} - Q)\dot{q}_s \quad \Rightarrow Q = Q_{max} + (Q_0 - Q_{max})e^{-2\mu q_s}; \quad Q_0 = Q(t=0)$$

A3. Formulation of the viscoplastic Chaboche model incorporating Krämer-Krolop approach for kinematic hardening variable and mixed cyclic hardening/softening approach for isotropic hardening variable.

Stress calculation:

$$\dot{\underline{\underline{\sigma}}} = \underline{\underline{E}}\dot{\underline{\underline{\varepsilon}}}_{el} = \underline{\underline{E}}(\dot{\underline{\underline{\varepsilon}}} - \dot{\underline{\underline{\varepsilon}}}_p)$$

Yield condition:

$$f = J_2(\underline{\underline{\sigma}} - \underline{\underline{X}}) - R - k > 0, \quad J_2(\underline{\underline{\sigma}} - \underline{\underline{X}}) = \sqrt{\frac{3}{2}(\underline{\underline{\sigma}}' - \underline{\underline{X}}') : (\underline{\underline{\sigma}}' - \underline{\underline{X}}')}$$

Flow rule:

$$\dot{\underline{\underline{\varepsilon}}}_p = \frac{3}{2}\dot{p}\frac{\underline{\underline{\sigma}}' - \underline{\underline{X}}'}{J_2(\underline{\underline{\sigma}} - \underline{\underline{X}})}$$

$$\dot{p} = \left\langle \frac{J_2(\underline{\underline{\sigma}} - \underline{\underline{X}}) - R - k}{Z} \right\rangle^n$$

$$H(F) := \begin{cases} 1 & if \quad F \geq 0 \\ 0 & if \quad F < 0 \end{cases}; \quad \langle F \rangle := F \cdot H\langle F \rangle$$

Viscous stress (over stress):

$$J_2(\underline{\underline{\sigma}} - \underline{\underline{X}}) - R - k - \sigma_{vis} = 0$$

$$\sigma_{vis} = Z \cdot \dot{p}^{1/n}$$

Kinematic hardening:

$$\dot{\underline{\underline{X}}}_i = \frac{2}{3}c_i\dot{\underline{\underline{\varepsilon}}}_p - \gamma_i(1 - \gamma'_i(1 - e^{-p_i^*}))\underline{\underline{X}}_i\dot{p}, \quad i=1, 2, 3, 4$$

$$\dot{p}_i^* = c''_i |\sin\varphi|\dot{p}$$

$$\varphi := \arccos\left[\frac{\dot{\underline{\underline{\varepsilon}}}_p : \underline{\underline{\varepsilon}}_p}{\left\|\dot{\underline{\underline{\varepsilon}}}_p\right\|\left\|\underline{\underline{\varepsilon}}_p\right\|}\right].$$

$$\underline{\underline{X}} = \underline{\underline{X}}_1 + \underline{\underline{X}}_2 + \underline{\underline{X}}_3 + \underline{\underline{X}}_4$$

Isotropic hardening:

$$\dot{R} = [a(cQ - R)H(q_1 - p) - b((1-c)Q + R)H(p - q_1)]\dot{p}$$

strain memory:

$$F = \frac{2}{3}J_2\left(\underline{\underline{\varepsilon}}_p - \underline{\underline{\xi}}\right) - q_s \leq 0; \quad J_2\left(\underline{\underline{\varepsilon}}_p - \underline{\underline{\xi}}\right) = \sqrt{\frac{3}{2}\left(\underline{\underline{\varepsilon}}_p' - \underline{\underline{\xi}}'\right) : \left(\underline{\underline{\varepsilon}}_p' - \underline{\underline{\xi}}'\right)}$$

$$\dot{q}_s = \eta H(F)\left\langle \underline{\underline{n}} : \underline{\underline{n}}^* \right\rangle \dot{p}$$

$$\dot{\underline{\underline{\xi}}} = (1-\eta)\sqrt{\frac{3}{2}}H(F)\left\langle \underline{\underline{n}} : \underline{\underline{n}}^* \right\rangle \underline{\underline{n}}^* \dot{p}$$

$$\underline{\underline{n}} = \sqrt{\frac{2}{3}}\frac{\dot{\underline{\underline{\varepsilon}}}_p}{\dot{q}_s} = \sqrt{\frac{3}{2}}\frac{\underline{\underline{\sigma}}' - \underline{\underline{X}}'}{J_2\left(\underline{\underline{\sigma}} - \underline{\underline{X}}\right)}$$

$$\underline{\underline{n}}^* = \sqrt{\frac{2}{3}}\frac{\underline{\underline{\varepsilon}}_p - \underline{\underline{\xi}}}{q_s}$$

$$\dot{Q} = 2\mu(Q_{max} - Q)\dot{q}_s \quad \Rightarrow Q = Q_{max} + (Q_0 - Q_{max})e^{-2\mu q_s}; \quad Q_0 = Q(t=0)$$

Lebenslauf

Persönliche Daten

Name	Yu Wang
Geburtsdatum	01.August 1977
Geburtsort	Henan, V.R.China
Staatsangehörigkeit	chinesisch
Familienstand	verheiratet

Studium

09.1995 – 07.2000	Bachelorstudium in Thermal Power Engineering am Institute of Thermal Engineering der Tsinghua University in V.R. China
07.2000	Bachelorabschluss
10.2000 – 07.2002	Masterstudium in Computational Mechanics of Materials and Structures an der Universität Stuttgart
07.2002	Masterabschluss

Berufliche Tätigkeiten

09.2002 – 01.2007	Wissnschaftliche Mitarbeiter an der Materialprüfungs- anstalt der Universität Stuttgart
Seit 02.2007	Berechnungsingenieur bei TENNECO GmbH

Ludwigshafen, Juni 2014